# Carbon Fiber Tow Spreading

## Experimental Machine Design, Friction Behaviour, and Novel Monitoring Concepts

MSc Aerospace Engineering
Ehshan ul-Haq


Delft University of Technology

TU Delft

# Carbon Fiber Tow Spreading

## Experimental Machine Design, Friction Behaviour, and Novel Monitoring Concepts

by

Ehshan ul-Haq

to obtain the degree of Master of Science
at the Delft University of Technology,
to be defended publicly on Tuesday July 4, 2023 at 14:30.

Student number: 4588142
Thesis committee: Prof. C. Dransfeld, supervisor
dr. B. Caglar, supervisor
dr. D. Peeters,
dr. N. Yue



TU Delft

# Preface

This master's thesis investigates the design, assembly, and employment of an experimental tow spreading line for unidirectional carbon fiber composite tapes. The main focus is on studying friction behavior during spreading and introducing novel monitoring techniques. The findings challenge existing theories, highlighting the need for further research and process improvement. This work aims to contribute to the field of aerospace engineering and inspire future advancements in composite manufacturing.

I would like to especially thank Onur Yuksel, Baris Caglar, and Clemens Dransfeld for their help and supervision during the thesis. Additionally, I would like to thank all other staff members which provided feedback or assisted me on my work. I am very grateful to all of you.

*Ehshan ul-Haq*
*Heerlen, The Netherlands, June 2023*

# Summary

This master's thesis focuses on the design and assembly of an innovative tow spreading line for investigating carbon fiber tow spreading through the utilization of spreader bars. The primary objective was to examine the friction behavior during the spreading process by employing multiple tension sensors. Additionally, novel monitoring concepts including 4-point resistivity sensing, optical width and gap detection, and optical analysis for determining fiber orientation within the carbon tow were introduced. Through a series of experiments conducted on the newly built setup, comprehensive data was collected and analyzed.

The findings revealed an intriguing observation that deviates from the established Capstan equation. It was observed that an increase in tension in the tow resulted in a reduced apparent friction coefficient during bar tow spreading. This departure from the conventional understanding of friction dynamics in this scenario contributes valuable insights to the field of carbon fiber tow spreading.

Furthermore, the feasibility of utilizing resistivity measurements as a means of detecting material anomalies, such as damage or waviness, was investigated. The results demonstrated that this technique, while partially reliant on tow tension, consistently detected such anomalies. However, challenges were encountered in achieving quantitative consistency in the optical orientation analysis, making it difficult to obtain robust results in this aspect.

The experimental monitoring setup also revealed an increase of approximately 20% in the width of the tow. To enhance process repeatability, recommendations are proposed to upgrade several components of the built experimental line. Moreover, it is advised to further test and develop the software analysis techniques to achieve a higher degree of repeatability, thus potentially validating the obtained results.

In conclusion, this research contributes to the understanding of carbon fiber tow spreading through the design and assembly of an experimental production line, examination of friction behavior, and the introduction of novel monitoring techniques. The outcomes serve as a foundation for future investigations and advancements in this domain, with the potential to enhance the efficiency and quality of carbon fiber tow spreading processes.

# Contents

# 1 Introduction

## 1.1. Background and Motivation

Carbon fiber is a versatile material that has gained popularity in various industries due to its high strength-to-weight ratio and other desirable properties. Carbon fibers are manufactured by subjecting precursor materials to high temperatures and converting them to carbonized fibers. The carbonized fibers are then processed to improve their mechanical properties and used to make composite materials for various applications, such as aerospace, automotive, and sports equipment [1].

A critical step in carbon fiber manufacturing is the spreading process, in which carbon fiber tows are spread into flat tapes or sheets. The spreading process affects the properties of the final product and can impact the performance of composite materials made from the carbon fibers [1]. Spread tow composites undergo size effects, which can enable the material to have increased strength [2]. Understanding the behavior of carbon fiber tows during spreading is, therefore, crucial to optimize carbon fiber manufacturing processes and improve the quality of carbon fiber products.

### 1.1.1. Applications of CFRP and Thin-Ply Composites

One of the key advantages of carbon fiber composites is their high strength-to-weight ratio, making them ideal for applications where weight reduction is critical. Carbon fiber composites also offer excellent stiffness, durability, and resistance to fatigue, which make them suitable for high-performance applications [2].

Part of the recent advances in carbon fiber composites technology is tow spreading, which involves the spreading of carbon fiber filaments into a wider, flatter, and more uniform configuration. This process increases the fiber volume fraction, which results in higher strength and stiffness properties for the composite. Tow spreading also improves the interlaminar shear strength and fracture toughness of the composite, making it more resistant to delamination and damage propagation. This technique has found applications in the aerospace and automotive industries, where weight reduction is a critical factor in improving fuel efficiency and performance [3].

Thin-ply composites are another area of development in carbon fiber composites, where thinner carbon fiber plies are used to create a composite with enhanced properties. Thin-ply composites offer improved interlaminar shear strength, reduced delamination, and enhanced damage tolerance compared to traditional thick-ply composites [4]. This makes them ideal for applications where weight reduction and high-performance are critical, such as aerospace and defense applications. Below, a list is presented with examples of how thin-ply composites are being used in aerospace.

- Aircraft structural components: Thin-ply composites can be used in the manufacturing of aircraft structural components, such as wings, fuselages, empennages, and (cryogenic) fuel tanks [5]. Their high strength-to-weight ratio and improved interlaminar shear strength can help reduce the overall weight of the aircraft, leading to improved fuel efficiency and range. New solutions such

as morphing wings can possibly also be introduced [6].

- Satellite components: Thin-ply composites can be used in the manufacturing of satellite components, such as solar panels and antennas. The improved damage tolerance of thin-ply composites makes them more resistant to the harsh environments of space, leading to increased reliability and lifespan of satellite components [7].

- Helicopter rotor blades: Thin-ply composites can be used in the manufacturing of helicopter rotor blades [8]. The improved interlaminar shear strength and damage tolerance of thin-ply composites can help reduce the risk of delamination and damage propagation in the rotor blades, leading to increased safety and reliability.

- Spacecraft heat shields: Thin-ply composites can be used in the manufacturing of spacecraft heat shields. The high strength-to-weight ratio of thin-ply composites can help reduce the weight of the heat shields, leading to reduced launch costs. The improved damage tolerance of thin-ply composites can also help protect the spacecraft during re-entry into the Earth's atmosphere [9].

- Unmanned aerial vehicles (UAVs): Thin-ply composites can be used in the manufacturing of UAVs, where their high strength-to-weight ratio and improved damage tolerance can improve the endurance and reliability of the vehicles. Thin-ply composites can also help reduce the noise signature of UAVs, making them more suitable for surveillance and reconnaissance missions.

Overall, the applications of thin-ply composites in the aerospace industry are diverse, and their properties make them well-suited for high-performance and weight-critical applications. On top of the presented examples, thin-ply composites can also be used in sports and recreational equipment, such as bicycles, where their high strength-to-weight ratio can improve performance.

In conclusion, carbon fiber composites are a versatile material that has found numerous applications across a wide range of industries. The recent developments in tow spreading and thin-ply composites have further enhanced the properties of carbon fiber composites, making them even more suitable for high-performance and weight-critical applications.

### 1.1.2. Manufacturing of Carbon Rovings and CFRP

The manufacturing process of carbon fiber is complex and involves several steps. This chapter provides an overview of the manufacturing process of carbon fiber rovings, which are bundles of carbon fibers used as a reinforcement material.

There are two main materials used in the production of carbon fiber: PAN (polyacrylonitrile) and pitch [10]. PAN is derived from oil or coal and forms a thermoplastic polymer, which will later transform into carbon fiber. Pitch, on the other hand, is the residue of the distillation process of carbon-based materials such as crude oil or coal. Pitch-based fibers generally have a crystal structure in the form of sheets, making them stiffer, while PAN-based fibers have a more granular structure, making them tougher. Pitch fibers also generally have better electrical and thermal conductivity, but are more expensive than PAN fibers due to the need for an oil refinery.

Regardless of the precursor material used, the process of manufacturing carbon fiber involves several steps [11]. The precursor material is first obtained via spinning, which can be done using melt spinning, dry spinning, wet spinning, or dry jet wet spinning. Once the precursor is made, the oxidation step follows, where temperature and pressure are finely controlled to stabilize the precursor. The fibers cannot yet be called carbon fibers at this stage, as a significant portion of their content consists of non-carbon atoms. To turn them into near 100% carbon fibers, the fibers are heated in an inert atmosphere, causing the carbon atoms to orient themselves towards a structure with minimized energy. During this process, the crystal structures align more with the length direction of the fiber, resulting in a stiffness increase.

For high modulus fibers, an additional graphitization step is performed, where the fibers are placed in a high-temperature oven filled with inert gas. During this step, the crystals in the fiber align even more with the fiber direction, making for an even stiffer fiber. However, this process also results in a reduction in tensile strength. Finally, all fibers receive a surface treatment and a sizing [11].

Once the carbon fibers are produced, they are bundled together to form rovings, which are the basic unit of carbon fiber reinforcements. Various configurations of carbon fibers can be achieved through different bundling techniques. For example, single carbon fibers are too thin and fragile to be useful, so they are bundled into untwisted strands, also known as direct rovings or single end rovings. Assembled rovings, or multi-end rovings, are bundles of multiple strands that often have been twisted together to improve handling [11].

Carbon fiber composites can be made from either thermoplastic or thermoset matrices, both of which have their own advantages. Thermoplastic composites are more easily recyclable, have better toughness and can be welded [12], while thermoset composites have better chemical and heat resistance due to their cross-linked molecular structure. In both cases, the carbon fiber rovings are impregnated with the matrix material and then molded into the desired shape using heat and pressure. The final product is a composite material that combines the unique properties of carbon fiber with the advantages of the matrix material [13].

In conclusion, the production of carbon fiber rovings is a complex process that involves several steps and the use of either PAN or pitch precursor materials. The resulting carbon fibers are then bundled together to form rovings, which can be used as reinforcement materials for thermoplastic and thermoset composites. The ability to tailor the composite to specific requirements makes carbon fiber composites a popular choice in many industries, such as the aerospace industry. As research continues, it is likely that carbon fiber and its composites will play an increasingly important role in shaping the future of materials engineering.

### 1.1.3. Carbon Fiber Tow Spreading

Carbon fiber tow spreading is a critical process in the manufacturing of high-performance composite materials. It involves the precise and consistent spreading of individual carbon fibers into a wider, flatter ribbon or tape, which can then be used to create composite materials with exceptional strength-to-weight ratios. Carbon fiber tow spreading is important because it allows manufacturers to produce composite materials that are strong, lightweight, and durable. The process requires specialized machinery and expertise to ensure the fibers are properly aligned and distributed, which ultimately affects the performance of the final product. In this research, the focus is on bar tow spreading, in which the carbon tow is tensioned over a bar to engage spreading. Bar spreading machines do this by controlling the tension, wrap angle, and speed of the tows during spreading. This section reviews several relevant aspects of the bar spreading technique and related research is presented. The mentioned topics include: pre-tension, tension release, relative velocity, wrap angle, bar surface and friction, bar diameter, symmetry, and twists. Other spreading techniques are also mentioned, including air spreading, ultrasonic spreading, and electrostatic spreading. An illustration of the mechanism of tow spreading is displayed in figure 1.1.

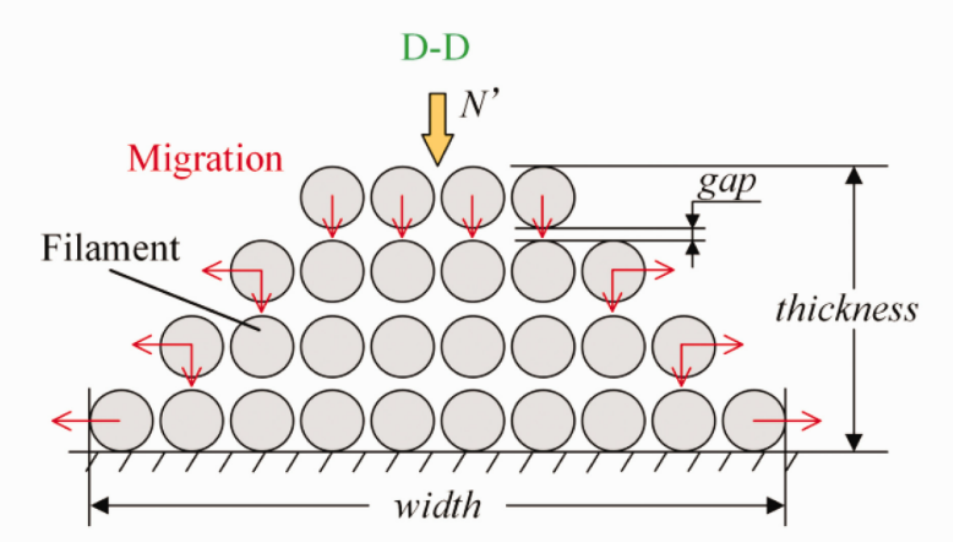


**Figure 1.1:** Diagram of the mechanism of lateral fibre spreading, showing a cross-section of a fibre bundle as it is stretched over a rod [14].

### Pre-tension

Pre-tension is the process of stretching the carbon fiber tow before spreading it. Pre-tension helps to keep the fibers aligned during spreading, which results in a more uniform and flat spread. Adjusting pre-tension can also helps to prevent damage to the fibers, which can occur if the fibers are stretched too much during spreading.

An experiment has been performed in which the effect of pretension has been analyzed on the spreading behaviour of a carbon fibre tow. The results are displayed in figure 1.2 below [15].

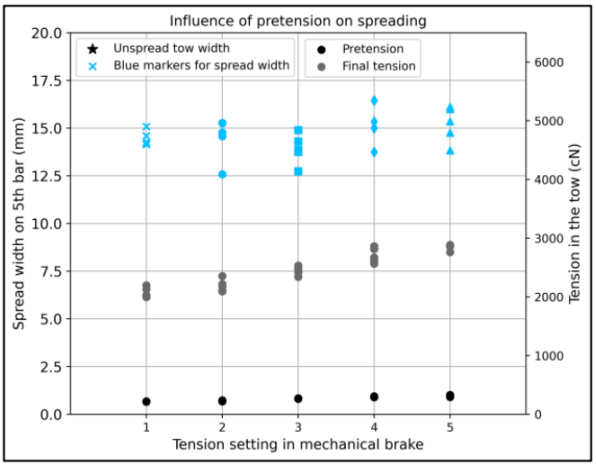


**Figure 1.2:** Influence of pretension on spreading [15].

From figure 1.2, a trend can be observed between the applied pre-tension (via a mechanical brake) and the final tension in the tow. As the pre-tension is increased, the final tension also increases. However, even though the overall tension gradient changes, there does not seem to be a noticeable trend between the pre-tension and the final spread width of the tow. This conclusion is in line with the conclusions from both [16] and [17].

Since the spreading of the tow strongly depends on the mechanical friction between the tow and the rod, and since this friction results from tension in the tow, it seems counter-intuitive that there is no correlation between pre-tension and tow spreading. Therefore, in agreement with [15], a new study will

be conducted in which the same principle is examined. In the previous study conducted by [15], the pre-tension test range was approximately 100 cN.

### Tension release

Tension release is the literal release of tension on a tow after a spreading process via bars has been performed. A study has been conducted by Irfan et al., in which he spreads a carbon fibre tow over two rods via a back and forth movement [17]. After an equilibrium of the spreading width has been achieved, an additional cycle is carried out followed by a relief in tow tension. Then, another cycle is performed. Experimental results are displayed in figure 1.3 below.

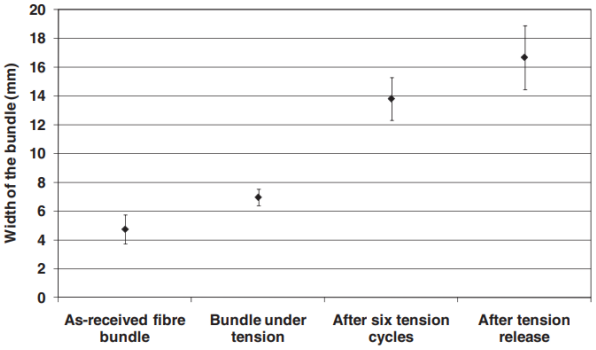


**Figure 1.3:** Width evolution of tow for various stages [18].

According to the figure above, the tension release action seems to have a notable effect on the spreading of the fibre bundle. An explanation is proposed for this phenomenon. It is believed that the spread of the bundle approaches an equilibrium value as the friction between fibres and rod, and between fibres and fibres, eventually prohibits further movement of the filaments. It is said that the fibres in the bundle keep a 'near-stable packed configuration'. Therefore, further spreading is unlikely to occur once equilibrium is reached. If, however, the tension on the tow is removed, and a new cycle is performed, the fibres are able to move relatively freely. Then, the spread width of the tow can be further increased [18].

As figure 1.3 implies, applying the additional tension release cycle can have a significant effect on the spreading of the tow. Also, it can be relatively complicated to add a tension release system to a spread-tow production line. In two known cases, carrier hubs with multiple rollers are used [3] [17]. As the tow passes over this rotating carrier hub, the total distance that the tow has to travel changes due to the rods that move with the hub. This results in a periodic relief in tension on the tow. Adding such a setup to a continuous production line would require a brake to be placed before the tension release setup. Otherwise, the release in tension is noticeable through the entire line which could potentially reduce the effect of the spreader bars.

### Relative velocity and wrap-angle

Looking at figure 1.4, it becomes clear that an increased rotational speed, in opposite direction of the moving tow, of the spreader bar causes a greater amount of spread. The mechanism of importance here is the (variable) relative velocity between bar surface and tow. The phenomenon can be explained by the fact that when the rotational speed is increased, more contact points between tow and roller occur. This means that there is a greater chance for the monofilament to be affected by a friction force, and be distanced from the center line. From the same graph it also becomes visible that an increase in wrap angle leads to an increased spread width. This has a similar potential explanation; as the wrap angle increases, the contact area between tow and roller increases as well. As the contact area increases, there is a greater distance over which the tow experiences friction (and therefore spread-inducing normal forces).

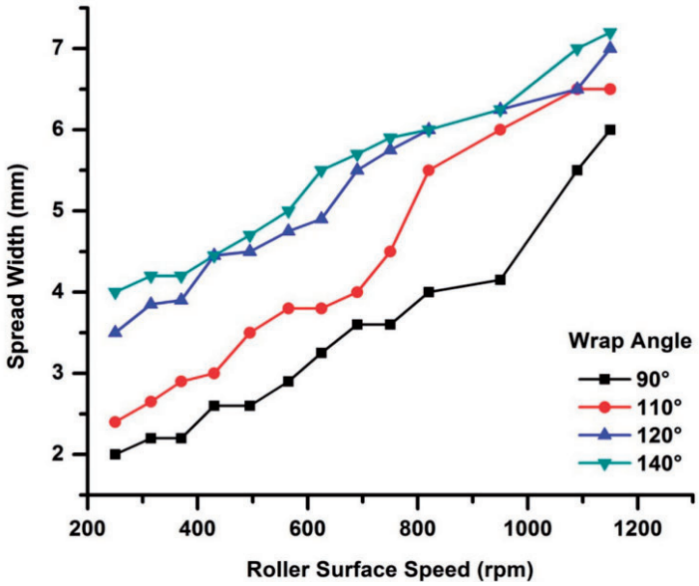


**Figure 1.4:** Spread width versus roller surface speed for various wrap angles [14].

### Bar surface roughness and Friction

Spreader bar surface roughness is also an important factor in bar tow spreading. A smooth spreader bar surface allows for easier spreading of the carbon fiber tow, but it can also cause slippage and damage to the fibers. A rough spreader bar surface can help to grip the fibers better and prevent slippage, but it can also cause damage to the fibers. Therefore, it is important to find a balance between surface roughness and grip to achieve optimal spreading results.

Depending on the material and topography of the spreader bar surface, the overall spreading properties can differ. Some materials and topographies result in processes in which the fibres experience more friction than for other parameters. Generally, friction is defined according to the Coulomb friction model shown in equation 1.1. In this equation, the force of friction $F_f$ is written to be directly proportional to the normal force $N$.

$$F_f = \mu N \tag{1.1}$$

For which $\mu$ is the coefficient of friction, and $N$ is the normal force.

Although equation 1.1 is widely used, it has been observed that the apparent coefficient of friction $\mu$ changes as the applied normal force changes instead of staying constant as the equation implies. Because of this, Howell's equation is widely accepted to estimate the correlation between friction and normal load. Howell's equation is displayed in equation 1.2 [19].

$$F_f = kN^n \tag{1.2}$$

For which $k$ is an experimentally determined coefficient of proportionality, and $n$ is a fitting parameter that relates to the deformation mechanism. The value of $n$ ranges from 2/3 for a fully elastic deformation, up to 1 for fully plastic deformation.

An experiment has been performed in which the coefficients of friction have been determined for a 12k carbon fibre tow passing over a friction drum [19]. Said tests are executed according to the Capstan measurement setup, of which a diagram is displayed in figure 1.5. The experiment included the following four different cases: (a) tow over smooth metal, (b) tow over rough metal, (c) tow over tow parallel, (d) tow over tow perpendicular.

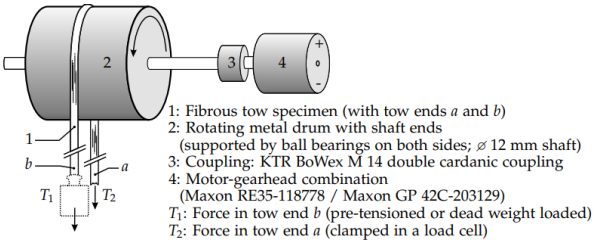


**Figure 1.5:** Schematic description of capstan experiment [19].

From the experiment, several *Major Trends* were noted. These are listed below [19].

- The friction experiments show a general trend that the friction between tow and metal is significantly higher for the smooth drum than for the rough drum.
- The friction between tow and parallel tow (on the drum) is higher or at least as high as for the friction between tow and perpendicular tow (on the drum).
- The measurements with parallel tow on the drum show that the friction coefficient is measured to be higher for tow that have a polyurethane-based sizing, compared to tows which do not have that sizing.

### Bar diameter

Changing the diameter of the rods, used to spread the tow, has been shown to have an effect on the spreading behaviour of the tow. In figure 1.6, this effect is shown for spreader bars with diameters of 30, 50, and 100 mm.

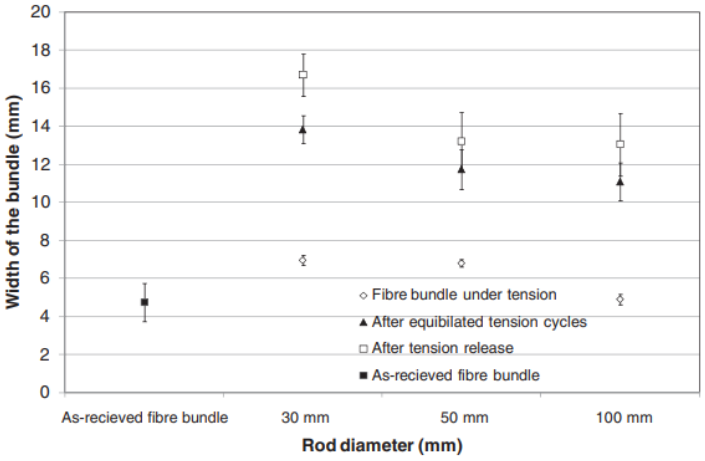


**Figure 1.6:** Rod diameter vs. tow width after spreading [18].

In this particular setup, two bars were placed next to each other. The tow was draped over the two bars and weights were attached to the ends of the tow. The findings from figure 1.6 can be explained by the following. As the tow slides over the larger diameter rods, the contact surface is larger compared to the smaller diameter rods. Since the tension in the tow remains the same, the contact stresses will be lower for the case with the larger diameter rods. Using a rod with a smaller diameter also increases the de-cohesion between the filaments, due to increased strains on the fibres as a consequence of a tighter radius. This, in turn, also contributes to the spreading of the tow. It has to be noted, however, that increased contact stresses and bending strains on the fibres can increase the damage afflicted on the fibres [18].

### Symmetry

The relative position of each of the spreader bars is what decides how the contact between the tow and the rods is. By utilizing a symmetrical spreader setup, the tension ratios (of the tow between each

rod) can be uniformly altered. A non-symmetric layout can in turn provide tension spikes. This can be beneficial in controlling the evolution of the spreading process. Non-symmetrical layouts can, for example, be used to achieve strong spreading during impregnation [15].

Lateral symmetry is essential in bar tow spreading. If the tow is not spread symmetrically, it can cause uneven fiber distributions, which can result in weak spots in the final product. Therefore, it is important to ensure that the tow is spread symmetrically during the spreading process.

### Twists

When a reel of carbon fibre is manufactured, some of the carbon fibres are twisted. The twist of a fibre can occur in two ways. Firstly, global twist. Global twist can be explained by a general twist of the tow itself. This can be resolved by hanging the tow vertically and letting the tow unwind. It is also possible to buy reels of carbon fibre for which the global twist is already mainly resolved.

The second type of twist is intra tow twist. In this case, individual fibres are *twisted* around neighboring fibres. This can be detrimental for the spreading of the tow; the intra tow twist inhibits spreading of the fibre bundle. When a section of tow passes over a spreader bar (for example), a normal force is applied on the tow which leads to lateral relative motion of the fibres. If a fibre is wrapped around a bundle of fibres, this fibre can prevent the lateral motion by carrying a tension load. Intra tow twist is difficult to simulate. However, to give an impression of the effect of twist on the spreading behaviour of a tow, a graph is shown in which maximum spread is plotted against amount of global twist in figure 1.7 [16].

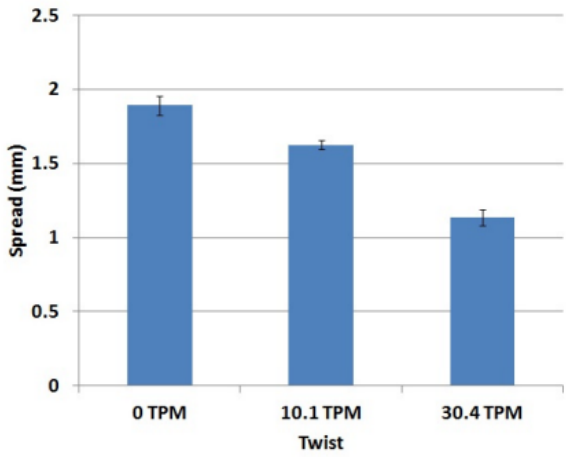


**Figure 1.7:** Maximum spreading width for untwisted, 10.1 twist/m, and 30.4 twist/m [16].

It is expected that an intra tow twist will have less of an effect on the overall spreading width than global twist. However, the effect is assumed to be significant still.

### Non-Bar tow spreading methods

There are various methods used in the carbon fiber industry to achieve flat and uniform carbon fiber tow. Some of the most common methods are air spreading, ultrasonic spreading, and electrostatic spreading.

Pneumatic spreading is a technique which uses the flow of air to spread a tow [20]. In this technique a pressure difference is applied to the tow. Applying the right amount of air pressure can result in the tow experiencing weightlessness. Then, the tow momentarily is in a state free of tension. The air, blowing through this tow, is then able to spread the fibres. It has been reported that this technique can spread 12K tow from 5mm to 25mm, reducing areal weight by 500% [20]. It is also said that air spreading generally results in less fibre damage compared to typical bar spreading methods [1]. This

is due to the contactless spreading operation, where fibre-fibre friction is the only type of solid to solid contact friction. It has also been reported that controlling the air-spreading process is difficult.

Ultrasonic spreading is a tow spreading technique which also makes use of bars to contact and guide the roving. As the tow wraps around the bar, ultrasonic vibrations are applied to the bar. The bar could also be named the sonotrode in this application. This causes a great deal of energy being transferred locally into the tow. As a result of this, the filaments experience many moments of interaction with either other fibres or the bar. The excited fibres settle down to minimize their energy. This then results in spreading of the tow [1]. The ultrasonic spreading technique cannot be used with all fibre types: the fibre has to be able to have an elastic response to the induced vibrations. If this is not the case, the fibre might break. Glass fibre and pitch-based carbon fibre are generally too brittle for ultrasonic spreading [1]. Spreading via vibrations can also be applied without the use of ultrasonic vibrations. A lower frequency, potentially mechanically induced, vibration can be applied. The induced vibrations do not have to be introduced into the tow via a bar-like interface. Rather, technologies also exist for which the vibration is transmitted through air [21].

Spreading of fibres in a tow can also be achieved via an electrostatic route [21]. For this technique, a conducting element is connected to the tow. The conducting element is connected to a high-voltage source, while one of the bars is connected to ground. Resulting from this is a voltage difference over the tow, which leads to electrostatic forces acting perpendicularly on the tow. Spreading of the tow emerges as an effect hereof [21]. A big disadvantage of this technique is that it only works for non-conducting fibres, such as glass fibres. Also, it is considered a complex and dangerous process due to the applied high voltage.

Carbon fiber tow spreading is an essential process in the production of carbon fiber composite structures. Bar tow spreading is the most common method used in the industry, and it requires careful attention to details such as pre-tension, tension release, twists, spreader bar surface roughness, spreader bar surface pattern, diameter of the spreader bar, and symmetry. Achieving a flat and uniform spread is crucial for ensuring the strength and durability of the final product.

Different tow spreading methods such as air spreading, ultrasonic spreading, and electrostatic spreading offer alternative approaches to achieving a flat and uniform spread. Each method has its own advantages and disadvantages and requires specialized equipment and expertise. As carbon fiber technology continues to advance, it is likely that new and innovative methods for achieving a flat and uniform spread will emerge. However, regardless of the method used, attention to detail and careful quality control will always be essential for achieving the best possible results.

### 1.1.4. Mechanics and Characterization of Carbon Fiber Properties

Understanding the behavior of carbon fiber during the spreading process requires the characterization of carbon fiber tow properties. Several properties, such as fiber diameter, orientation, and waviness, can affect the behavior of carbon fiber tows during spreading. This section provides a review of the different techniques used to characterize carbon fiber properties.

#### Friction properties

The quality of a carbon fibre, or a tow of fibres that is, greatly influences the properties of the final part that is to be made with said fibres. It is known that the matrix material, in a composite part, adheres to the fibres. This adhesion is dependent on the quality of the outer surface of the fibre. Therefore, if the fibre quality decreases, the overall part properties will change as well [22]. In the worst case, fiber breakage occurs. Breakage of a fibre results in an inability to carry a continuous load, thereby reducing the overall strength of a part. In reality, the broken fibre will still carry some load, since the stresses can be transferred via the matrix material. Still, breakage of a fibre is the most catastrophic damage that can occur to the fibre. It is assumed that this will then also have the most notable effect on the part as a whole.

A study has been performed which aimed to find a correlation concerning normal loads and tow-on-tool contact friction [23]. In this case, an experiment was conducted to simulate the effect of weaving tools on carbon tows. This differs from bar tow spreading, but can provide insightful information since the physical phenomenon, tow on tool contact, is comparable. A diagram of the experimental setup is displayed in figure 1.8. For this experiment, the amount of broken fibres is quantified according to the 'hairiness' of the local region. A side view of the the processed tow is taken via a camera and converted to grey scale. Based on the greyness per area, a value for tow quality can be assigned. The samples were also tensile tested [23].

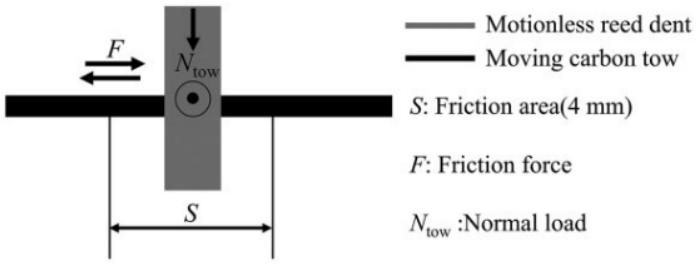


**Figure 1.8:** Diagram of experimental setup of tow-on-tool experiment [23]. The reed is made from stainless steel.

The effect of normal load on friction force was examined. From this, the graph in figure 1.9 is obtained. It is found that the normal load is not directly proportional to the friction force. Rather, the results indicate a correlation according to equation 1.2 which was mentioned earlier. For a further look into the F-N relationship, attention is given to the adhesion theory of friction which states equation 1.3 [23].

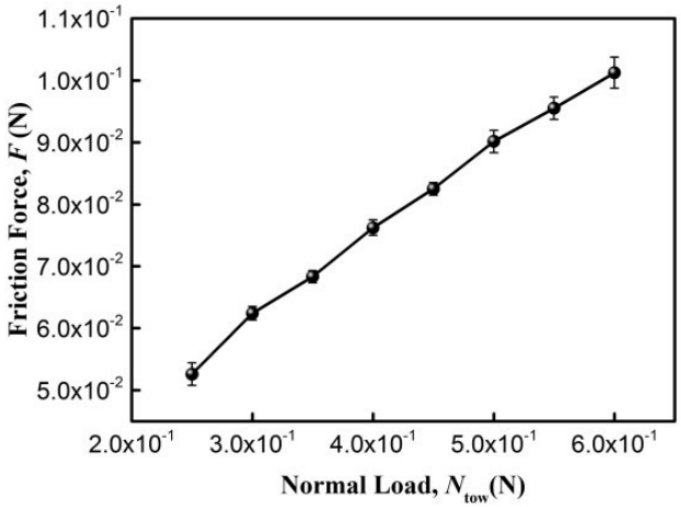


**Figure 1.9:** Normal load vs. friction force [23].

$$F = A_r \tau \tag{1.3}$$

For which $A_r$ the real area of contact between the tow and the tool, and $\tau$ is the shear strength at the interface of two given materials (which is generally assumed to be a constant).

If adhesion theory of friction holds true for carbon fibre tows, $A_r$ will determine the friction force $F$. The contact area of a single filament can be determined via the Hertz contact model. An equation, describing the relation between real contact area $A_r$ and normal load $N$ is defined according to equation 1.4 [23].

$$A_r = n_{fil}\sqrt{\frac{RL}{375E\pi}}N_{tow}^{\frac{1}{2}} \tag{1.4}$$

For which $n_{fil}$ is the number of filaments, $R$ is the radius of the carbon fibre filament, $L$ is the width of the reed, $E$ is the material equivalent modulus of elasticity, and $N_{tow}$ is the normal load acting on the tow. The equation can be simplified for fitting, and can then be written as equation 1.5.

$$A_r = kN_{tow}^{n} \tag{1.5}$$

It has been found that the fitting parameter $n$ corresponds closely for equations 1.2 and 1.5. Therefore, the alternative method of describing correspondence between friction force and normal load is considered reasonable [23].

It is often assumed that the Capstan equation, from 1.6, is true for tow spreading. The Capstan equation is generally utilized to analyze friction in a belt wound around a cylinder (capstan). This equation relates the tensile force on one side of the belt, T2, to the tensile force on the other side, T1, and is derived under several assumptions. These include a rigid capstan, a 1D structure of the belt, and no bending rigidity or shear deformation. Although this equation also has exponential factors to describe the tension properties of the situation, it states that the tension ratio is solely dependent on the wrap angle and friction coefficient and ignores the real contact area. It can be argued however, that a change in real area, and thus mechanical interlocking capabilities in the micro-scale, is physically the same as a change in friction coefficient $\mu$. This makes equations 1.5 and 1.6 comparable.

$$\frac{T2}{T1} = e^{\mu\phi} \tag{1.6}$$

Where $\mu$ is the friction coefficient and $\phi$ is the wrap angle. This equation demonstrates how the ratio of tensile forces changes exponentially based on the product of the friction coefficient and the wrap angle.

A different paper is published in which the influences of tension and relative velocity on friction are examined, using a Capstan-based setup which was earlier displayed in figure 1.5 [24]. It was found that both tension and relative velocity exhibit a positive correlation with the friction coefficient [24]. Initially, this may seem contradictory with equation 1.4. However, as the tow is tensioned, real contact area $A_r$ increases by which the friction coefficient also increases.

For relative motion the following can be said. If a change in relative velocity is imminent, the present static friction (between tow and rod) will initially keep the filaments from moving along and a small strain is induced in the fibres. This causes an elastic deformation. The greater the relative velocity is, the greater this deformation will be. A larger deformation in turn causes a larger difference in tension, comparing one side of the roller with the other side. The increase in tension then leads to a higher coefficient of friction [24]. This case is slightly different for when a relative motion is already present. In this case, increasing the relative velocity results in a reduction of relaxation time of the fibre: thus less deformation. As the tension difference increases, the friction coefficient increases [24]. Figure 1.10 shows a measurement of the effects of tension and relative velocity on the friction coefficient.

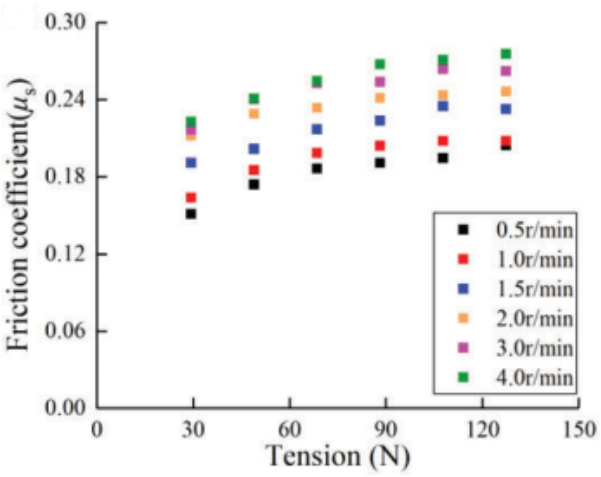


**Figure 1.10:** Tension and relative velocity vs. friction coefficient [24].

Based on their findings and equation 1.2, a fitting equation is proposed for the relation between the friction coefficient and the relative velocity. This can be seen in equation 1.7 [24]. This equation is similar to other Capstan based non-linear equations for determining the friction coefficient, but with the addition of a term for relative velocity [24].

$$\mu = k(\frac{T}{R})^{n-1}v^m \tag{1.7}$$

For which $v$ is the relative velocity between tow and rod, $R$ is the radius of the roller, and $T$ is the tension in the tow. $m$ and $n$ are fitting parameters.

For a discrete element approach, an equation for the normal force acting on a filament as it passes over a spreader bar is given in equation 1.8 [16].

$$f_n = \frac{T_i}{R} \tag{1.8}$$

For which $T_i$ is the tension in the filament and $R$ is the radius of the spreader bar. Note that $f_n$ is a value defined per unit length. Therefore, the normal force $f_n$ only depends on the tension in the filament, $T_i$, and the radius of the spreader bar, $R$. This equation is, however, derived for use in a discrete element method. Because of this, equation 1.8 only holds for small values of theta.

### Fiber Architecture

In order to develop a better understanding of the variations and architectural aspects that occur within a carbon fiber tow, this section will briefly discuss a previously made characterization descriptor named *Differential Tortuosity* from a study with the goal of characterising the microstructural organisation of carbon fibre filaments in unidirectional composites [25].

Tortuosity is a parameter which is used in the context of permeability of fibre bundles [25]. It is a definition of the deviation between the permeation path and a straight line, of which the latter is the most direct way of travel. Tortuosity can be described according to equation 1.9.

$$\tau = \frac{L}{L_0} \tag{1.9}$$

For which $L$ is the length of the path that the fluid travels, and $L_0$ is the actual traveled path of the fluid.

Equation 1.9 can be related to fibre architecture, where $L$ is the length of the filament and $L_0$ is the length of a perfectly straight filament. Hereby, the value of the tortuosity for any fibre is $\tau \geq 1$. An alternative definition exists, which is defined as *Differential Tortuosity*. This is the difference between an actual real fibre and a theoretical straight fibre which is aligned with the scan volume. Differential tortuosity is defined according to equation 1.10 [25].

$$\tau = \tau - 1 = \frac{L - L_0}{L_0} \tag{1.10}$$

For which $L$ is the length of the fibre and $L_0$ is the length of the scan volume.

This approach of tortuosity provides a more intuitive value as the differences between theoretical and real-world are provided in a logarithmic fashion. Also, the base value is now 0 instead of 1 [25]. In figure 1.11, an example of differential tortuosity of a fibre is shown.

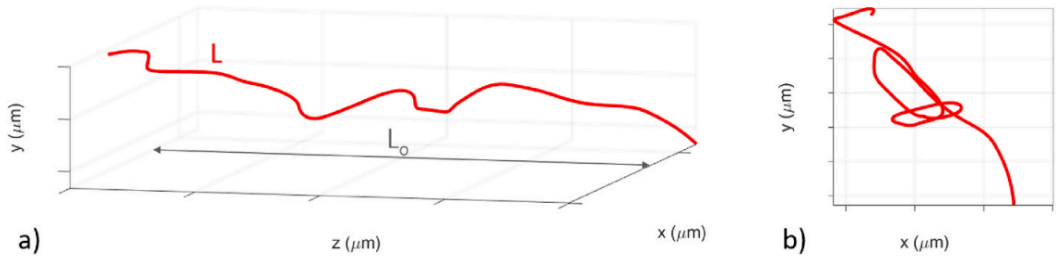


**Figure 1.11:** Differential tortuosity of a fibre in a) 3D view and b) 2D view [25].

As can be summarized from this section and as can be seen in figure 1.11, fibers in a sections of carbon fibre can have very unpredictable pathways in their length direction. For new innovative manufacturing, with which the goal is to predict the material properties as best as possible, descriptors as *differential tortuosity* are beneficial for characterizing the material and quantifying the method-inflicted alterations hereof. This is because these properties can have an influence on the spreading capabilities of a tow. Fibres with a high amount of differential tortuosity can potentially mechanically connect several various fibres. This may result in the prevention of (lateral) fibre movements, and thereby a reduction of the spreading range.

### 1.1.5. Analysis and Modeling Techniques for Carbon Fiber

Several data analysis and modeling techniques can be used to analyze and model the spreading of carbon fiber tow. These techniques can provide insights into the quality and consistency of carbon fiber reinforcement and the tow spreading process and help identify areas for improvement. Some of these techniques are listed below.

- Image Analysis: Images of the carbon fiber tow can be captured using a camera, microscope, or other imaging system, and then analyzed using image processing software [26]. This analysis can provide information on the spacing and alignment of the individual fibers, as well as the presence of defects such as breaks or clumps of fibers.
- Statistical Analysis: Statistical analysis can be used to identify patterns and trends in the data, as well as to determine the statistical significance of any differences between samples [27]. This analysis can be used to identify the factors that affect tow spreading quality, such as the type of sizing used or the speed of the spreading machine.
- Computational Modeling: Computational modeling involves creating a mathematical model of the process and then simulating it using a computer. This analysis can provide insights into the mechanics of the process and can be used to optimize the process parameters to achieve the desired properties in the final product [28].

- Machine Learning: Machine learning algorithms can be trained on data from the tow spreading process to identify patterns and predict outcomes. This analysis can be used to develop predictive models that can help optimize the process and improve product quality [29].

Data analysis techniques can be used to analyze the spreading of carbon fiber tow and provide insights into the quality and consistency of the process. These techniques can help identify areas for improvement and optimize the process parameters to achieve the desired properties in the final product. Image analysis, statistical analysis, computational modeling, and machine learning are some of the data analysis techniques that can be used for this purpose.

## 1.2. Objectives and Research Questions

The main objective of this study is to design and construct a carbon fiber tow spreading machine and use it to characterize and quantify carbon fiber tow properties during the spreading process. This covers the implementation of new measurement techniques to assess the straightness, degree of spread, and applied damage of the tow. The specific research questions that this study seeks to answer are mentioned below.

The main research question is:

- What properties are relevant during carbon fiber tow spreading and how can these be measured?

Following from this, the sub-questions are:

- What is the behaviour of friction during tow spreading?
- Can resistivity measurements be used to analyze the carbon tow properties?
- Can optical analysis be used to analyze the carbon geometrical properties?

Next to these research questions, significant practical questions are also listed which will be answered via the methodology:

- How can a tow spreading line be designed and made to accommodate relevant research?
- How can conductivity of a carbon fiber tow be measured?

## 1.3. Significance of the Study

The findings of this study can have great significance for the carbon fiber industry, as they could provide insights that can be used to optimize carbon fiber manufacturing processes and improve the quality of carbon fiber products. More specifically, knowledge about uni-directional carbon fibre tape production will be broadened. Applied damage during manufacturing results in a final part with increased damage, and thus reduced mechanical properties. Investigating tow spreading, a significant part of UD tape production, can contribute by developing a better understanding on how particular measurement and processing steps influence the material at hand. The study's methodology is particularly noteworthy, as it involves the design, assembly, and use of a new carbon fiber tow spreading machine and the implementation of custom optical analysis software and electrical analysis.

By using this new machine, the study may be able to help achieve highly consistent and uniform carbon fiber tow spreading, which is a critical step in the carbon fiber manufacturing process. The custom optical and electrical analysis may also allow for highly accurate measurement and characterization of the tow spreading process, possibly enabling identification key factors that affect the quality of the process.

The insights gained from this study can be used to improve the overall efficiency and quality of carbon fiber manufacturing, which has significant implications for a wide range of industries that use carbon fiber materials. For example in the aerospace industry, where the demands for high-quality carbon fiber products are particularly high, the findings of this study could lead to the development of new, more reliable manufacturing processes that can produce high-quality carbon fiber materials at a lower cost. Furthermore, the study's methodology, which combines advanced engineering techniques

with advanced data analysis techniques, can also contribute to the advancement of carbon fiber research. By combining these two fields, researchers can gain a more comprehensive understanding of the carbon fiber manufacturing process, which can lead to the development of new and innovative manufacturing techniques.

In conclusion, the findings of this study can have significant implications for the carbon fiber industry and can contribute to the advancement of carbon fiber research. The study, which involves the use of a new carbon fiber tow spreading machine and the implementation of custom optical and electrical analysis, represents an innovative approach to carbon fiber manufacturing research and has the potential to drive new developments in this field.

## 1.4. Scope and Limitations

This study focuses on the design and construction of a carbon fiber tow spreading machine and the characterization of carbon fiber tow properties during the spreading process. The study aims to provide insights into the behavior of carbon fiber tow during spreading, which can be useful in improving carbon fiber manufacturing processes.

However, it is important to note that this study has some limitations. First, the experimental setup is limited to laboratory-scale conditions and may not be representative of industrial-scale conditions. Second, the study only considers a single type of carbon fiber tow, and the results may not be applicable to other types of carbon fibers. Finally, while the study uses several techniques to analyze the data, other data analysis techniques may be applicable and could provide additional insights.

Despite these limitations, this study provides a comprehensive analysis of carbon fiber tow properties during the spreading process and offers valuable insights that can be used to optimize carbon fiber manufacturing processes.

## 1.5. Overview of the Methodology

The methodology for this study will involve designing and constructing a carbon fiber tow spreading machine and conducting experiments to characterize the carbon fiber tow properties during the spreading process. The experiments will include the measurement of friction, conductivity, and geometry as part of the experimental setup. The acquired data will be analyzed using Python.

## 1.6. Organization of the Report

Chapter 2 describes the methodology used in this study, including the design and construction of the carbon fiber tow spreading machine and the experimental setup. Chapter 3 presents the experimental results from the investigation towards carbon fiber tow properties during the spreading process, including the effects of friction and conductivity on spreading behavior, the data analysis using optical analysis, and the Capstan investigation. This chapter also discusses the implications of the results and their potential application in optimizing carbon fiber manufacturing processes. Chapter 4 provides concluding remarks and suggestions for future research. Finally, appendices contain additional technical details on the carbon fiber tow spreading machine design and construction, experimental setup, data analysis, and raw experimental data.

# 2

# Methodology

In this chapter, the methodology is described and explained in terms of three main themes: the machine design, experimental setup, and data acquisition and analysis methods. First, the design and construction of the machine are shown in section 2.1. This goes over both the mechanical design considerations and assembly of the tow spreading line as well as the electrical connections applied. Following this, is a section on the experimental setup used, specifically in section 2.2. This lists the research plan decided upon, including an explanation of the Capstan equation that is to be investigated. This section also further lists and describes the to-be-performed experiments. After this section, more detail is presented on the techniques used for capturing and analyzing the experimental results in section 2.3. In this section, measurement techniques to quantify the tow behaviour are discussed. This ranges from well-known tension measurements, to innovative conductivity measurements and custom optical analysis.

## 2.1. Design and Construction of the Carbon Fiber Tow Spreading Machine

In this section, the main attributes of the design and assembly of the tow spreading line are presented. This first goes over the design considerations, where previously found notes are presented and machine requirements and options are mentioned. This is followed by a subsection on the assembly and main functions, where the broad characteristics of the machine, as decided on, and its functions are shown. The machine electrics are discussed in the final subsection. For specific details on the configuration and specifications of the machine and its components, please visit Appendix A.

### 2.1.1. Design considerations

As is evident from chapter 1, related research has been performed by TU Delft beforehand [15]. For these research studies, a tow spreading line had been build. It was noted that certain improvements are recommended, derived from usage of the line. In the list below, the most notable points of feedback are named. This list is based on the user experience of researchers with experience on the previously existing line.

- Alignment - the tow had issues with moving in a straight path and deviated frequently.
- Stiffness - the tow spreading line lacked sufficient stiffness. Due to this, its geometry often changed which has the tendency to affect measurement data.
- Space for sensors - even though the number of sensors was limited, the machine lacked sufficient free mounting points for additional sensor integration.

- Wrap angle adjustment - as variating wrap angles are one of the main requirements for a experimental tow spreading line, accurate and quick adjustment is wanted. The previous tow spreading line had various issues in terms of this aspect.

Besides these points of feedback, several general functions should be included in the tow spreading line. These are again listed below.

- Pulling unit - a unit which tensions and feeds the tow through the system is required.
- Mechanical brake - a unit which is capable of providing a (variable) pre-tension on the tow.
- Bar spreading unit - since the research is focused around the physical act of bar-spreading tow, a spreading unit is one of the main necessary functions of the line.
- Sensor attachment points - to obtain experimental data, sensor implementation is required. For this it is important that the tow line has sufficient mounting capabilities.

It has been decided that the required changes and functions exceed the capabilities of the previously built tow spreading line. Therefore, it has been decided to develop a new tow spreading line from the ground up to accommodate all listed functions. By taking this approach, room for extensions arises. A new type of carbon properties sensor is to be developed and implemented based on the electrical properties of the material at hand. More about this sensor can be read in section 2.1.3. Also, the design and assembly of a completely new line offers the possibilities to upscale already existing functions. The pulling unit has been approached this way by also designing and building it in a completely new fashion. This is such that the pulling force is increased, making the machine capable of a greater range of tension values. The size is also to be increased, in terms of frame thicknesses and general volume. This has been chosen to increase stiffness and to accommodate for multiple integrated functions. It can be derived that an increased number of functions could lead to an increased value of friction in the system, which is then solved by the new pulling unit design.

To develop the new tow spreading system, a design is made first. For this, the above-mentioned requirements and notes (on previous comparable systems) are expressed in terms of equipment. Below in this section, the main part design considerations are explained. After the design is made, parts are selected and ordered. Then, assembly commences during which the tow spreading line is built. A morphological table hereof is given in table 2.1. For a further and more detailed description of the tow spreading line, please visit section 2.1.2 and Appendix A.

#### Frame

A previous setup implemented aluminium extruded profiles with a cross-sectional dimension of 15x15 mm. These extruded profiles offer the convenience of quick customization and various configurations. For the new design, these properties are recognized and considered. This and other considered frame possibilities are explained below. The options for the frame assembly relate to the overall assembly type and frame struts (extruded profiles).

For the overall assembly type, two methods are considered: solid and modular. *Solid assembly* means that the entire structure is generally one construction. This means that all connections are fixed. If one wants to move or replace certain aspects, (partial) disassembly is required. The benefit of this would be the integrity of the system, as a completely connected system is expected to have a more uniform stiffness and better predictability. The disadvantage comes when edits are to be made, or functions are to be changed. A modular assembly implies that the machine is divided into sections which are build separately. A general mainframe would be required to house these separate modules. The advantages of such an assembly are that it can be quickly adjusted or tuned, in cases of new future research or when the machine does not perform as wished. Such an assembly can also be moved around more easily in cases of changing work spaces, making it more flexible. Implementing the idea

of sub-modules would also result in generally shorter distances for the frame-struts to span, reducing bending deformations. The disadvantages of an assembly of this type are, firstly, an increased amount of required building and designing time so that the parts are compatible with one another. Secondly, sub-modules require their own frame elements, resulting in increased assembly costs.

Considering the earlier-mentioned stiffness issues with the previous research setup, the following options are considered as possible for the new iteration: original 15x15mm extruded star-profiles, 40x40mm extruded star-profiles, 40x40 extruded closed profiles. The novel tow spreading line is to have larger machine dimensions than the previous version. Since 15x15mm was already not rigid enough, it will surely not be adequate for the new spreading line. The named cross-sectional dimensions have been chosen for the fact that these profiles are known to be rigid. Since possible future research might upscale the parameters, it is speculated that such an over-engineered solution is adequate to future-proof the design. Comparing star-profiles and closed profiles, the main difference is ease of assembly and miscellaneous attachments. This is easier to perform on the star-profile as it has rails cut out over its length direction. The closed profiles are expected to be cheaper.

#### Pulling unit

The pulling unit can be considered the heart of the tow spreading line. Also, this can be seen as the most complicated section as it includes various different design choices. The considerations for the pulling unit design are as follows: motor selection, axle design, and drivetrain selection.

For the motor selection, the main concern is the pulling speed and pulling torque. As is mentioned earlier, the line is expected to be used for future research in which the parameters are yet unknown. Several possibilities arise from this. The currently used stepper motor can be re-used. This would imply similar pulling performance as in the previously conducted research. An alternative possibility is the integration of a stronger, over-engineered, pulling motor. This implies an extension to the pulling range, future-proofing the design. Besides these two considerations, it is also important to decide between a brushed DC motor and a stepper motor. Brushed DC motors generally are cheaper and less complex to drive. However, stepper motors have an increased level of control where discrete steps can be used to precisely edit motor parameters.

Considerations of the axle design can be distributed in mainly three categories: number of axles, diameter, and material. Pulling the tow requires a great amount of friction between pulling axles and tow. Friction can be increased by increasing the number of pulling axles. A similar effect can be achieved by increasing the axle diameter or to choose a rougher material. A consideration has to be made, since an increase in friction is expected to additionally damage the out coming tow. Although, it has to be noted that the relative motion between pulling axle and tow is close to zero such that pure friction forces are not expected to be very high. Researchers in the topic have noted [30] that the tow, being stretched over a rod with a relative motion of zero but an absolute motion of non-zero, experiences small forces which cause the tow to minimize the internal system energy. This is said to homogenize the tow, showing an increased effect when multiple axles are used where the friction can be approximated as zero. Apart from the friction, bending of the axles should be considered as the tensions in the tow here are the highest in the entire line. Generally, stainless steel is considered strong and cost-effective. Other options exist, like aluminium, which would reduce the weight of the pulling unit significantly. Increasing axle diameter provides a larger contact area such that the pulling axles have a greater grip on the tow. However, the axle diameters should be manageable and applicable in the spreading line. Therefore, axles too big are considered not effective.

Drive selection relates to the manner in which the motors torque is transferred to the carbon tow. This paragraph does not cover the electrical driving system for the motor (this is covered in section 2.1.3). Two main methods of providing power from the motor to the pulling axles is considered: belt-drive and chain-drive. Generally, chain drive is considered the stiffer option since steel chains have less elasticity than canvas driving belts. However, this can also be considered negative, as some flexibility could dampen vibrational noise in the system. Due to the higher stiffness of chains, they are known to be more efficient in transmitting their power. Belts, however, are lighter and would therefore reduce

the weight of the module.

### Spreading system

The spreading system is the main function of the novel tow spreading line. Several aspects of this are considered; spreader bar diameter, spreader bar surface material, number of spreader bars, wrap angle adjustment, and relative velocity.

Spreader bar diameters can vary based on the application. In the previous study, bars with a diameter of 20 mm are used. Decreasing the diameter will bend the fibers more, breaking up sizing and therefore influences spreading behaviour. Greater diameters result in larger friction areas, albeit with lower stress, in which the fiber spreading can occur. Implementing differently sized spreader bars can result in new discoveries on the diameter parameter influences. On the other hand, using the existing diameter provides a certainty to the process such that other variables can be observed more closely. Also, retrieved values can be compared more conveniently to known previous experiments.

The surface material of the spreader bars can be chosen based on the required friction properties. As mentioned, friction is the driving force behind the spreading of tow. However, increased friction results in increased tow damage. The options for this parameter are to stick to previously used Topocrom finished spreader bars, or to experiment with new coatings. Again, using various new coatings can provide new information on the process. On the other hand, using the existing coatings provides certainty of the process as also mentioned above.

The number of spreader bars is a free variable which depends largely on what one wants to investigate. Research has shown that spreading behaviour, over multiple bars, reaches an asymptotic value at a count of approximately five spreader bars [15]. Using more bars will increase the friction in the system, putting more strain on the line. Using less bars makes the procedure more simple to manage and marginally cheaper, but could potentially hinder future studies in terms of flexibility. It should also be considered how much space is available to implement spreader bars into the spreading line.

To study the effect of wrap angle and relative velocity on the spreading behaviour, spreader bar mounting positions should be variable such that the wrap angles can be changed. Various options have been considered, explained below with the help of images.

For wrap angle adjustment within a defined volumetric dimension, which is the reserved space for the spreading unit, the spreader bars should be variable in relative height from one another. To achieve this, an electrically controlled system can be used which rises the bar up and down via a threaded vertical axle or a driving belt. The driving belt has the benefit that it can move quicker. The thread generally would mean a more accurate vertical position. Apart from this, the adjustment can also be performed by hand. If the spreader bar is span between two pillars, additional holes can be made in said pillars such that a variety of wrap angles becomes possible.

Relative motion, of the moving tow and spreader bar, can be adjusted in two ways: by adjusting the pulling speed of the tow, and by rotating the spreader bar itself. Adding rotational functionality to the spreader bars would increase the relative velocity operating interval, however, it would also increase machine complexity. Below in figure 2.1a, two configurations are shown which both sport automatically adjustable wrap angles and relative velocities. Note that both shown options have spindle axles for vertical adjustment. Belt-drive options were also considered. However faster, these are deemed less accurate than the spindle adjustment. This is partly due to the fact that the rubber-type material is more prone to stretching than steel. Models of these preliminary spreader-bar concepts, including annotations and a detail, are added to Appendix A.

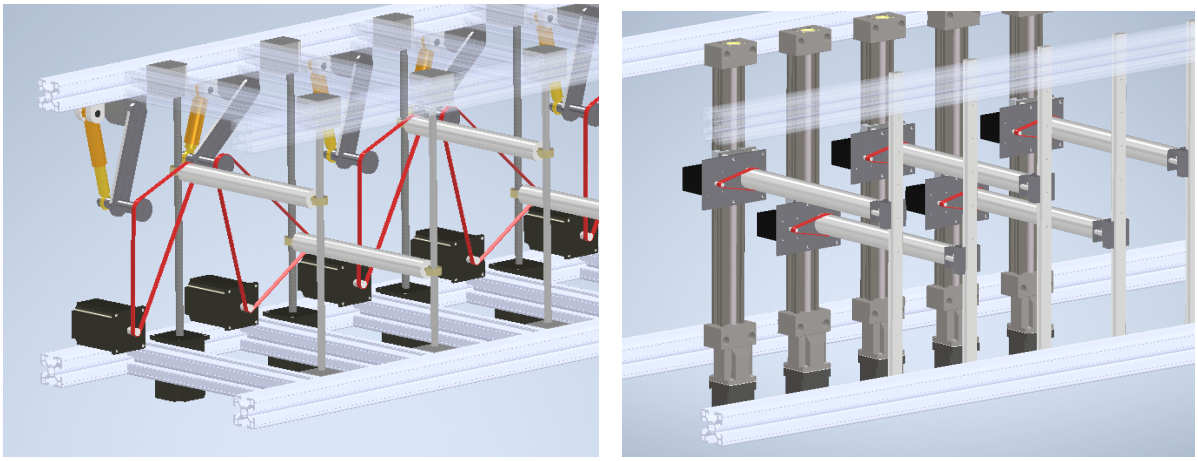

**(a)** Image of spreader concept 1.

**(b)** Image of spreader concept 2.

**Figure 2.1:** Two spreader system concepts.

### Mechanical brake

For the brake system, used to generate pre-tension in the system, several pre-build items can be used. The considered items include a spring-loaded mechanical brake, friction strap brake, and eddy-current electrical brake. One of the benefits of the spring-loaded brake is predictability, as previous experiments with this item have been performed and experience is gathered on its performance. Another major benefit is the cost consideration. As the item is already in-house, no additional costs would be required. Friction strap brakes also work via mechanical principles, using a tightened strap to prevent the brake from rotating freely. This brake would extend the range, compared to the spring-loaded brake. However, the increase is not significant. Also, additional costs would be generated. Eddy-current brakes are objectively the most useful, as it is possible to electronically control and measure the pre-tension values that are applied. A downside of this brake is complexity, of which the main disadvantage is increased costs. Eddy-current brakes are quoted around one to two orders of magnitude higher in terms of price.

### Sensor attachment

To be able to implement sufficient sensors in the line, two main things should be considered: empty space for the sensors, and attachment points for these sensors. When using a closed profile frame, holes can be drilled locally to implement mounting points. A disadvantage of this would be the required effort and accuracy each time a new sensor (location) is chosen. Alternatively, 3D printed or milled mounting adapter can be used. For this it has to be mentioned that 3D printed mounts generally are not very stiff. Milled steel adapters would suffice but are generally very expensive.

If star-profiles are used to build the frame, attachment points are excess as every empty section of frame can be used to attach a sensor to it. To do this, small metal parts can be quickly made from steel tube sections, by drilling appropriate holes and thereby creating a versatile, strong, and cheap mounting adapter. For some connections, the part could be bolted directly to the frame components. 3D printing can also be used in this case, for quickly fitting e.g. curved connections.

### Alignment

Alignment of the machine, and thereby the tow passing through the machine, is crucial for user experience and reliable machine performance. To achieve alignment, the following options are considered. Firstly, alignment can be achieved by relying on the straightness of the line in general. If the line and all its components are balanced and straight, the tow should run straight. Secondly, double-vertical guides can be used to guide to tow straight. However, for this the tow has to be twisted 90 degrees back and fort. This could induce gaps or twists in the tow. Another possibility is to use several concave rollers in the system, such that the tow fall to the center of the roller due to system tension. A disadvantage hereof would be the lateral compression that occurs if multiple strand all try to do this at the same time, it could namely lead to induced gaps and overlays within the tow.

### Collecting

Collecting of the spread tow refers to storing the tow on a collecting reel. However, when dry carbon fibers are spooled unto a reel, their architecture changes. To prevent this, a binder would have to be applied before collecting the tow. This in turn would require an additional function within in the machine, in which the tow is consolidated or cured with an applied binder substance to lock its geometry.

### Safety measures

Using a powerful motor, driving equipment, and sensitive carbon fiber brings risks along. To manage these risks, some form of safety has to be implemented into the spreading line design. Safety considerations are made for two main machine sections: the pulling unit and the general complete system.

For the pulling unit, it has to be stated that significant levels of torque can be present in the system. Since the power is guided from the motor to the axles via gears, moving parts exist. For this it is considered very important that such movement does not occur per accident in situations where harm could be done. One implementation is to add laser sensors to the pulling unit, such that movement in the area of the dangerous parts would interrupt the current flow and stop the system. Disadvantages hereof are the added complexity and possibility for interference, which could interrupt ongoing research for false alarms. Alternatively, a double activation system can be applied to the motor. Then, the motor can only be turned on if both conditions apply. This latter option does still require the user to be careful with the moving components, but reduces the chance that the line turns on accidentally when researchers are not paying attention. Alternatively, a shield could be placed to cover the modules. This is further mentioned below.

Due to the fact that carbon rovings are manipulated during the process, loose fiber elements and carbon dust is prone to be present. Since this is considered a health hazard, a proposition is made to cover the operating line with Plexiglas panels and apply suction at the top of the line such that these dangerous elements are safely removed. Adding Plexiglas does contribute with the safety of the pulling unit, since it is less likely for someone or something to interact with this unit. Generally, this also implies that adjustment of the line is more difficult. The Plexiglas can be applied in large single panels per side, such that it is relatively easy to implement. If work on the line is required, panels can be removed. Another option is to divide the side panels into small sections, and add hinges to these sections. Then, certain parts can be easily accessed and worked on while keeping protection on the rest of the line which is not being worked on.

Below in table 2.1, a morphological chart of the relevant considerations for the line are displayed. The chosen options are printed in blue. In the following section 2.1.2, these choices are further mentioned.

| *Function* | **Option 1** | **Option 2** | **Option 3** |
|---|---|---|---|
| Frame Assembly | Modular | Solid | |
| Frame Profiles | 15x15mm star | 40x40mm closed | 40x40mm star |
| Motor Selection | Stepper | Brushed DC | |
| Pulling Axles $\phi$ | 40mm | 60mm | 80mm |
| Number of Axles | 3 | 5 | 8 |
| Drivetrain | Chain Drive | Belt Drive | |
| Spreading Bar $\phi$ | 15mm | 20mm | 25mm |
| Surface Material | Topochrome | Stainless Steel | |
| Spreader Bar Count | 4 | 5 | 6 |
| Wrap Angle Adjustment | Manual | Automatic | |
| Relative Velocity | Rotating Bars | Fixed Bars | |
| Mechanical Brake | Spring Loaded | Friction Strap | Eddy-Current |
| Alignment | Natural Alignment | Double Rollers | Concave Bars |
| Tow Collection | Collecting System | No Collecting System | |
| Pulling Unit Safety | Double Activation | Laser Sensors | |
| Carbon Dust Blocking | Single Panel | Sectioned Panels | |

**Table 2.1:** Morphological Overview of Design Considerations.

### 2.1.2. Assembly and main functions

Partially based on the methodology of previously performed studies, a new tow spreading line is designed and manufactured to conduct the research at hand, and, to be used for further studies for which these machine functions are requested. The design decisions explained in this section have been mentioned in the section above, where they are compared to alternative options. In this section, the primary machine properties are mentioned. A more detailed overview of the machine design aspects, as well as a CAD concept design, can be seen in Appendix A. Note that electrical diagrams and corresponding information are explained in section 2.1.3.

#### Frame

The new carbon tow spreading line is designed according to a modular principle. A mainframe is placed, in which modules, accommodating functions, are installed. Due to the modular design, different modules can be replaced and exchanged, making the tow spreading line suitable for various types of research towards the topic of tow fibre spreading. During this study, a single configuration is set-up and used throughout. However, this design method was decided upon to initiate and support further research into the field and possible on-the-fly adjustments based on problems encountered during the building process or during general usage. The main- and sub-assemblies of the line use 40x40 mm aluminum extruded profiles for the general geometry. The profiles have been chosen as star-profiles so that no extra drilling work has to be performed to connect the frame pieces with each other, and so that sensor attachment can be done at any point on the line. Dimensions have been chosen based on estimations of all the sub modules, to which additional space is added for sensor placement and straightening of the tow after it leaves the reel.

#### Pulling unit

A brushed 24V DC motor has been chosen as power train of the line. The motor is capable of pulling the tow at speeds ranging from 4 to 7.5 cm/s in a complete line including all sensors, using a drive gear with 17 teeth. Slower or faster pulling speeds are possible by swapping the drive gear to a gear with a lower or higher teeth count. An additional gearbox could be added to even further extend the interval. The written code to control this motor is mentioned and shown in Appendix B. In order to maintain a velocity, the contact between tow and pulling axles should be maximal. To ensure this and provide surface contact, an additional roller is placed on top of the last axle which holds the tow down such that the steel axles can catch a grip on it.

The pulling unit, in figure 2.2, is responsible for delivering a pulling force on the tow via a set of five custom stainless steel rolling axles. The count and diameter (60mm) of these axles is chosen based on other pulling unit designs [30], the consideration that enough contact area should be present, and practicality of the build. The material has been decided on because of the fact that stainless steel is a generally strong and cost-efficient metal. These axles grip onto the tow via friction and pull it along. As the tow is pulled over and under these axles, forces act perpendicular on the tow which causes residual stresses to minimize and homogenize the tow [30]. Note that, since the axles rotate with the same speed as the moving tow, relative velocity is zero and therefore no friction-based spreading occurs. The axles are attached to the sub-frame elements via 22mm-inner roller bearings.

Connecting the power train with the pulling axles is the drive train, which has been chosen to be chain driven with an 8B simplex chain. The motor is mounted to the frame elements via a custom stainless steel adapter, recycled from discarded metal components. The gear attached to the motor has 17 teeth, as do the gears connected to the axles. Due to nature of this setup, pulling power and torque are not only variable via the driver software, but also mechanically. The above-mentioned velocity numbers are representative of the named gear ratio. The chain drive system is tensioned using a smaller gear with 10 teeth. Detailed motor specs, axle assemblies, and the drive train assembly can be further viewed in Appendix A. In figure 2.2, an image of the assembles pulling unit is shown.

**Figure 2.2:** Picture of pulling unit.

A side view of the pulling unit's assembly is displayed in figure 2.3. Here, separate components of the module are highlighted with tags. For the electrical details on the pulling unit assembly, please visit section 2.1.3 and Appendix A.

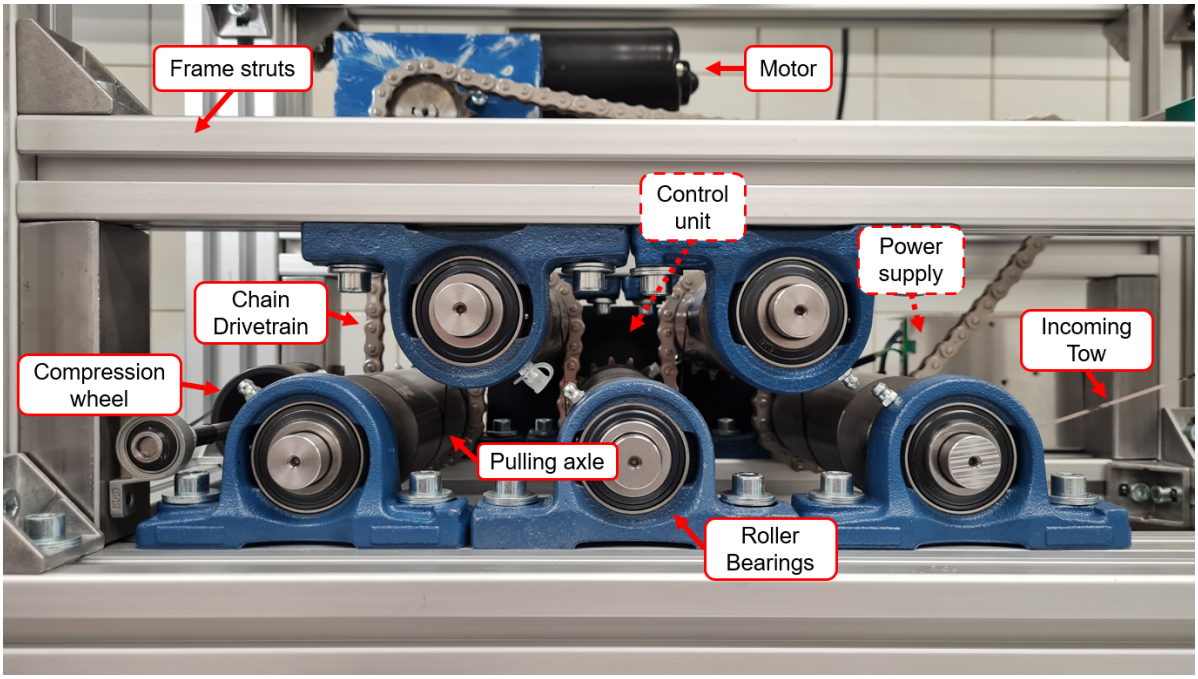


**Figure 2.3:** Side view of pulling unit with tags.

### Spreading system

The main function of the machine is the spreading of tows. In this study, the research principles are aimed towards the effects during bar spreading under e.g. various wrap angle installments. For this it is necessary to have multiple adjustable spreader bars. This has been solved according to the spreader bar system displayed in figure 2.4.

**Figure 2.4:** Image of spreaderbars.

This module is built using the above-mentioned 40x40 mm aluminum extrusions. 40x25 mm tube sections with 1 mm wall thickness, cut to a length of 320 mm and equipped with holes along the length direction, are placed in this module. The spreading unit contains four pairs of these tube sections, each supporting a topochrome coated spreading bar with a diameter of 20 mm. The topochrome spreader bars can be attached to the supports according to any supported layout, creating an arrange of various wrap angle combinations. Once the spreader bars are installed in the module, they are fixed and therefore resist rotational movement. Large benefits of this setup are firstly the manual adjustment capabilities, making it less reliant on additional software and actuating hardware to function reliably, which is convenient during research. Secondly, the setup can quickly be adjusted to fit other experimental setups or to just generally add improvements based on user experience. For example, multiple additional spreader bars can be quickly and cheaply installed when required. Thirdly, the costs of the applied setup are drastically lower than other considered setups.

### Mechanical brake

The spring-loaded mechanical brake, used in earlier tow-spreading research, is used for the current setup. The brake used for this setup is responsible for providing pre-tension on the tow. This brake can provide pre-tension values ranging from 3 to 6 N in a fully built tow line setup. For a more detailed view on the mechanical brake used in this line, please visit Appendix A.

### Sensor attachment

As explained above, star-profile extruded aluminium frame elements are used to construct the sub-modules and main-frame. Due to the nature of these profiles, sensor attachment can be done anywhere in the line. If a frame element is not conveniently placed, one can easily add an extra element into the particular sub-module to which the sensor can be attached. The sensors and the frame element are connected using custom adapters, displayed together with the sensors in section 2.1.3. Additional information on the frame elements and sensor attachment adapters can be found in Appendix A.

### Alignment

The tow spreading machine functions mainly via intrinsic straightness. A single double vertical roller set is used to guide the tow away from the reel. This roller set has been placed 1200 mm away from the reel, such that the vertical rollers have less of an influence on the tow geometry. This is due to the tow entering the rollers at a reduced angle with increased distance, as the tow moves from left to right when coming off of the reel.

### Safety measures

The pulling unit has been made with a two-stage activation. Instead of connecting the logic system and motor to the same power supply, the motor is connected to a separate power supply and the logic system is connected via USB power. Both have to be live for the pulling unit to be able to function. Therefore, accidentally turning the motor on, via the mechanical switch present, cannot in itself happen. The motor can only be activated once the single USB connection is plugged into a computer. Via this same single USB connection, the motor and all sensors are also controlled and monitored as is explained in section 2.1.3. This is such that the towline can only run if people are indeed working with it.

To combat carbon dust, Plexiglas sheets are cut and placed around the exterior dimensions of the line. Holes are created where connections have to be present, and on the top of the line. The top holes are in turn covered by suction vents to pull away the dust. For the current setup, single big sheets are developed which cover entire sides of the line. The line can be entered by disengaging the hooks, with which they are attached, and placing the Plexiglas away from the line.

An image of the assembled tow line can be seen in figure 2.5. Tags have been added to indicate the main items.

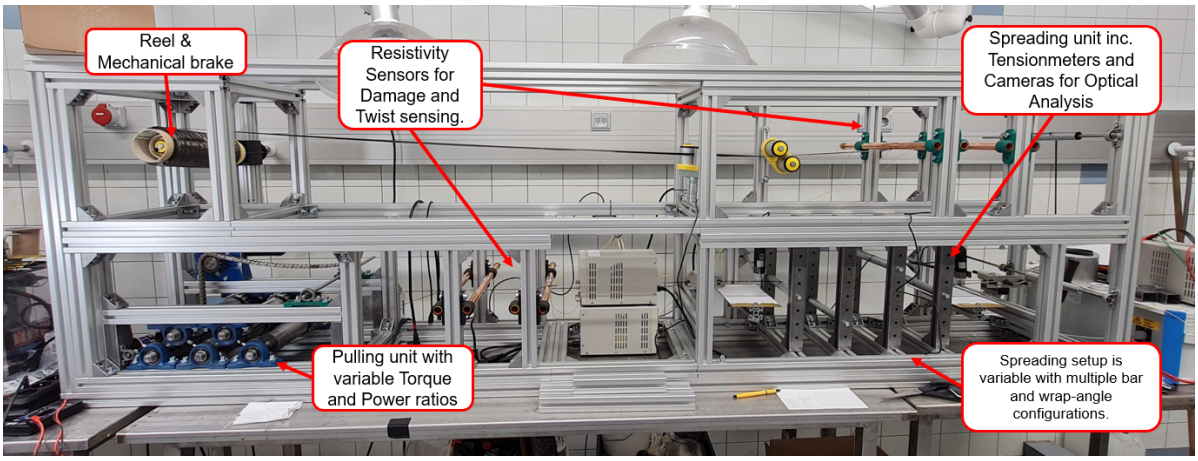


**Figure 2.5:** Image of assembled tow line with tags.

## 2.1.3. Electrics

The electric components of a carbon tow spreading machine play a crucial role in ensuring the smooth operation and efficient performance of the equipment. These components include a micro controller unit with an L298N driver, multiple power supplies, the wiring and other electrical functions for all systems on the line. The micro controller serves for controlling the motor in terms of direction and power. The power supplies ensure that the machine's systems receive a steady and reliable source of electricity, while the wiring diagrams provide a clear visual representation of the electrical connections and circuits involved. This section will delve into each of these components in more detail via a section on *Motor electrics* and *Sensor electrics*, showing how they contribute to the overall performance of the carbon tow spreading machine.

### Motor electrics

To enable and control the motor efficiently, a small circuit is made including an Arduino Uno and a L298N H-bridge driver module. These are wired to control the motor as can be seen in figure 2.6.

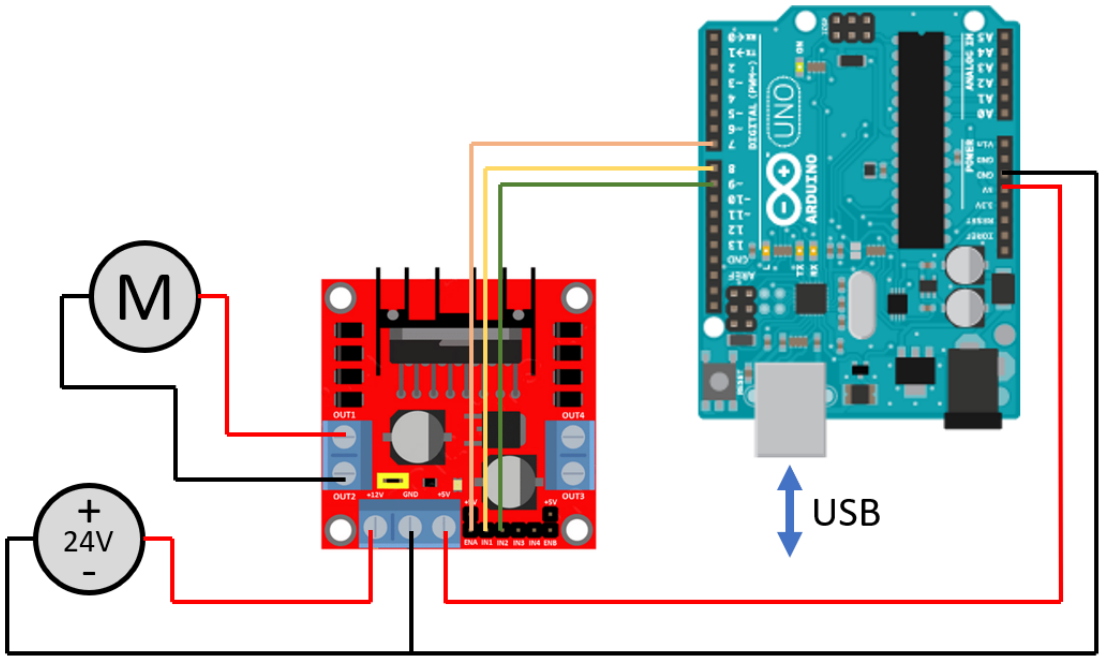


**Figure 2.6:** Wiring diagram for motor power and control.

The Arduino Uno module operates on a small section of code, which can be adjusted and uploaded live via the same USB connection that powers the logic system. Because of this, the motor speed (and less important, direction) can be adjusted on the fly within the available interval. The code can be read in Appendix B. As earlier mentioned, manually changing gear ratios can further extend the interval range.

### Sensor electrics

To be able to measure the friction values that act on the moving tow during spreading, tensionmeters are used. Two tensionmeters are installed in the same module as the spreader bar system. One tensionmeter is placed before the spreading unit, and one is placed after it. By measuring the tension before and after the relevant process, the friction force during the process can be determined via subtraction. One of the tensionmeters is displayed in figure 2.7. The tensionmeter exists out of a body and three rollers through which the tow passes. Based on the displacement of the middle roller, the tension in the tow is derived via a voltage measurement as is similar with a strain gauge.

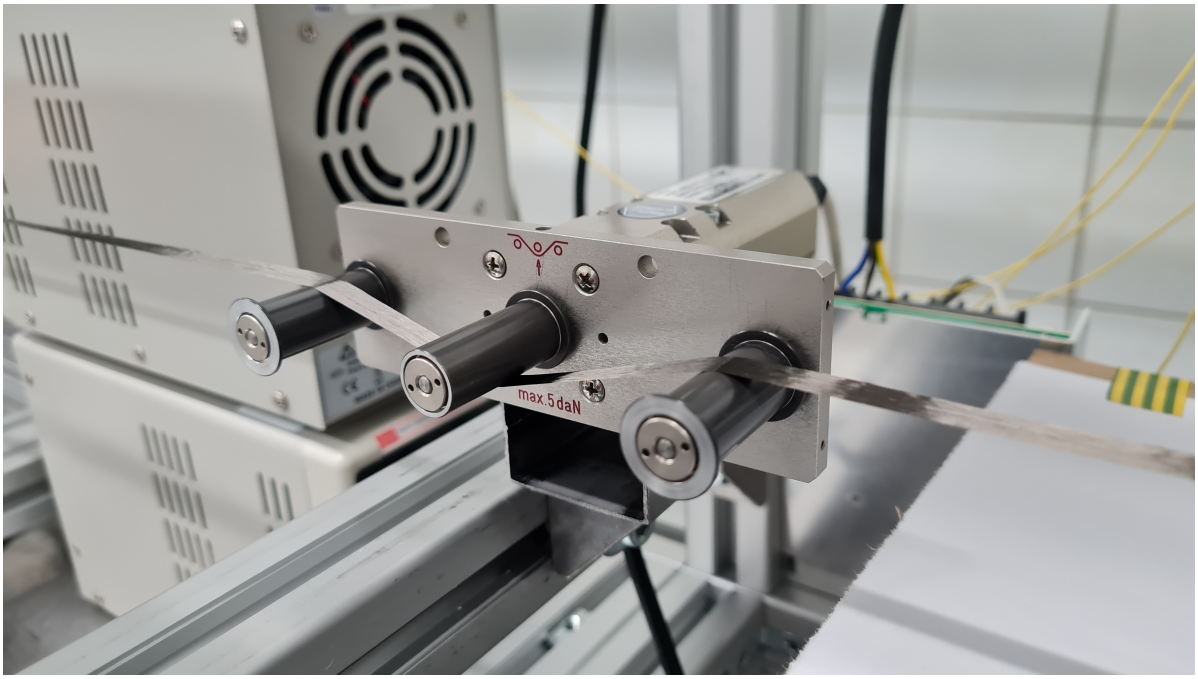


**Figure 2.7:** Image of installed tensionmeter.

A wiring diagram of the tensionmeter connections is displayed in figure 2.8. Relevant values have been noted in this figure.

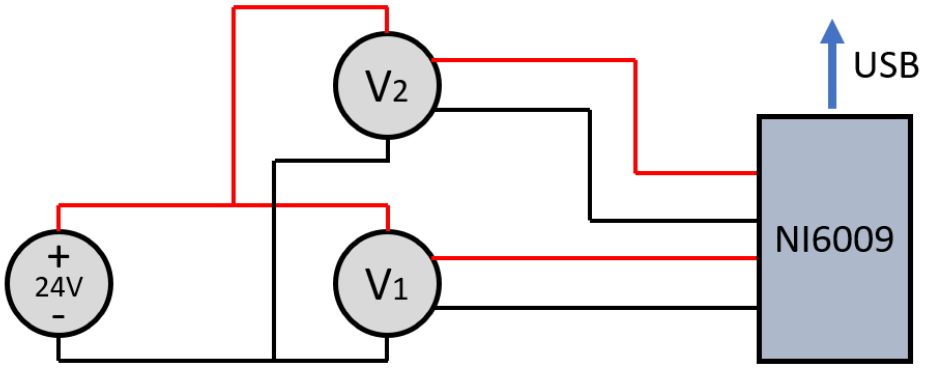


**Figure 2.8:** Wiring diagram for tensionmeters.

In an attempt to make an assessment on the state of the tow, a conductivity measurement is performed. The relation for determining resistivity in a material with a certain length $l$ and cross-sectional area $A$ is given in equation 2.1, also known as Pouillet's Law of resistance of a wire. As the state of the tow varies, its conductive properties change accordingly since the equation possesses the geometry dependant variables. Using this principle, a quantification can be obtained of a measured section of tow in terms of how well it conducts electricity. This is used to develop a baseline value for electrical conductivity of the tow. Then, offsets from baseline can be classified as tow sections with decreased electrical performance which is expected to be the result of damage, twists, or wavy behaviour. All of the above are namely expected to result in a either a reduced cross-sectional area or a reduced tow-to-bar interface area.

$$\rho = \frac{RA}{l} = \frac{UA}{Il} \tag{2.1}$$

For which $U$ is the present voltage and $I$ is the applied current to the circuit.

In this application, two of such conductivity sensors are installed. One before the spreading operation, and one after the spreading operation. This is decided such that a measurement can be performed on the change of resistivity (or conductivity, the inverse) during the spreading process. The two-sensor system therefore has the following functions.

1. Determine a baseline for conductivity within the system - such that deviating tow sections, such as damaged or twisted sections, can be noticed in the form of a electrical change.

2. Quantify the change in electrical properties during spreading by comparison of the two sensors - such that a possible correlation can be discovered.

A image showing an inline conductivity sensor is displayed in figure 2.9. The design utilizes four-point contact with the running tow in order to measure the conductive properties over a section of material with known current. The contact points are created by placing live copper tubes in contact with the tow under a small wrap angle. The tubes are connected to the subframe via 3D printed mounts. The current is introduced via the outer bars. Then, via the inner bars, a voltage can be measured of the section in-between these two inner bars. The current is supplied via a set of linear power supplies. For this research an introduced an introduced current of $500mA$ is used based on user experience. To potentially optimize this, a later study can be done to find the ideal applied current to use for a particular setup.

**Figure 2.9:** One of two conductivity sensors.

The copper tubes are physically attached to a subframe of the tow line built from the 40x40 mm aluminium extrusions. The mounting of the copper tubes to the extrusions is done via custom 3D printed brackets, which are also visible in figure 2.9. A wiring diagram of the resistivity sensor connections can be viewed in figure 2.10.

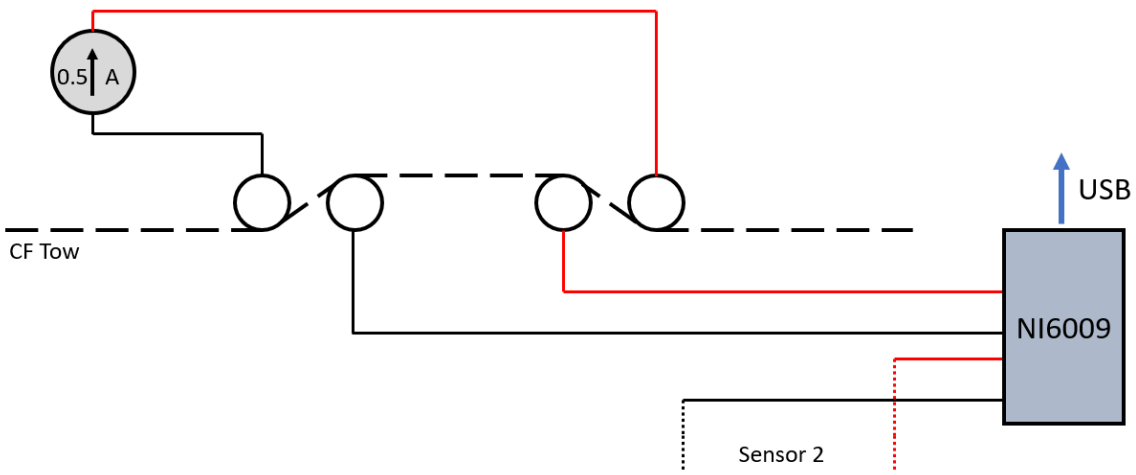


**Figure 2.10:** Wiring diagram for resistivity sensor(s).

A summarizing diagram, showing the machine functions and their respective locations in the line, is displayed in figure 2.11. Note that this diagram does not show attachment mounts or frame struts.

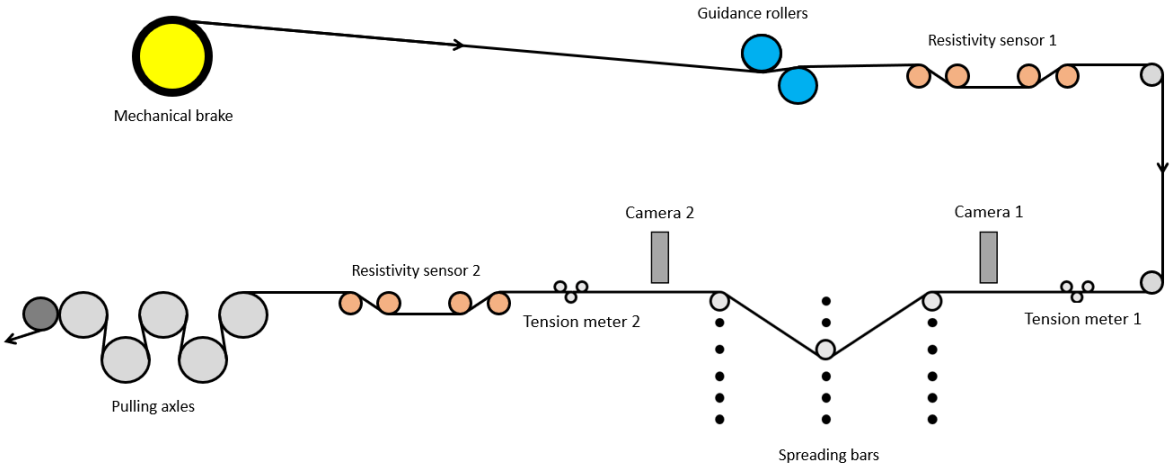


**Figure 2.11:** Diagram of spreading line functions.

## 2.2. Experimental Setup for Carbon Fiber Characterization

This section describes the experimental strategy of both the properties correlation investigation and the Capstan equation consistency investigation.

### 2.2.1. Research plan

To investigate the research questions posed in Chapter 1, a study is carried out to examine the correlations between various variables in the tow spreading process. The following variables will be considered: wrap angle, friction, conductivity, tow width, fibre straightness, pulling velocity, and pre-tension.

To create and measure these variables, a tow spreading line is designed and constructed, capable of accommodating the necessary equipment and operating within significant ranges, as previously described in section 2.1. The execution plan for conducting the experiments is explained in this section.

Experiments to investigate the correlations between the variables will be carried out using the newly-built tow spreading line. The experiments will be conducted under the same conditions, with the tow spreading line in motion. The machine functions, including wrap angle, pulling velocity, and pre-tension, will be adjusted within specific range intervals. The friction, tow width, conductivity, and fibre straightness will then be independently measured under various machine settings. The range indices for each input variable, or machine requirement, are provided below.

- Wrap angle (40, 80, 115, 150, 170 [degrees])
- Pre-tension (1-5 [pre-set settings])
- Pulling speed (4.4, 6.2, 7.7 [cm/s])

The obtained data will be analyzed before any conclusions can be drawn. Quantitative measurement values for friction, width, conductivity, and fibre straightness will be obtained using several sections of Python code, which are described in more detail in the following sections of this chapter.

An overview of the experimental procedure that will be conducted is provided below.

1. Adjust the pre-tension, pulling speed, and wrap angle of the tow spreading line to different values within a predetermined range interval.
2. Measure the resulting friction, tow width, conductivity, and fibre straightness for each setup.
3. Repeat the experiment several times to ensure accuracy and reliability.
4. Record and analyze the data to determine the relationships between pre-tension, pulling speed, and wrap angle and each of the four variables.

Please refer to Appendix B for a complete overview of the written and used code. The theory and application of the fibre straightness quantification are described in section 2.3.2.

### 2.2.2. Capstan equation investigation

Apart from the general correlation investigation presented in the previous section, special attention is given to a study towards the accuracy of the Capstan equation for this setup.

The capstan equation relates the force required to move a flexible cable or rope around a cylindrical object, such as a capstan or a winch, to the tension in the cable and the angle of wrap around the object. The equation is displayed in 2.2. Earlier, an alternative definition of the Capstan equation is also given in equation 1.6.

$$F = Te^{\mu\phi} \tag{2.2}$$

where $F$ is the force required to move the cable, $T$ is the standard tension in the cable, $\mu$ is the coefficient of friction between the cable and the object, and $\Phi$ is the angle of wrap around the object in radians.

The equation tells us that the force required to move the cable increases exponentially with the angle of wrap, so it becomes much harder to move the cable as the angle of wrap increases. This effect is often used in mechanical systems to increase the holding power of winches and capstans, because a small increase in the angle of wrap can greatly increase the tension that the system can hold. In the case of this research, the equation applies to a carbon tow moving over a spreader bar. In particular, the Capstan equation states a constant and material dependant friction coefficient. Since the validity of this is questioned within a tow spreading system, the investigation tracks the apparent friction coefficient as stated in equation 1.6. The pre-tension is to be varied, while wrap angles remains constant. The apparent friction coefficient should then remain constant as demonstrated in equation 2.3. Which is a different way of expressing the known Capstan equation at 2.2.

$$\mu_{app} = \frac{ln\frac{T2}{T1}}{\Sigma\Phi} \tag{2.3}$$

By measuring the tension before $T1$ and after the spreading process $T2$, of which the total sum of wrap angles is defined as $\Phi$, a conclusion on the consistency of $\mu_{app}$ can be found. If $T2$ changes proportionally with $T1$, keeping $\mu$ constant, the Capstan equation is considered valid for this type of setup. Additionally, the effects will be recorded during various line speed settings. The range intervals for the measured variables are according to section 2.2.1.

It is hypothesized that the friction coefficient $\mu$ does not remain constant. This hypothesis is based on previous research presented in chapter 1. Within this hypothesis it could be expected that the (apparent) friction coefficient increases in value with increasing system tension as is displayed in figure 1.10. However, since the setups are not identical, different behaviour might emerge.

## 2.3. Data Acquisition and Analysis

The examination of spreading of carbon fiber tow requires precise observation of various process parameters to ensure data of the quality and performance of the final product. One critical aspect of this is the ability to monitor and analyze real-time data from various sensors and instruments throughout the production line.

In this chapter, the data acquisition and analysis system used in the built carbon fiber tow spreading line is discussed. The system includes a National Instruments acquisition unit that collects data from multiple sensors interpreted by Python code, including tensionmeters and resistivity sensors. Additionally, cameras are used for optical analysis of the tow during production, and the resulting data is analyzed using custom software.

### 2.3.1. Data Acquisition

Acquiring data relates to the multiple sensors which are installed in the tow spreading machine. These are listed below. A National Instruments 6009 unit is used to capture the electrical measurement output. Cameras are used to obtain the optical data, and are connected via USB.

- Tensionmeters for friction measurements
- Copper 4-point resistivity sensors
- Cameras to perform optical analysis

#### Tensionmeters and Resistivity Sensors

The function and wiring of the tension and resistivity sensors is as shown in section 2.1.3 and figures 2.8 and 2.10. The tensionmeters function on the basis of mechanical strain, resulting in a variating voltage output which is correlated with a certain tow tension force to calibrate the outcome. The tension sensors provide output in a voltage interval of $0V$ to $10V$. The calibration of these sensors is considered trivial and is not further discussed. These voltage values are passed through to the mentioned NI unit. Similarly for the resistivity sensors, as the voltage over the two inner bars is measured, it is passed to the same NI unit. As the NI unit captures the voltage inputs, it sends the information via USB to a connected computer. Via a simple Python script, this data can be read. The Python script used to read the input data from the tension and conductivity sensors is shown in Appendix B. The Python scripts have the built-in ability to save the measured data in generated text-files, such that later analysis can also be done.

A set of preliminary static resistivity tests has been performed. The setup contained each resistivity sensor tested individually by inserting separate sections of 12K carbon fibre tow in them, tensioned by hanging dead weights. In these tests, each sensor is loaded with three separate random sections of 12K carbon tow by Toray, for a total of 6 sections. Each section is measured for voltage three separate times for a duration of five seconds. From this, an average resistivity value is retrieved per tow section

per sensor. The tension is provided by $1kg$ dead weights on either side. The results are presented in table 2.2 below.

| Sensor | Resistivity 1 [$m\Omega m$] | Resistivity 2 [$m\Omega m$] | Resistivity 3 [$m\Omega m$] |
|---|---|---|---|
| 1 | 20.74 +- 0.02% | 20.43 +- 0.05% | 20.73 +- 0.07% |
| 2 | 20.41 +- 0.04% | 20.20 +- 0.03% | 20.28 +- 0.08% |

**Table 2.2:** Resistivity measurement values per sensor

From this it can be seen that the resistivity sensor has a low error percentage. However, separate (intact) sections of tow have a larger variation in resistivity value compared to each other. An important note is that the connection interface, between tow and copper, is critical to the measurement. Variation is thought to be caused by natural differences in sections of tow and the slight variations in installing the sections into the sensors. To asses the interface contact in terms of resistive output, a test has been performed similar to shown above but with only one sample and with increasing dead weights ranging from 1 to 3 KG. The results are shown below in table 2.3. Sensor 1 is used to obtain these results. As the tension is increased, the contact between tow and sensors increases as well, decreasing resistivity of the connection.

An image of the data presentation via Python is displayed in figure 2.12. Note that this data does not correspond with the above-given values.

| Dead weight [$kg$] | Avg. Resistivity [$m\Omega m$] |
|---|---|
| 1 | 20.55 |
| 2 | 20.47 |
| 3 | 20.43 |

**Table 2.3:** Resistivity measurement values per dead weight, using sensor 1.

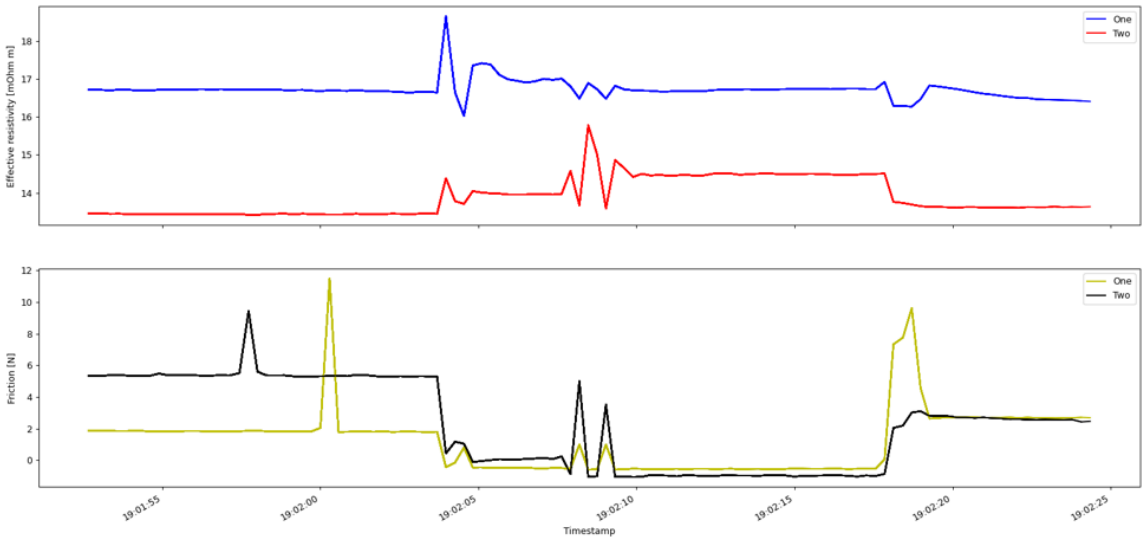


**Figure 2.12:** Resistivity and Tension data interface. 1=before spreading, 2=after spreading.

### Cameras for optical analysis

The cameras used, for retrieving optical information of sections of tow, have a zoom factor of 60x. These micro-scope cameras are connected via USB to the operating computer, from which they also receive their operating power. The cameras have a resolution of 640 by 480 pixels, and are placed at a

distance of 20 mm from the tow (sensor to object). Underneath the tow, opposite of where the camera is located, single-color white cardboard is placed to enhance the contrast for an increased detection of the carbon properties.

These cameras are the main sensors for the topics of width detection and straightness detection. By using custom Python software, the digital image is analyzed for this information. An explanation on how this analysis code functions, is given in section 2.3.2. For the case of the cameras, one is placed before the spreading system and one is placed after. Following the same logic as for the resistivity and tension sensors.

### 2.3.2. Data Analysis

#### Resistivity and Friction data

As explained in the previous section, resistivity and tension are measured with two sensors each, after which results are stored in newly generated text files. From these text files, data can be read. Then a comparison commences between the first and second sensors, such that the change in parameters, occurring during the spreading process, can be quantified. Other notable observations are saved also. The resulting data is presented as is shown in chapter 3.

#### Width detection

For width and gap detection purposes, a custom Python code has been made. Below, an explanation of the implementation is given.

The code starts by importing the necessary libraries, including *OpenCV* for computer vision operations, *NumPy* for numerical operations, and *datetime* for handling timestamps. It then initializes a video capture object using the connected camera via a simple while-loop. Inside this loop, the code reads a frame from the video stream and applies a series of image processing operations to create a binary image with morphological smoothing, which is used to find the contour with the largest area. The code then draws the largest contour on the original image and finds the bounding rectangle of the contour to obtain the height of the object, which, in this case, is the width of the passing tow. The highest value is reported, such that if the tow appears as parallelogram, the largest width is chosen.

The code then converts the image to grayscale, applies a threshold to create a binary image, and calculates the horizontal projection of the image. It then finds horizontal gaps in the projection by looking for values below a certain threshold, and draws the gaps onto the image with transparency. The code displays the resulting image in real-time with the object height and gaps marked, and writes the current timestamp and height value to a new output file. The code can be exited by a simple keyboard command. The complete code can be read in Appendix B. An example of the inline real-time view is shown in figure 2.13, where pre-spreading and post-spreading width are measured simultaneously via two cameras. Note that the height/width is expressed in pixels.

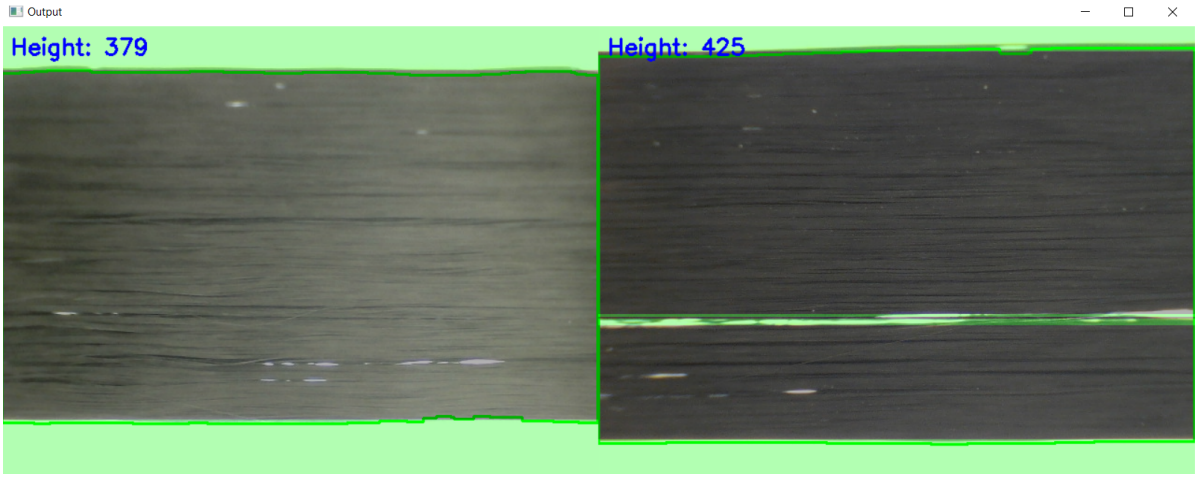


**Figure 2.13:** Width detection interface: camera 1 (left) and camera 2 (right). A gap is marked and highlighted in the right image. A green contour is generated around the tow. Transparent green blocks are placed where there is no tow, above and below of the tow and over gaps.

In figure 2.14, the contour- and height finding capabilities of the code are displayed using various objects. In here it can clearly be seen that the code recognizes the main contour of the objects pretty well, indicating them with the bright green fit. It marks brighter sections as gaps, highlighted with transparent green.

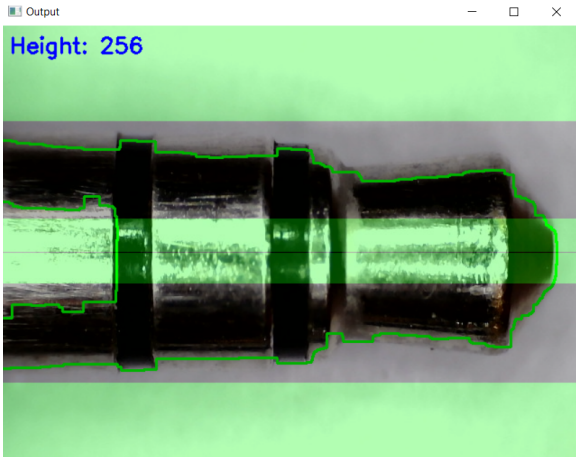


**(a)** Picture of 3.5mm headphone jack. Bright reflection in the center-line is recognized as gap.

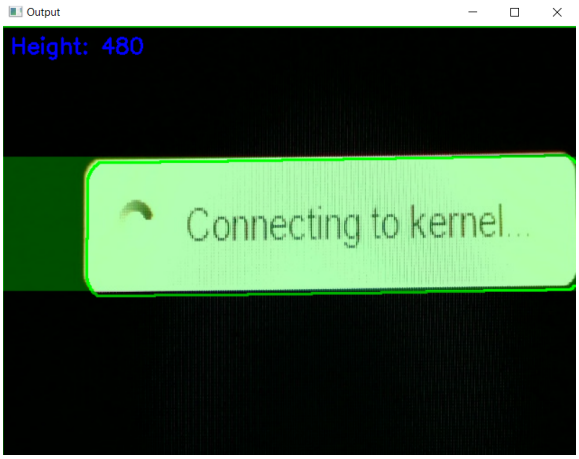


**(b)** Picture of Python kernel crash. The background is seen as tow, excluding the white section in the fit and highlighting it as a gap.

**Figure 2.14:** Test cases of contour-finding code.

### Directional analysis

For directional detection purposes, two main options are considered. The first of these options is chosen as data analysis method for this particular setup, and is explained first below. The second method is discussed hereafter. For both of the methods, a custom Python code has been made. Below, an explanation of the implementation is given.

The first method that is explained is the method used for the final line. The code uses *OpenCV* library to detect lines in real-time from a camera feed and computes the average angle and standard deviation of these lines. The code starts by importing the necessary libraries: *cv2*, *NumPy*, and *datetime*.

The script initializes the camera and enters into a loop for capturing. The loop applies image processing techniques to detect the edges of the lines using the Canny edge detection algorithm. The Canny

algorithm firstly applies Gaussian blurring to the image to reduce noise and make the edges more distinct. This is done by convolving the image with a Gaussian kernel. This type of linear filter is commonly used to blur or smooth images. It has the property of being able to remove high-frequency noise while preserving the edges in the image. Next, the algorithm calculates the gradient of the smoothed image. This is done by convolving the smoothed image with two derivative masks, via Sobel filters, to obtain the gradients in the x and y directions. The Sobel filter is a linear filter that approximates the gradient by convolving the image with two $3 \times 3$ kernels: one for the x direction and one for the y direction. The Sobel operator for the x direction is defined as:

$$\begin{bmatrix} -1 & 0 & 1 \\ -2 & 0 & 2 \\ -1 & 0 & 1 \end{bmatrix}$$

And for the y direction:

$$\begin{bmatrix} 1 & 2 & 1 \\ 0 & 0 & 0 \\ -1 & -2 & -1 \end{bmatrix}$$

To, for example, calculate the gradient in the x direction at a particular pixel $(i, j)$, we would multiply the pixel values in the image by the corresponding values in the Sobel x kernel according to equation 2.4.

$$G_x(i,j) = (I(i{-}1, j+1) + 2I(i, j+1) + I(i+1, j+1)){-}(I(i{-}1, j{-}1) + 2I(i, j{-}1) + I(i+1, j{-}1)) \quad (2.4)$$

The gradient of an image is a vector that points in the direction of the steepest increase in intensity. In the case of edge detection, we are interested in the magnitude of the gradient, which gives an indication of the strength of the edge. The script then finds contours of these edges. For each contour, the script fits a line using the least-squares method and calculates the angle of this line with respect to the horizontal axis. The angles of all lines are collected in a list, and the script computes the average angle and standard deviation of these angles. The script also draws the lines on the image and displays the average angle and standard deviation on the frame in real-time. The script writes the data to a text file named after the current timestamp. The data includes the timestamp, average angle of all visible lines per frame, and standard deviation of the detected lines. This way, a deviation from the average angle will be visible due to an increased standard deviation on the set of all detected lines per frame. The code is stopped via keyboard interruption.

The function of the code is demonstrated in figure 2.15, where the angle of any object (in this case scrap metal) is determined in real-time. Note that this range is for illustrative purposes. The code has also been successfully tested to distinguish between single degrees. The Std. Dev. offset values are demonstrated in figure 2.16, where it can be seen that a higher variety of line angles (simulating waviness and fiber offsets within a carbon tow) naturally results in a significant change in standard deviation. Fitted lines are plotted in purple. An example of the inline live-feed is given in figure 2.17, where pre-spreading and post-spreading conditions are analyzed simultaneously in real-time. Note that the sensitivity and line thickness have been turned down on purpose to show the underlying tow more clearly.


**(a)** Picture of random piece of metal at 0 degrees.


**(b)** Picture of random piece of metal at 45 degrees.

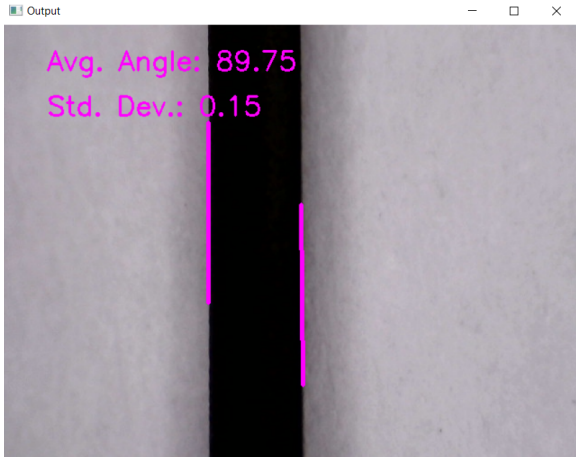


**(c)** Picture of random piece of metal at 90 degrees.

**Figure 2.15:** Directional Detection code demonstration.


**(a)** Picture of random piece of metal at 0 degrees.


**(b)** Picture of random piece of metal at 0 degrees with additional object at 40 degrees.

**Figure 2.16:** Anomaly Detection via offset in Std. Dev.

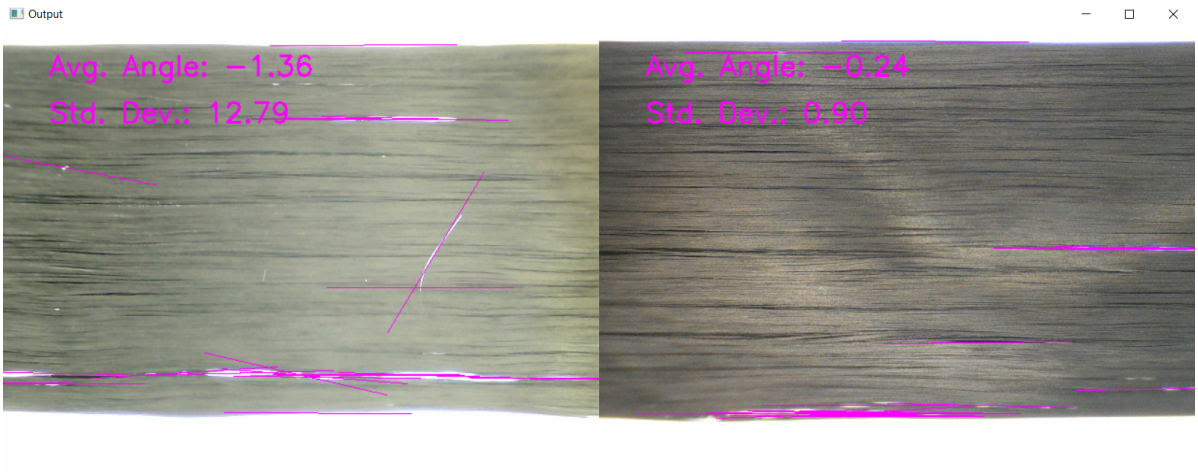


**Figure 2.17:** Directional detection interface: camera 1 (left) and camera 2 (right). Note that sensitivity has been turned down for this image.

The second method that has been applied and tested, but not implemented, makes use of structure-tensor analysis to determine lines in the retrieved image. This is done by first taking the gradient over the x and y directions. Looking parallel to the length of a fibre, not much intensity difference will occur. However, looking perpendicular to the fibre directions, the intensity will vary significantly. This results in variating gradients per direction. Generally, the directional derivative (in x direction) can be determined according via equation 2.5 below - known as the central finite difference approximation of derivatives.

$$G_x(i) = \frac{G_x(i+1) - G_x(i-1)}{2} \tag{2.5}$$

Now that the directional derivatives are found, the tensor matrix can be built. The tensor matrix looks as in equation 2.6.

$$S(x, y, z) = \int_{W_s(r)} S'(r)dr \tag{2.6}$$

For which:

$$S'(r) = \begin{bmatrix} G_x \times G_x & G_x \times G_y & G_x \times G_z \\ G_y \times G_x & G_y \times G_y & G_y \times G_z \\ G_z \times G_x & G_z \times G_y & G_z \times G_z \end{bmatrix} \tag{2.7}$$

Once this matrix is built, a statement about the main directions of the matrix can be made based on its eigenvalues.

Even though the latter method provides interesting results, it currently lacks accuracy for this particular case due to the nature of homogenizing images via this method. Setting different kernel sizes, for now, only changes the sections which are not represented in detail. Also, computation is significantly more intensive compared to the previously mentioned technique. This is a major disadvantage when using Python, since a live-feed of the analysis was troublesome to produce considering the small tow section displayed and the relatively fast movement hereof. An example of the functionality of this code, during the detection of twists in the tow, can be seen in figure 2.18. One can see that the twisted section of tow, from top-left to bottom-right in figure 2.18a, is detected to indeed have a different orientation as seen in figure 2.18b.

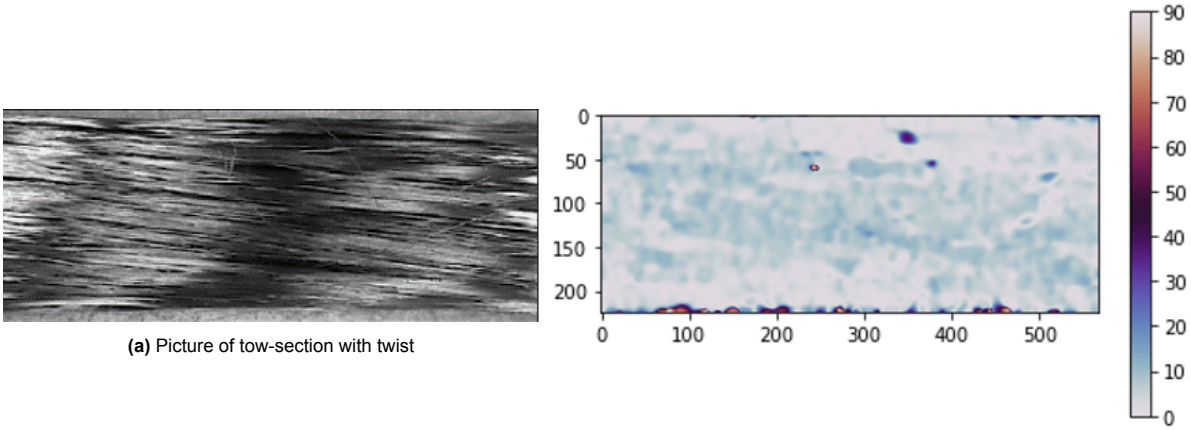


**(a)** Picture of tow-section with twist

**(b)** Tow-section after analysis

**Figure 2.18:** Twist detection via Structure-Tensor approach.

# 3

# Results and Discussion

In this chapter, the main results are displayed. The chapter presents and discusses data related to friction behaviour, carbon fiber resistivity, optical analysis, and anomaly detection.

## 3.1. Friction Behaviour

The friction behaviour of the spreading system is analyzed according to the research plan described in chapter 2.2.1; pre-tension, pulling velocity, and wrap angle are varied, while tension in the tow is measured before and after the spreading process. A diagram of the experimental method can be seen in figure 3.1. This was done for two machine setups, one *with* resistivity sensors installed, and one *without* resistivity sensors installed. Although resistive properties are not measured at this point in time, a comparison was made to show the influence of the presence of the resistivity sensors on the friction behaviour of the line. Note that the presented data points are average values over measurement intervals of 5 seconds, at a sampling rate of 30 Hz.

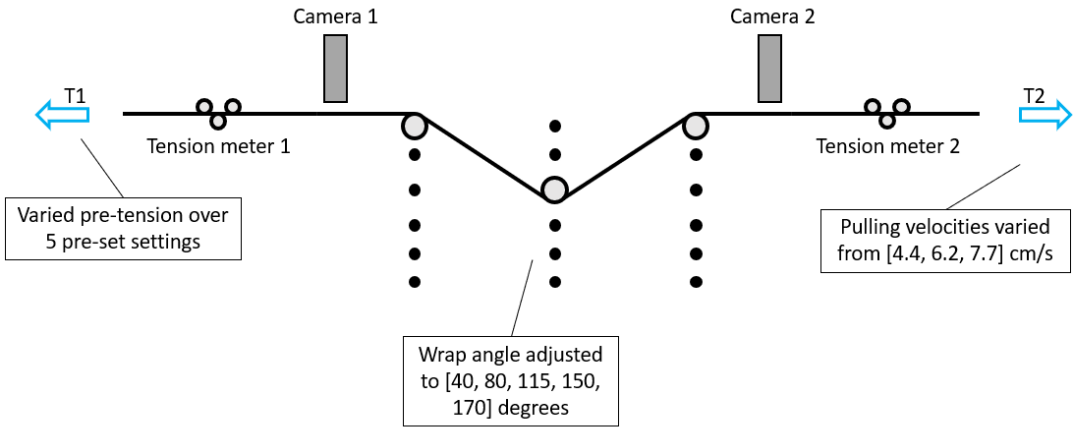


**Figure 3.1:** Diagram of experimental method. Note that the cameras are not yet used for this section's results.

Referring to equation 1.6, it is stated that the tension ratio is a function of the friction coefficient $\mu$ and the wrap angle $\phi$. Therefore, if Capstan holds true for this case, the tension ratio should be a constant value if friction coefficient and wrap angle remain constant. For general cases, it is commonly assumed that these remain constant since $\mu$ is a material property and $\phi$ is related to setup installation. For this current setup, wrap angle is constant per run. Therefore, if the tension ratio $\frac{T2}{T1}$ appears non-constant, it can be said that the apparent friction coefficient is variable instead of a fixed parameter.

Figures 3.2 and 3.3 show the friction relations for the case without and with resistivity sensors respectively. Although the data is collected according to 3 variables, see figure 3.1, the figures below are grouped only per wrap angle. This is done to show the behaviour of the tension ratio per wrap angle, since, according to equation 1.6, other variables would not influence the trend.

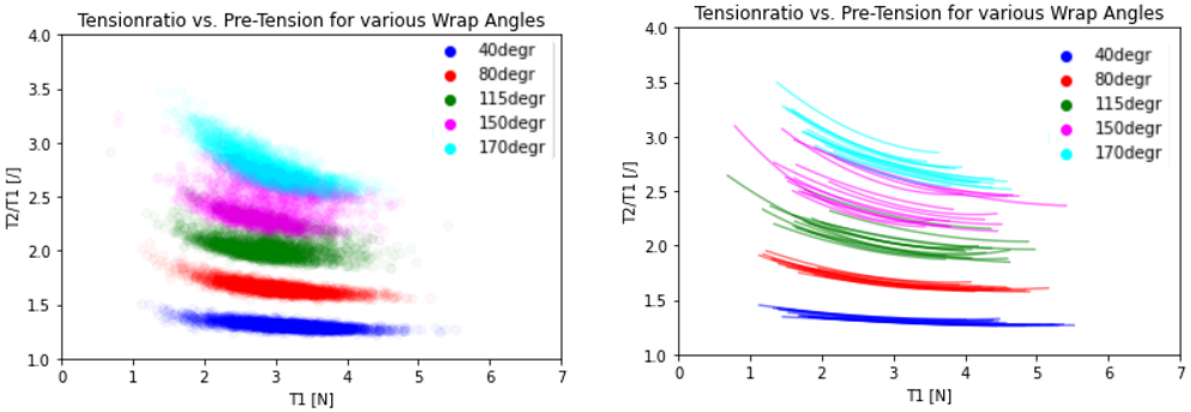


**(a)** Tension ratio T2/T1 vs. pre-tension T1.

**(b)** 2nd order polynomial fits of tension ratio T2/T1 vs. pre-tension T1.

**Figure 3.2:** Tension ratio vs. pre-tension for case without resistivity sensors installed.

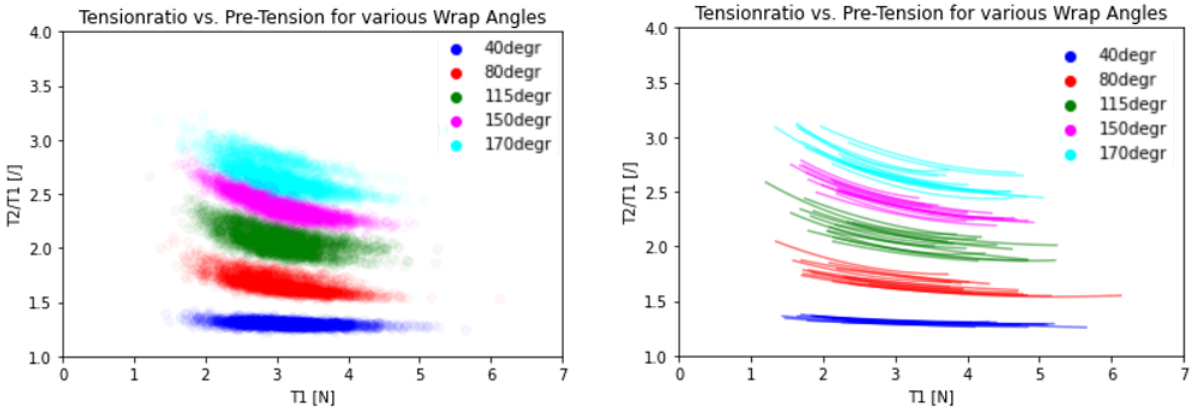


**(a)** Tension ratio T2/T1 vs. pre-tension T1.

**(b)** 2nd order polynomial fits of tension ratio T2/T1 vs. pre-tension T1.

**Figure 3.3:** Tension ratio vs. pre-tension for case with resistivity sensors installed.

From these figures, a downward trend can be observed in all measurement results. Fitting parameters are displayed in Appendix C for the 2nd order polynomial fits. This contradicts the Capstan assumption that the apparent friction coefficient $\mu$ is constant per wrap angle. A notable property of the trends, however, is that they seem to approach an asymptotic value as pre-tension is increased. Further research should be performed to confirm this observation. What can also be noted is that the trends, from the setups with and without resistivity sensor, have roughly the same progressions. A difference is that the setup with resistivity sensors acts over a slightly higher pre-tension $T1$ range. This makes sense, since the addition of resistivity sensors in the line adds extra friction events in the line, increasing the tension read at the first tensionmeter. This addition seems to shift the data further down the trend by about $0.5N$ on the x-axis, and by about $-0.5$ on the y-axis. Parameter readouts of the fitted curves can be read in Appendix C.

As earlier mentioned, multiple variables were measured during the experiments. One of these is how the pre-tension influences the measurement results directly. In theory, based on the results from figures 3.2 and 3.3, a higher pre-tension should shift the data further down the trend. Figures 3.4 and 3.5 show subplots per wrap angle setting, where differences resulting from pre-tension are highlighted

with different colors. Each subplot corresponds to an individual color from figures 3.2 and 3.3.

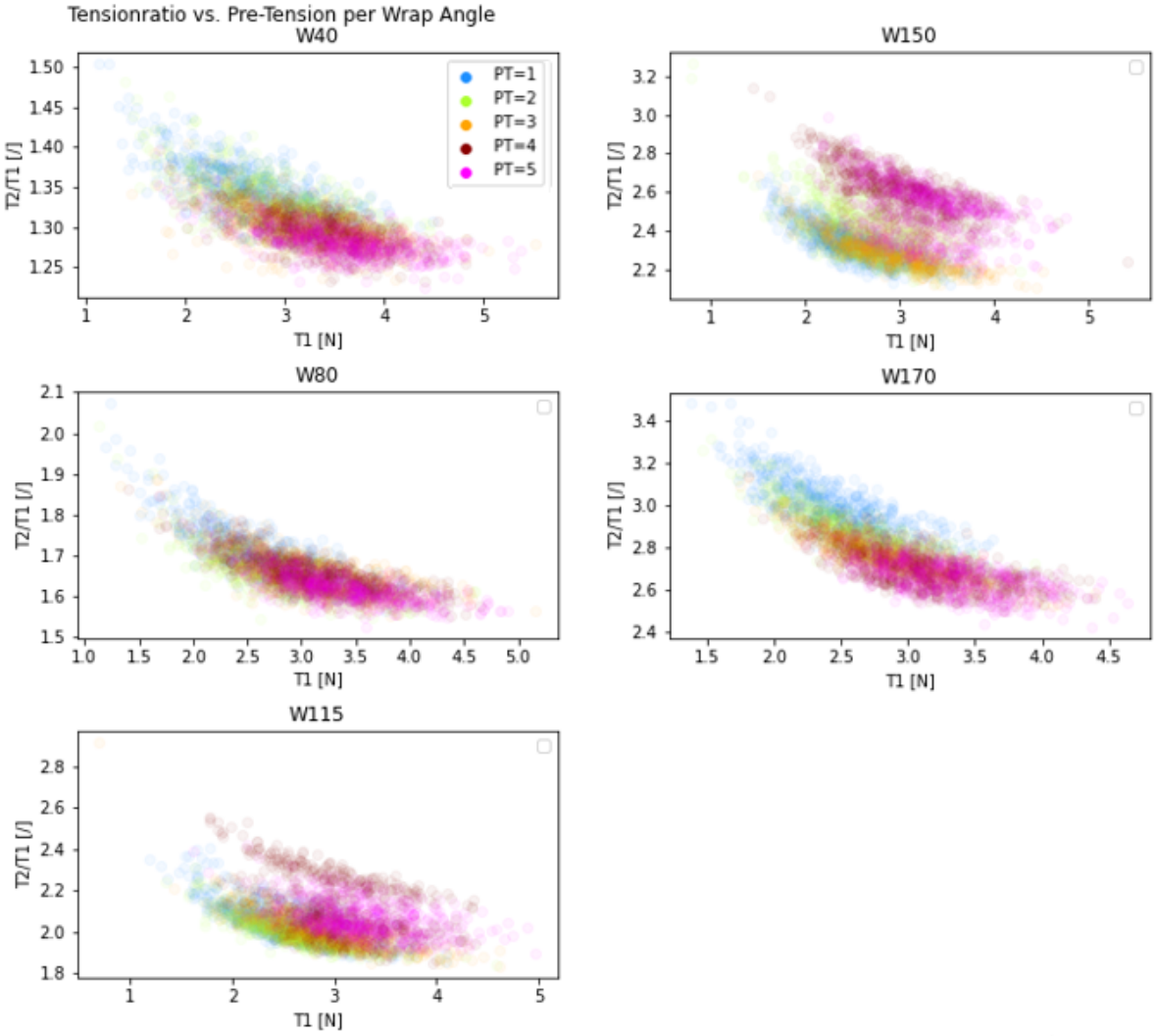


**Figure 3.4:** Tension ratio vs. pre-tension per wrap angle for various pre-tension settings. Subtitles show wrap angle values (e.g. W40 = wrap angle of 40 degrees). No resistivity sensors installed.

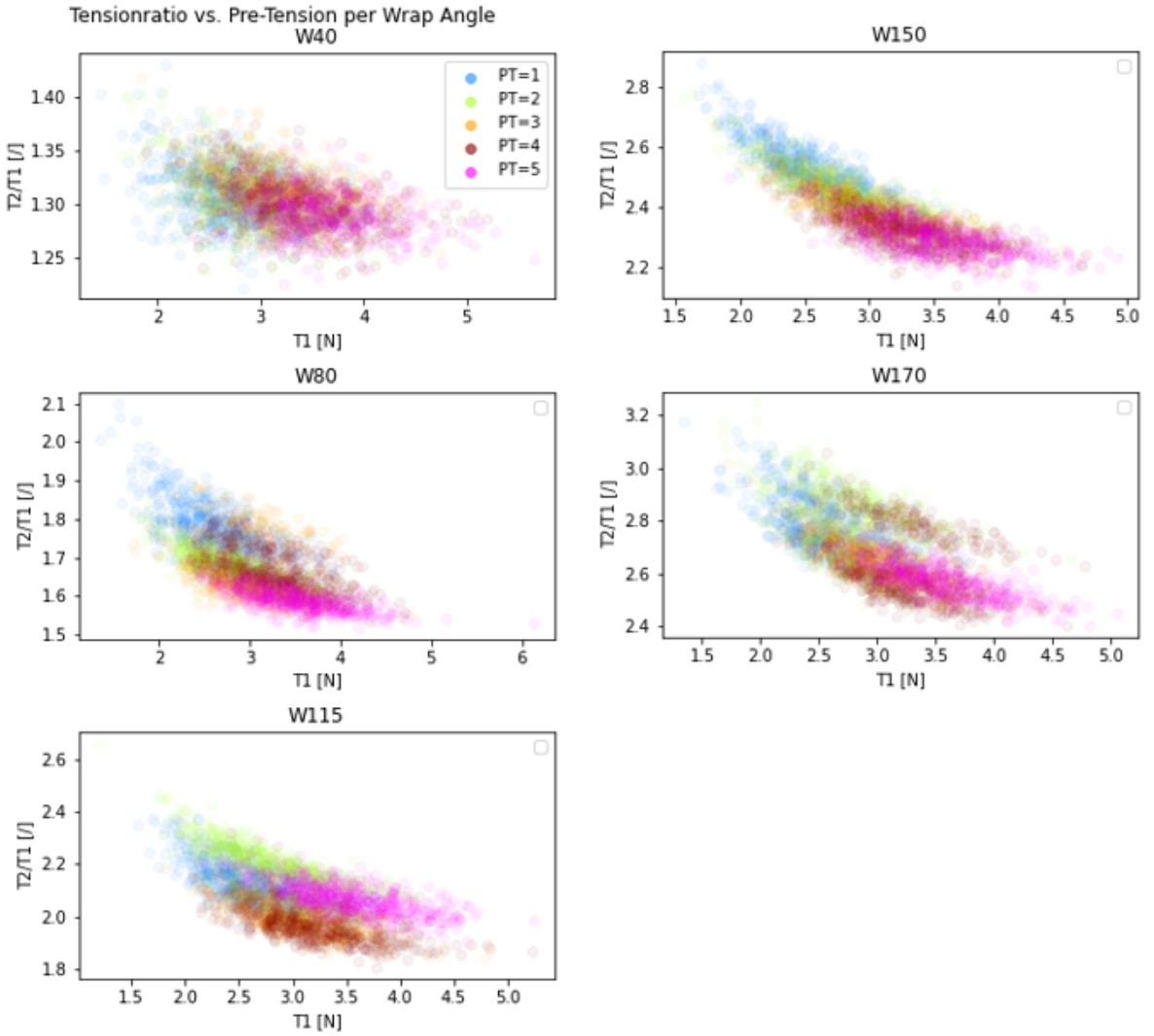


**Figure 3.5:** Tension ratio vs. pre-tension per wrap angle for various pre-tension settings. Subtitles show wrap angle values (e.g. W40 = wrap angle of 40 degrees). Resistivity sensors installed.

Generally, the same trend holds locally as it does globally: as $T1$ is increased, the tension ratio $T2/T1$ decreases. This can clearly be recognized in most of the plots shown. Although some figures do show a deviation here from, such as the 150 degree wrap angle case of figure 3.2 and the 115 degree wrap angle case of figure 3.3. These deviations from the trend are suspected to be due to process instability, which could be potentially solved by making small changes to the production line as discussed in Chapter 4.

Lastly, a distinction was made based on the pulling speed. For this, wrap angles and pre-tension settings can be displayed once at a time. Otherwise, due to the nature of the data, overlaps distort the results. Figure 3.6 shows the tension ratio vs pre-tension for the pre-tension brake setting of 4 out of 5, for the total range of wrap angles. The complete overview of results can be viewed in Appendix C.

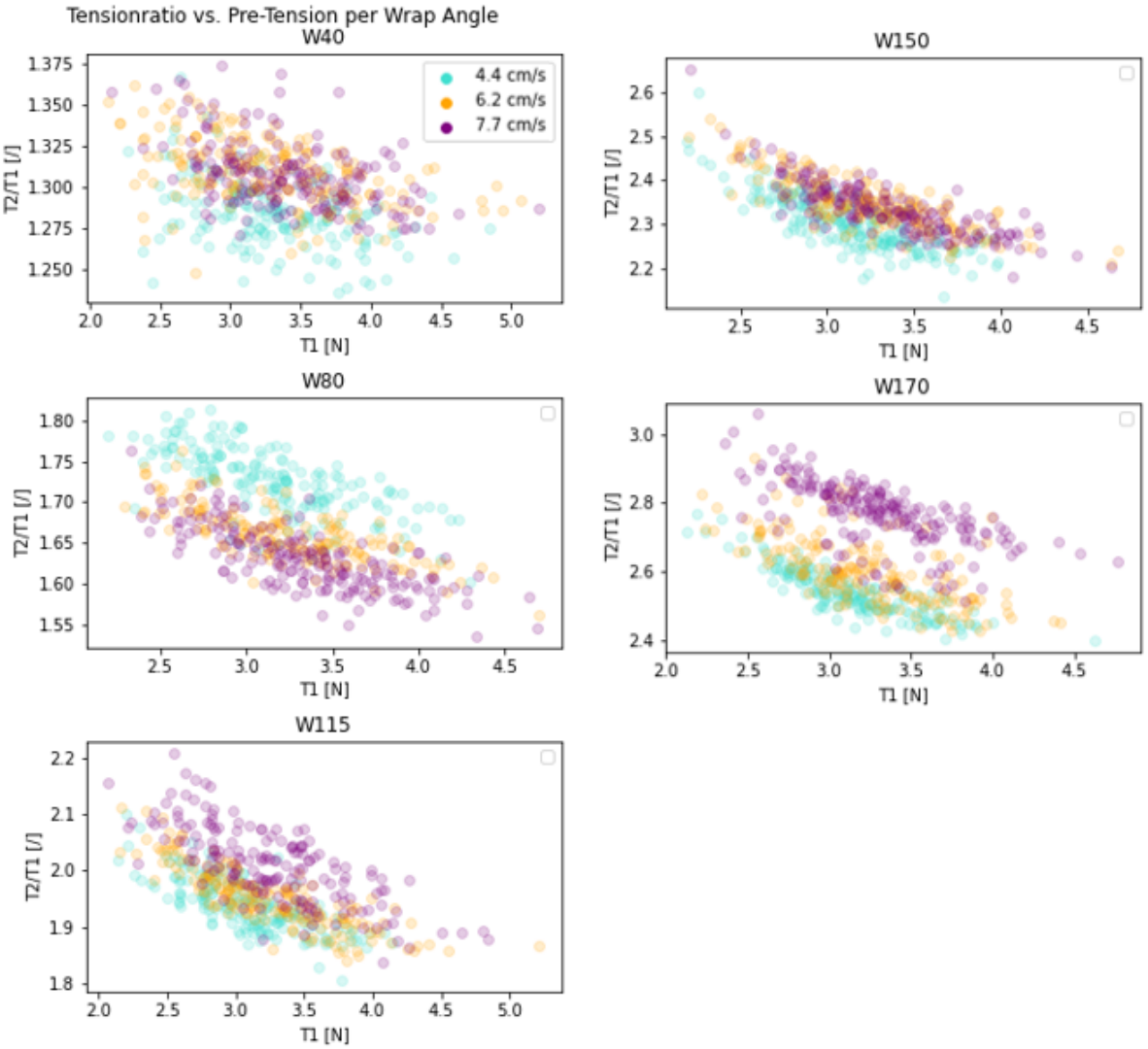


**Figure 3.6:** Tension ratio vs. pre-tension per wrap angle for various wrap angles at a pre-tension setting of 4/5. Case with installed resistivity sensors. Subtitle shows wrap-angle.

Generally, tow sections which move with a higher relative velocity respective to the spreader bar experience a measurably higher tension ratio $T2/T1$ for the same pre-tension $T1$. This can potentially be explained with the principle of energy minimization [24]. As the tow passes over the spreader bar and endures mechanical interlocking, a small strain is induced on the fibers in the tow. It takes a certain amount of time for stored energy to minimize before the next strain operation starts. If the velocity of the tow, relative to the bar, is increased, the fibers have less time to minimize their internal strain energy before the next strain event occurs. Due to this reduction in minimization in energy, a higher friction scenario naturally takes place.

That being said, outliers occur. To make a better defined statement about the influence of relative velocity and the friction behaviour, additional studies should be performed with an extended range of tested relative velocities.

## 3.2. Effect of Tow Spreading on Carbon Fiber Resistivity

In this section, results will be provided on the resistivity based measurements of UD carbon fiber. General parameter based values are displayed and discussed first, after which anomaly detection results are shown.

### 3.2.1. Electrical Resistivity of UD Carbon Fiber

In an attempt to assess the relation between material resistivity and processing parameters, experiments are done in which both the tension and resistivity of the material are measured for various line settings. Further in this section, real-time resistivity measurement results are presented from figure 3.10 where notable observations are mentioned.

The data points as seen in figure 3.7 are average values each, taken as the mean value from 5 second measurements. In these figures, measured average resistivity values are plotted against $T2 - T1$, or the friction that occurs in between both sensors (during spreading). The process of obtaining the data follows a similar approach as described in section 3.1, where the wrap angle, pulling speed, and pre-tension are modified within a specific range. The collected data is then organized into subgroups based on the wrap angle, allowing the main trend to be more clearly discernible. However, it is important to note that the distinct clusters visible, each represented by a consistent color, actually comprise data collected from different machine settings. Other data representations can be viewed in Appendix C, where differences in pulling speed and pre-tension are highlighted.

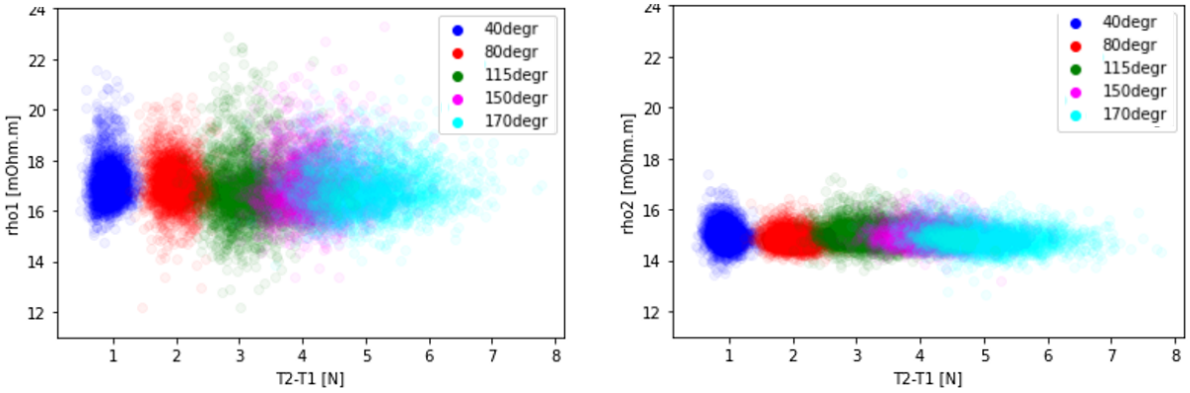


**(a)** Rho 1 vs. T2-T1

**(b)** Rho 2 vs. T2-T1

**Figure 3.7:** Resistivity before (left) vs. after (right) spreading vs. induced spreading friction.

From figure 3.7 it can be seen that the resistive material value decreases as the tow passes through the spreading system. Since tension increases as the spreading process occurs (increasing real contact area), and according to table 2.3, the resistive properties should indeed reduce. Increasing the wrap angle in the setup implies the same physical effect of increased friction, which is recognized as a very slight downward trend in figures 3.7a and 3.7b. What also stands out, is the fact that the deviation in figure 3.7b is not as large as for figure 3.7a. This is believed to be due to the fact that the second resistivity sensor is installed further down the line and is influenced less by the periodical noise of the mechanical brake, resulting in a more consistent measurement. More on this can be read in chapter 4.

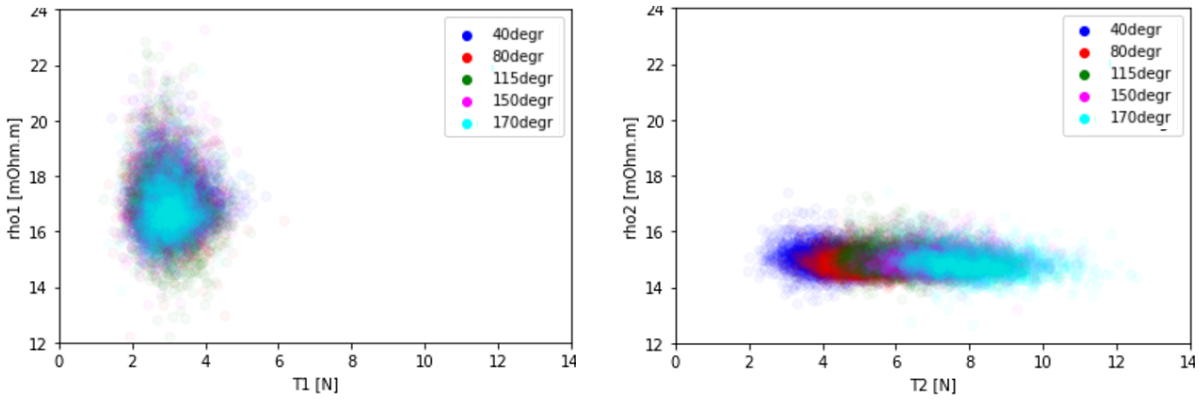


**(a)** Rho 1 vs. T1

**(b)** Rho 2 vs. T2

**Figure 3.8:** Resistivity before (left) vs. after (right) spreading vs. local tow tension.

As is visible from figure 3.8, the material resistive properties are consistent to a certain degree. What should be mentioned is the fact that data points are clustered for the case before spreading, and more linearly spread-out after spreading. This is, of course, because the wrap angle value has no influence on the tension value in figure 3.8a as oppose to the tension value in figure 3.8b.

### 3.2.2. Anomaly Detection via Resistivity Deviation

Some instances are better to be retrieved via the live data. An experiment is done to check the stability of the apparent trends by observing live output. Since a recognizable baseline is present for both pre- and post-spread resistivity, attempts can be made to deviate from this baseline by obtaining outliers.

Manually applying damage during the spreading operation could result in a offset from the trend. Of course, spreading itself also causes damage to the tow which reduces the tow-to-bar contact area, increasing resistivity. However, this effect is oppositely correlated with tension which increases the contact force and reduces effective resistivity. Manually adding extra damage during the measurement series could indicate what trend should be present and what offsets can be expected under certain circumstances. In figures 3.10 and 3.12, live sensor responses are observed for (applied) tow damage and observed (factory) tow waviness respectively. Figure 3.9 shows an example of applied cut damage to a section of tow.

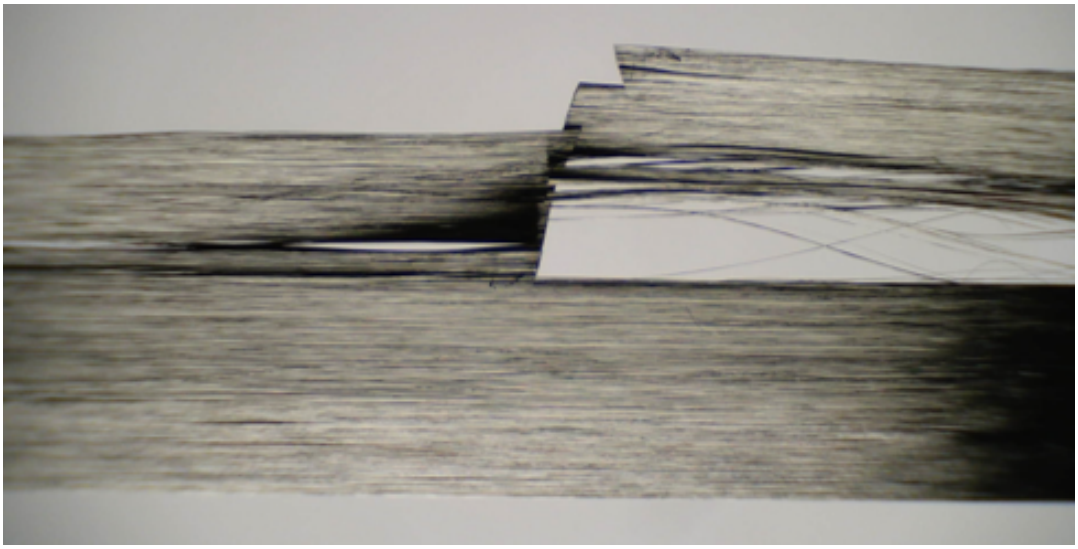

**Figure 3.9:** Image of applied cut damage to 12K carbon tow.

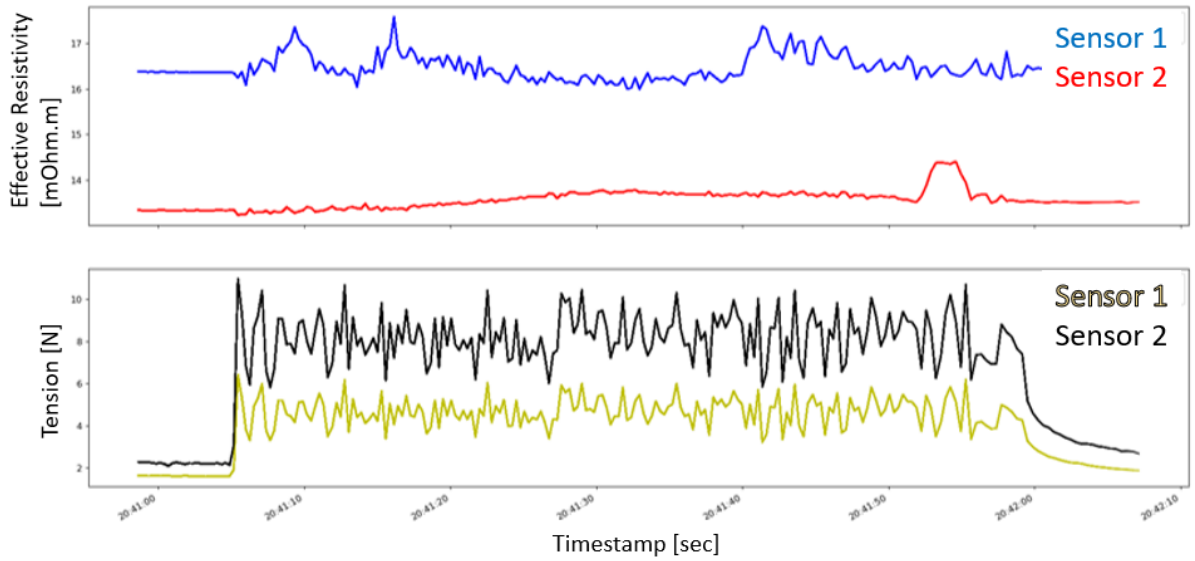


**(a)** Cut Example Case 1.

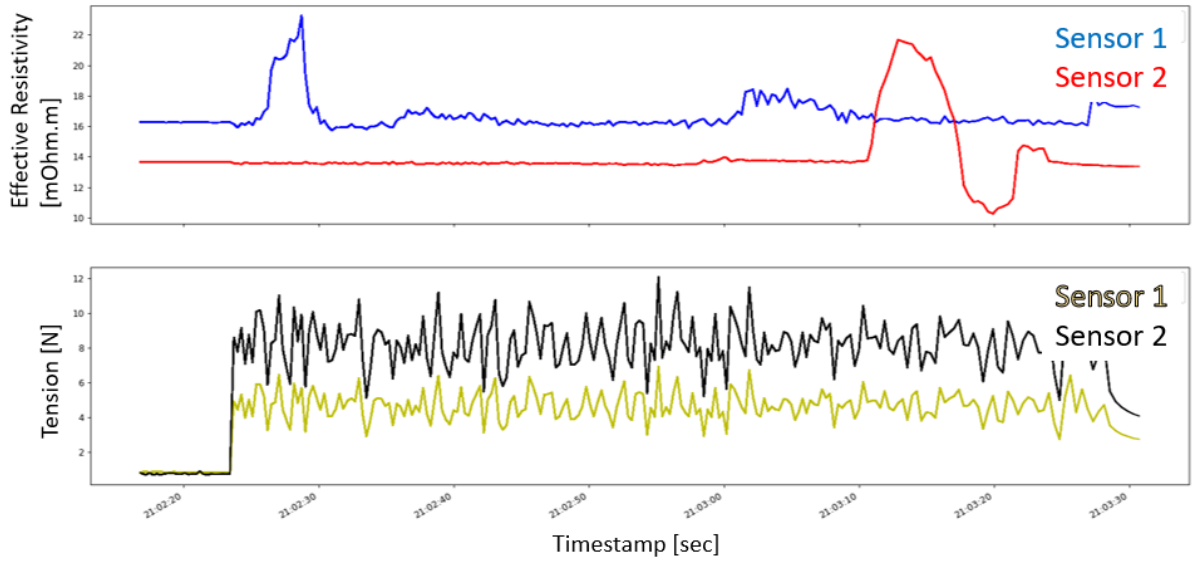


**(b)** Cut Example Case 2.

**Figure 3.10:** Live view of Tension (Yellow/Black) and Resistivity (Blue/Red) sensors. Response check via inflicted damage to tow. Blue and red regions indicate resistivity before and after spreading respectively. The x-axis shows the timestamp during the live operation. Inflicted damage to tow section is detected by the first peak in the blue region, and again by the peak in the red region. Anomaly travel time, from sensor 1 to sensor 2, is represented by the time in between the major blue and red peaks.

The inflicted damage includes a small lateral cut (1-2mm) in the tow cross-section. In figure 3.10a, this cut is seen to not significantly be detected by the first sensor. This is due to the wavy nature of the fresh carbon tow (further mentioned below), which can return similar resistivity responses as is seen in the figure. However, even though the initial response is not as clear, sensor 2 has no difficulties picking up the anomaly. This is since the tow, arriving at the second sensor, is more straightened and tensioned resulting in a more consistent signal, evident from the smoother response plotted in red in figures 3.10a and 3.10b. Such anomalies then stand out significantly. Figure 3.10b shows a similar scenario, but with a larger cut (more towards 2mm). Here the initial signal is already noteworthy. The signal of sensor 2 then becomes more pronounced. Upon visual inspection, the reason hereof can be said to be damage growth due to the friction events in the spreading process. Additional friction pulls the filaments apart even further, exaggerating the effect.

It is hypothesized that, when a section of the tow is cut, the load is locally carried by a subset of

the overall bundle. Then, when the tow comes in contact with the resistivity sensors, the subset of tensioned (and touching) fibres is smaller compared to a non-damaged tow. This locally increases resistivity by decreasing the effective current cross-section, as stated by equation 2.1.

A similar effect should then occur when waviness is present in tow sections. In the case of a wavy bundle section, also only a subset of the fibres is carrying tension. An example of this is shown in figure 3.11. According to the logical derivation above, the tow should return a signal which peaks when waviness occurs. Figure 3.12 shows the output signal for two measurements where naturally occurring tow waviness is measured.

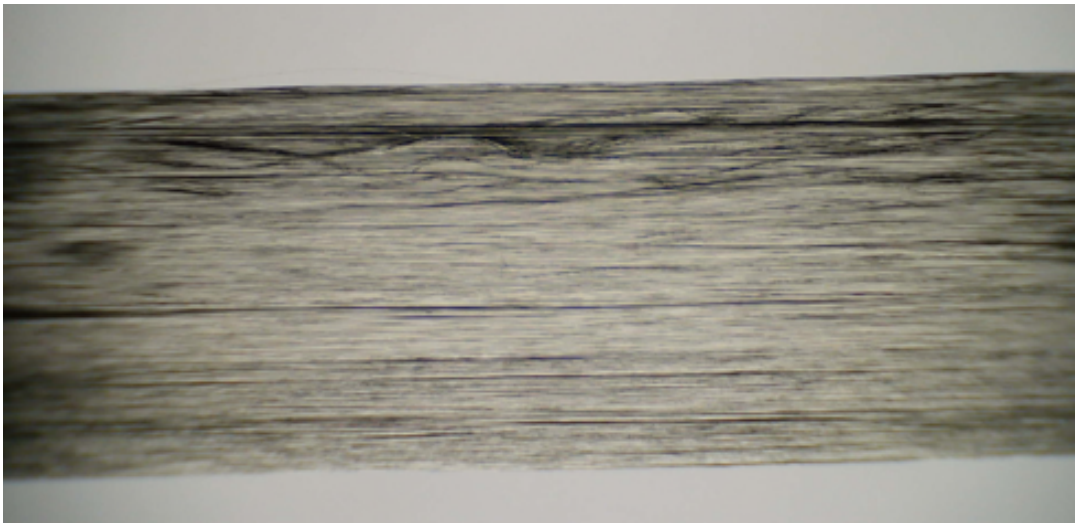

**Figure 3.11:** Image of factory (as-received) waviness of 12K carbon tow.

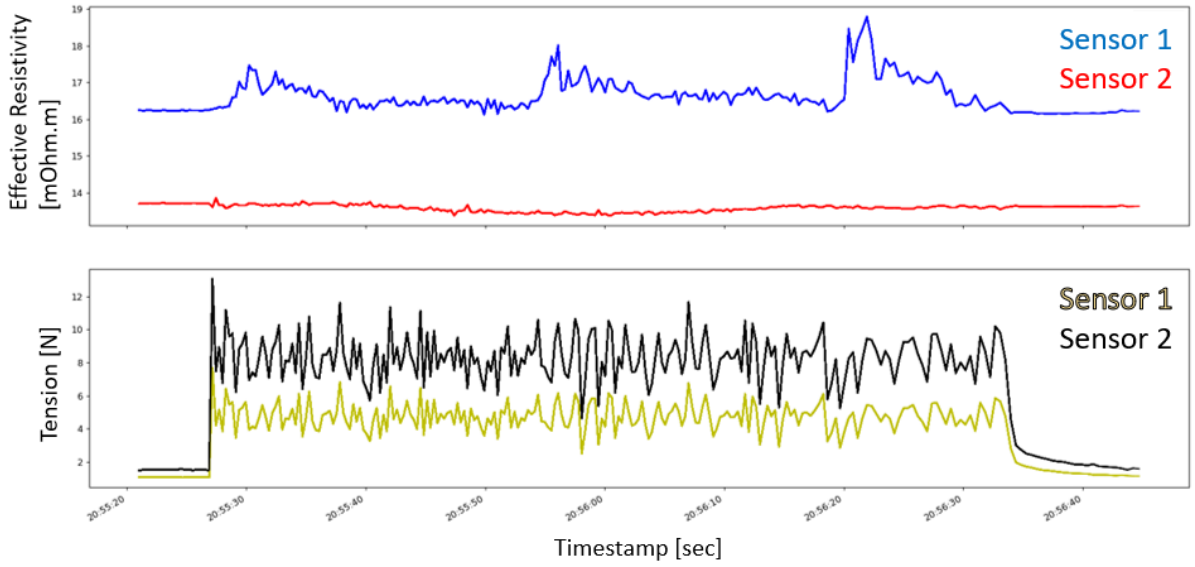


**(a)** Waviness Example Case 1.

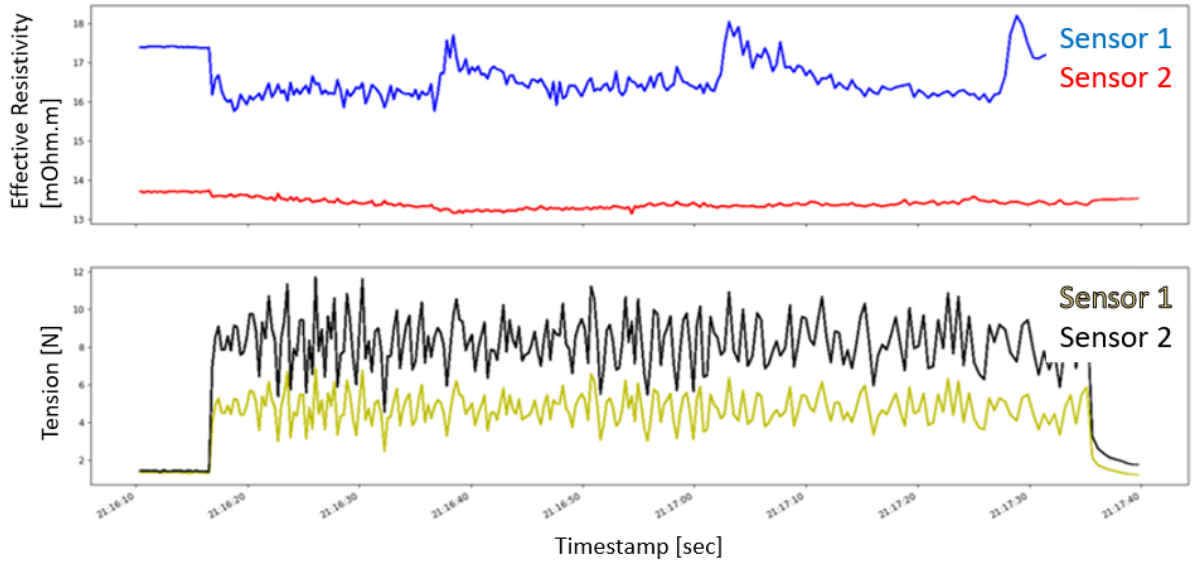


**(b)** Waviness Example Case 2.

**Figure 3.12:** Live view of Tension (Yellow/Black) and Resistivity (Blue/Red) sensors. Response check via natural waviness of tow. Blue and red regions indicate resistivity before and after spreading respectively. The x-axis shows the timestamp during the live operation. Waviness of tow section is visible in the blue region as peaks, but evens out after spreading.

As figure 3.12 indicates, waviness in tows can be detected by resistivity sensors. This is represented as the peaks in the blue plots. However, contrary to tow damage, sensor 2 does not detect this behaviour. This can be explained by the fact that the spreading operation homogenizes the carbon tow, reducing the waviness by minimizing local energy via friction events. This straightening of the tow is also observed visually by eye. By using this configuration, damage and waviness can both be measured. A distinction can then be made based on whether the signal remains, worsens (which can happen when damage grows), or reduces.

A set of experiments has been done to quantitatively establish the resistivity values at which tow damage and waviness responses read. Results hereof can be seen in figure 3.13. Since it has already been noted that the first sensor provides the most data on anomalies, this sensors' output value is used.

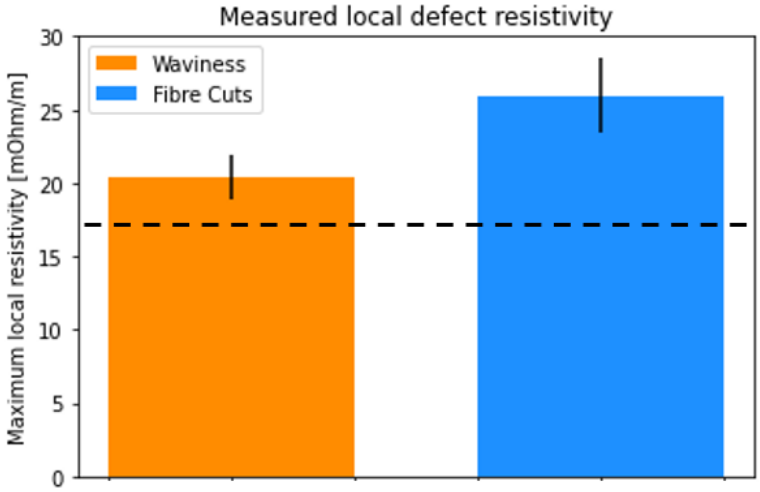


**Figure 3.13:** Resistivity response at waviness and tow damage. The dashed black line indicates the average baseline value (of sensor 1). Black vertical lines on the plot indicate standard deviation ranges.

It can be said that the sections of cut carbon provide a more notable output deviation than the wavy sections. This would make sense, since broken fibers generally cannot transfer (electrical) load and thereby reduce the effective material cross-section by definition. Further investigation is recommended to explore and measure other damage scenarios.

## 3.3. Analysis of Carbon Fiber Orientation and Geometry

Here, results are displayed of the optical analysis and measurement techniques described before. First, fiber orientation results are presented, after which a comparison is made to the resistivity based results to try to detect any correlation. Lastly, a short note is given on the width changes that were recorded during the experiments.

### 3.3.1. Orientation Analysis of Filaments in Tow

In this section, measurement data is displayed which is obtained from software as explained in section 2.3.2. Using this custom code and a camera, lines are found in the tow which represent the individual fibres. Based on the locations of these newly found data points from lines, several major lines are plotted on top of the original image in real-time. Then, the standard deviations of these angles are saved before and after the spreading operation in an attempt to assess the straightness of the fibres in the tow both before and after spreading.

3 separate standard deviation recordings are made per wrap angle setting, of which each recording has a duration of 1 minute (at 30 Hz) at a pulling speed of 4.4 cm/s and a pre-tension level of 3/5. Wrap angles have been adjusted according to 0, 40, 80, 115, 150, and 170 degrees. Figure 3.14a shows an example of plotted (live) standard deviations for pre- and post-spreading conditions for a 115 degree wrap angle setup. Figure 3.14b shows the absolute difference between these, as a conceptual quantification of the *reduction in standard deviation due to the spreading process*. All records of this measurement series can be viewed in Appendix C. Note that there is a time difference between the instants that a section of tow is captured by camera 1 and camera 2, due to the required travel time of the tow moving from camera 1 to camera 2. The displayed graphs have been adjusted for this offset.

The complete results are summarized in figure 3.15, where the differences in standard deviations, before and after spreading, are compared for setups with 0, 40, 80, 115, 150, and 170 degree wrap angles respectively. The plot shows the *average reduction of standard deviation of the fiber direction in the tow section*, per wrap angle. Note that the 115 degree wrap angle case (plotted in red) contains 3 data points, of which the upper 2 are plotted on top of each other.

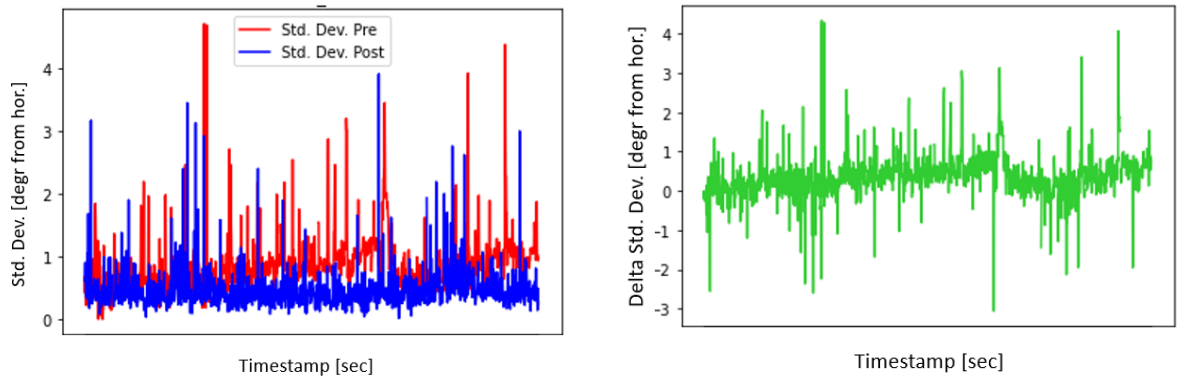


**(a)** Individual responses of cameras 1 and 2.

**(b)** Absolute difference between responses 1 and 2.

**Figure 3.14:** Standard deviation recordings of camera 1 (pre-) and camera 2 (post-spread), and their absolute difference. From 3rd run of 115degree WA setup.

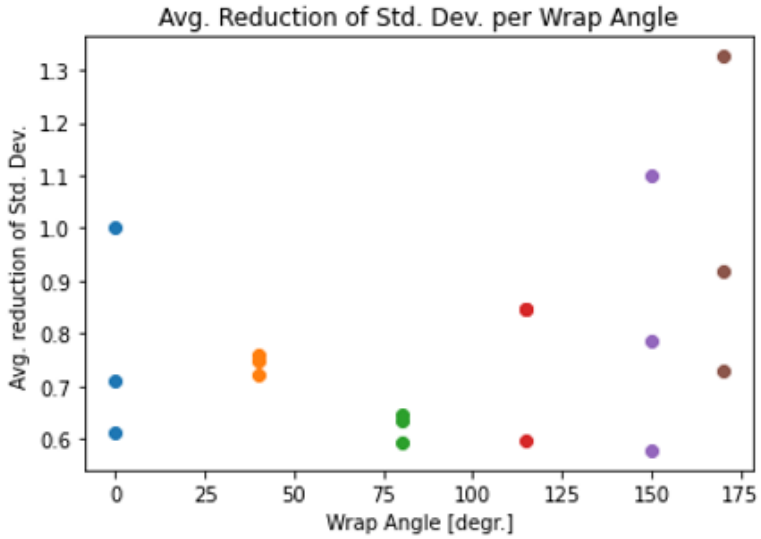


**Figure 3.15:** Overview of reduction of std. dev. per wrap angle.

What can be seen from figure 3.15 is that a generally increasing trend could be present. This would suggest that an increase in wrap angle correlates with an increased reduction of standard deviation during the spreading process. This would indicate that a greater wrap angle results in a more uniform tow, having a lower standard deviation in internal fiber directions. However, measurements at 0 degree wrap angles still indicate a reduction in standard deviation, which is virtually impossible as no spreader bars were installed for this case. To check whether the tensionmeters perhaps introduced some friction, their responses were examined. Tensionmeters 1 and 2 returned similar tension values for the 0 degree case, confirming that indeed no (spreading) friction was applied to the tow at these instances. This offset is thought to be due to slightly variating light conditions between the cameras, and the suspicion that the camera sensors are slightly different from one another. Because of this, this monitoring technique is still considered as concept, and further research should be performed to improve the robustness of the analysis method. One additional notable point is that the 40, 80, and 115 degree data is relatively close together. Seeing the apparent uncertainties in the system, this form of consistency was not expected.

### 3.3.2. Overlap of Resistivity and Optical Measurements

As is evident from figure 3.14, many noise spikes are returned during the measurement. It has been found that these spikes originate from (potentially) random artefacts such as contamination or loose fibres. This is shown in figures 3.16, 3.17, and 3.18, where applied cuts, waviness, or foreign particles respectively make for a jump in the standard deviation value.

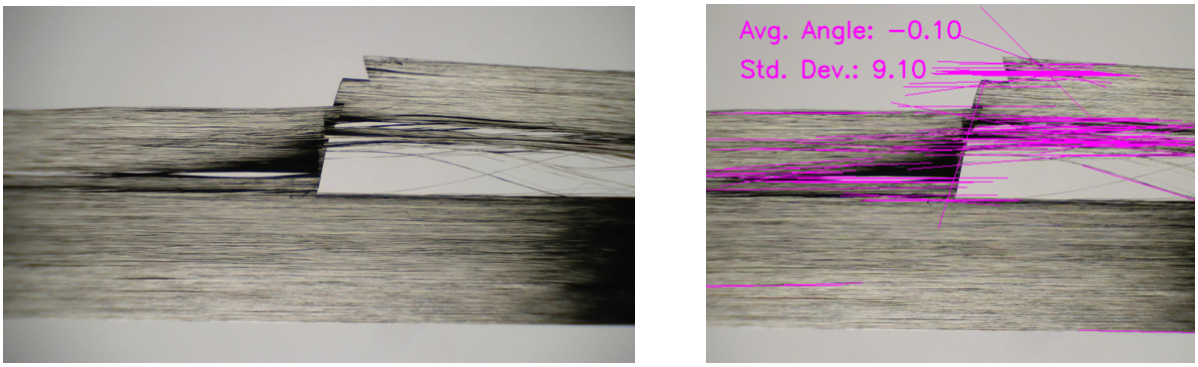


**(a)** Waviness in tow. **(b)** Software response.

**Figure 3.16:** Live feed of directional analysis 1 - peaks in std. dev. can partially be explained by deviating carbon architecture.

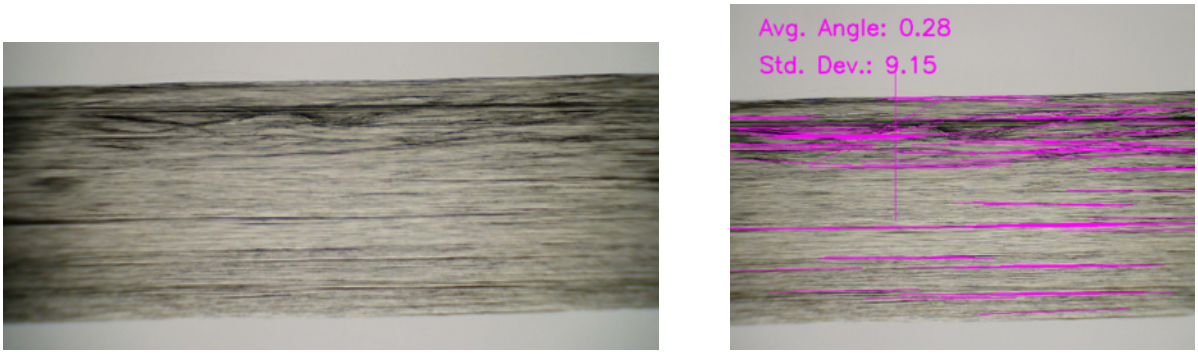


**(a)** Cut damage in tow. **(b)** Software response.

**Figure 3.17:** Live feed of directional analysis 2 - peaks in std. dev. can partially be explained by deviating carbon architecture.

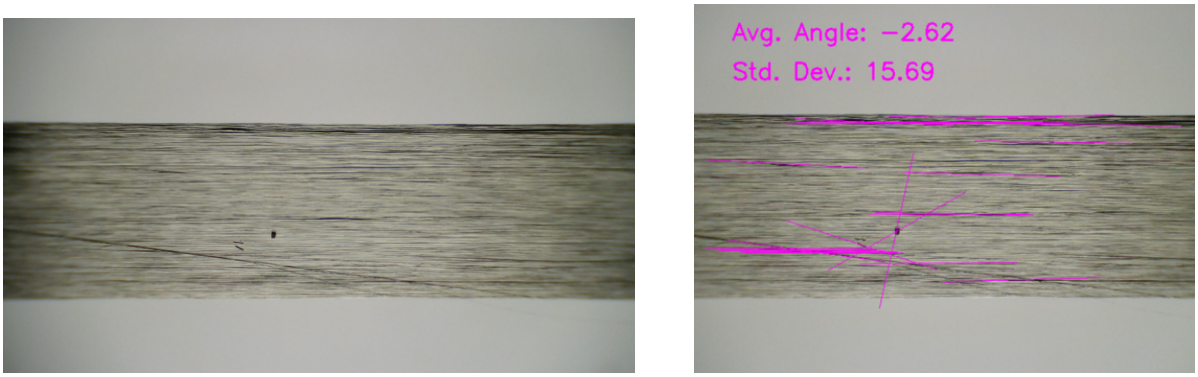


**(a)** Foreign particles in tow. **(b)** Software response.

**Figure 3.18:** Live feed of directional analysis 3 - peaks in std. dev. can partially be explained by deviating carbon architecture.

This behaviour is compared with the responses from the resistivity sensors in an attempt to find any correlation between the two novel monitoring methods. The results are plotted in figure 3.19.

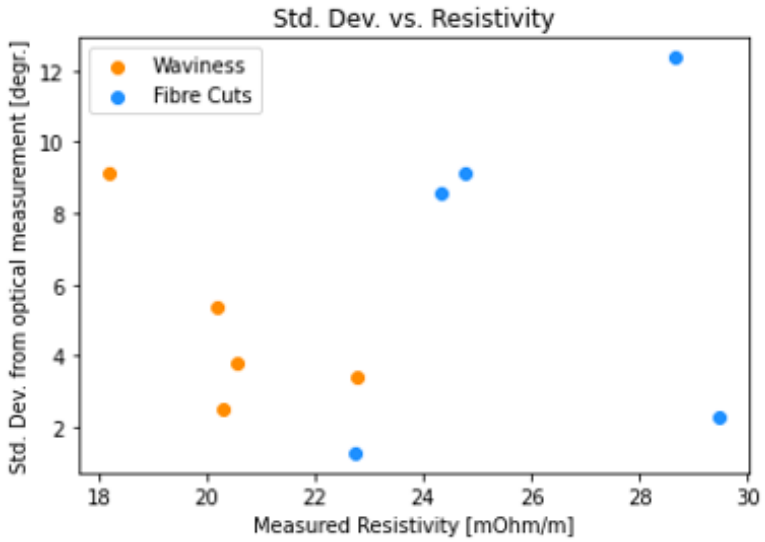


**Figure 3.19:** Quantitative comparison of anomaly spikes detected by resistivity vs. optical analysis.

It has to be noted that there is no visible correlation (quantitative) to be read from figure 3.19. Although anomalies are often recognized by both systems, the optical based orientation analysis seems to have trouble with connecting an appropriate quantitative value to its output. This could partially be caused by the fact that the areal density of the plotted lines is not controlled, meaning that the contribution of anomalies in the standard deviation might be unpredictable. This is also supported by figure 3.15, where no clear trend can be stated. Another point off criticism is that the hardware should be upgraded to identical high quality cameras, instead of cameras with (slightly) variating sensors. Also, both measurement methods rely on a different plane of the carbon tow: resistivity relies on contact area, while the optical system relies on a 2-dimensional picture. It has been noted that certain out-of-plane effects can occur, where part of the tow is tensioned to a lesser extend. This results in a reduced electrical contact, increasing apparent resistivity. The optical analysis does not handle these cases well. It either seems to not spot it at all, since all fiber directions are generally still aligned, or it recognizes the resulting shadows as lines and develops a wrong fit. Future work is recommended, as also stated in section 4.3.

### 3.3.3. Extent of Spreading

Using the developed width-detection software, as described in section 2.3, pre-spreading and post-spreading widths were measured inline. The used 12K Toray roving has a nominal width of a measured 6.15 mm. The results are displayed in figure 3.20 as a percentage of increase in tow width.

From section 3.1, results indicate that the pulling speed has an effect on the apparent friction coefficient; higher pulling velocities results in generally higher apparent friction. Also, lower pre-tension has a similar effect. Since spreading relies on present friction, machine settings were chosen such that the highest apparent friction coefficient was generated. The machine ran at $100\%$ velocity (for the current gear set, 7.7 cm/s) and at a pre-tension brake setting of 1 out of 5.

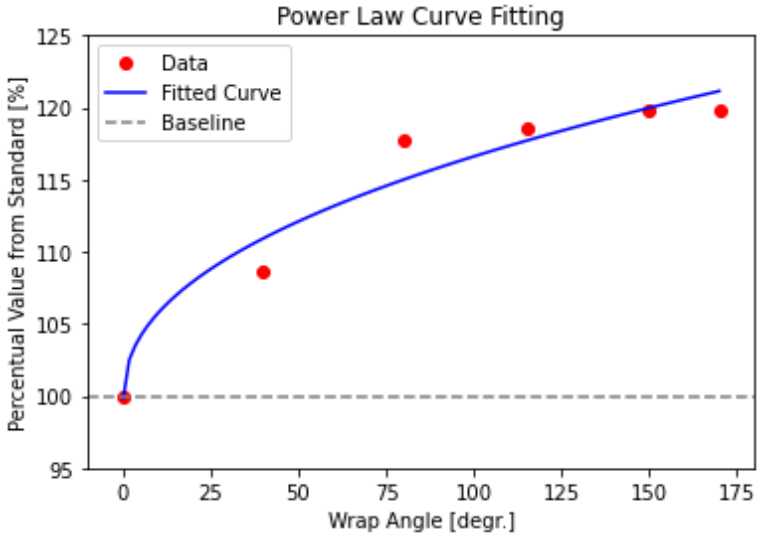


**Figure 3.20:** Increase of tow width expressed as percentage of original width.

From the graph it appears that the spreading width increase approaches an asymptotic value at around $120\%$ for this setup. A power law function has been fitted to the data according to equation 3.1, where $\phi$ is defined as the wrap angle. A power law function has been chosen because these are well-suited for capturing asymptotic behavior since they offer a concise representation of long-term trends and provide valuable information about the rate of growth without requiring complex mathematical formulations.

$$\%_{Increase} = 2.11 * \phi^{0.45} + 99.81 \tag{3.1}$$

It has to be noted that a greater wrap angle results in a higher tension ratio $T2/T1$, as seen in section 3.1. Therefore, as the wrap angle increases, the fibers are tensioned to a greater extend at the location of the second measurement (post-spread). This additional tension could potentially limit the freedom of the fibers, reducing the width increase. Regarding the fit, data is generally well covered. However, it seems as if the percentual width approaches an asymptotic value around $120\%$. To better understand these properties, further research is required.

# 4

# Conclusion and Recommendations

In this chapter, the conclusions are presented in terms of three sections. First, a summary of the findings is given along with an explanation. Then, the implications of the study are mentioned. Lastly, recommendations for future work are noted and explained.

## 4.1. Summary of Findings and Recommended Continuations

The findings of the completed experiments are highlighted in this section, subdivided into *Friction Studies, Resistivity Measurements, Optical Analysis, and Width Increase*.

### 4.1.1. Friction Studies

- Friction Behavior and the Capstan Friction Equation: In the analysis of carbon fiber tow spreading, it was observed that the friction behavior did not align with the predictions of the standard capstan friction equation. The capstan friction equation is commonly used to estimate the frictional forces in systems involving wrapped elements, such as cables or fibers. However, in the case of carbon tow spreading, the observed friction behavior deviated from this equation. This discrepancy suggests that further research is necessary to understand the underlying mechanisms governing the frictional behavior of carbon fiber tows. Investigating the factors that influence the interaction between the tow and the spreading mechanism will be crucial to develop a more accurate model or equation that can predict the friction behavior.
- Pre-Tension and Friction Coefficient: An intriguing finding in the analysis of carbon tow friction behavior was the observation that the friction coefficient of interaction appeared to decrease as the pre-tension increased. This trend was notable when the pre-tension was increased by adjusting the mechanical brake. In other words, as the initial tension applied to the carbon tow increased, the frictional resistance encountered during spreading was reduced. This finding suggests that the relationship between pre-tension and apparent friction coefficient in carbon tow spreading is complex and merits further investigation. Understanding the underlying mechanisms behind this behavior will enable more precise control of the spreading process and optimization of the frictional characteristics.
- Tension Ratio and Pulling Speed: Another significant observation was that increasing the pulling speed during carbon tow spreading resulted in an increased tension ratio. The tension ratio represents the ratio of the actual tension in the tow during spreading to the initial pre-tension applied. This means that higher pulling speeds led to greater tension in the tow relative to the applied pre-tension. The relationship between pulling speed and tension ratio is essential to consider in practical applications, as it indicates that the spreading process is influenced by the rate at which the tow is pulled. This finding underscores the importance of carefully controlling the pulling speed to achieve desired tension levels and avoid excessive tension that may affect the integrity of the carbon fiber tow or the spreading mechanism.

These three findings collectively highlight the need for further research and understanding of carbon fiber tow spreading. Investigating the complex friction behavior, exploring the relationship between pre-tension and friction coefficient, and considering the impact of pulling speed on tension ratios will contribute to advancing the knowledge and optimizing the processes involved in carbon fiber tow spreading.

### 4.1.2. Resistivity Measurements

- Inline Measurement of Carbon Fiber Resistivity Properties: The resistivity properties of carbon fiber were successfully measured inline, yielding repeatable outcomes. The inline measurement refers to the ability to assess the resistivity properties of carbon fiber during the actual production or processing stages. This capability is crucial for quality control and process optimization. The results obtained from the measurements were consistent and reliable, indicating that the inline resistivity measurement technique can provide valuable insights into the electrical conductivity characteristics of carbon fiber. Moreover, it was observed that the tension applied to the carbon fiber during measurement had a partial influence on the measured resistivity properties, suggesting that tension plays a role in the electrical behavior of carbon fiber.
- Identification of Anomalies Using Resistivity Sensors: The resistivity sensors employed in the study enabled the repeated measurement of anomalies such as fiber cuts and waviness in the carbon fiber tow. These anomalies could be consistently detected and characterized using the resistivity measurement technique. Furthermore, the observed anomalies were found to be associated with areas of partial tension in the tow. This finding suggests that deviations in tension distribution along the tow can manifest as observable anomalies in the resistivity measurements. By identifying and understanding these anomalies, it becomes possible to gain insights into the tension distribution and integrity of the carbon fiber tow, leading to improved quality control and defect detection in the manufacturing process.
- Mitigating Fiber Breakage in Resistivity Measurement: During resistivity measurement, it was observed that damage to the carbon fiber occurred as a result of contact with the copper bars used in the measurement setup. To minimize fiber breakage and ensure accurate measurements, certain measures were employed. Firstly, reducing the wrap angle, which refers to the angle of contact between the tow and the copper bars, helped mitigate fiber breakage. It was also noted that the accuracy of the resistivity measurements was not compromised by these modifications, as the nature of the 4-point resistance measurement method allowed for precise and reliable data collection.

These additional findings on resistivity measurements expand the understanding of carbon fiber properties and the application of resistivity sensors in assessing their characteristics. The ability to measure resistivity inline with repeatable outcomes, the identification and explanation of anomalies using resistivity sensors, and the optimization of measurement techniques to minimize fiber breakage collectively contribute to the advancement of quality control and process optimization in carbon fiber manufacturing.

### 4.1.3. Optical Analysis

- Challenges in Predictable Fiber Orientation with Optical Analysis: In the optical analysis of carbon fiber tow, it was observed that while the orientation of fibers within a tow appears to follow certain predictable patterns, the current technology and methods employed were unable to consistently produce repeatable and verifiable results. Despite efforts to monitor and measure the orientations using custom Python software and two cameras, there were inherent limitations and uncertainties in achieving consistent outcomes. This suggests that further advancements are required in the technology and techniques used for optical analysis to enhance the reliability and repeatability of fiber orientation measurements. Ongoing research is necessary to improve the accuracy and consistency of the optical analysis method for assessing fiber orientations within a carbon tow.
- Differences between Optical Analysis and Resistivity Measurements: A notable finding in the study was that optical orientation cameras and resistivity sensors, employed for measuring fiber orientations and resistivity properties, respectively, inherently measure different properties of the carbon tow. One key difference arises from out-of-plane effects, which can affect the accuracy

of optical measurements. These effects occur when fibers deviate from the plane of observation, leading to potential inaccuracies in measuring their orientations. Furthermore, the software used for optical analysis might not be fully ready or optimized to handle all scenarios, resulting in challenges and limitations. In contrast, resistivity sensors focus on measuring the electrical properties of the tow. These differences in measurement principles highlight the need to consider multiple techniques and approaches when characterizing different aspects of carbon fiber tows. By combining the strengths of optical analysis and resistivity measurements, a more comprehensive understanding of the tow properties can be obtained.

The findings related to optical analysis highlight the current challenges and limitations in achieving predictable and repeatable fiber orientation measurements. Further advancements in technology and techniques are required to enhance the reliability and consistency of optical analysis. Additionally, the intrinsic differences between optical analysis and resistivity measurements, such as out-of-plane effects and differences in the measured properties, underscore the importance of employing multiple complementary methods for a comprehensive characterization of carbon fiber tows. Continued research and development in these areas will contribute to improved analysis techniques and a deeper understanding of carbon fiber behavior.

### 4.1.4. Extent of Spreading

- Tow Width Increase and Wrap Angle Spreading Settings: In the study investigating the tow width increase for various wrap angle spreading settings, it was observed that as the wrap angle increased, the width of the tow also increased. This finding indicates that there is a direct correlation between the wrap angle and the resulting tow width. Notably, it was observed that the width increase reached asymptotic behaviour at a width value of around $120\%$ of the initial width. This suggests that there is a maximum width achievable for the tow, beyond which further increases in wrap angle have diminishing effects on the width.

The observed asymptotic behavior in tow width could potentially be attributed to the tension properties within the system, particularly in the post-spreading stage. Tension plays a critical role in the spreading process, and as the wrap angle increases, the tension distribution along the tow becomes more significant. At a certain point, the tension forces exerted on the tow may reach a threshold where they counterbalance the spreading forces, resulting in the observed width asymptote. Further research is necessary to gain a deeper understanding of the tension properties in the system and their influence on the width increase with varying wrap angles.

By examining the relationship between wrap angle and tow width increase, this study contributes to the understanding of the spreading process and the factors that affect tow dimensions. The observed asymptotic behavior suggests the presence of tension-related mechanisms, highlighting the importance of considering tension properties, particularly in the post-spreading stage. Further investigations into the tension distribution and its interaction with the spreading forces will enable the optimization of tow width control and improve the efficiency of carbon fiber spreading processes.

## 4.2. Implications of the Study

The comprehensive study conducted on carbon fiber tow spreading, encompassing various aspects such as friction behavior, pre-tension effects, pulling speed, resistivity measurements, optical analysis, and tow width increase, has significant implications for the understanding and optimization of carbon fiber manufacturing processes. The following implications arise from the key findings discussed:

1. Advancing the Understanding of Friction Behavior: The observation that the friction behavior of carbon fiber tows does not align with the standard capstan friction equation underscores the need for further research to uncover the underlying mechanisms. Exploring the factors influencing friction behavior will facilitate the development of more accurate models and equations for predicting and controlling friction in carbon fiber spreading processes.

2. Optimizing Pre-Tension Settings: The finding that increasing pre-tension, either through wrap angle or adjusting the pre-tension (PT) setting, leads to a reduction in the friction coefficient of interaction provides valuable insights for process optimization. Understanding the complex relationship between pre-tension and friction coefficient is crucial for achieving precise control over the spreading process and enhancing the frictional characteristics of carbon fiber tows.
3. Controlling Pulling Speed and Tension Ratios: The observation that increased pulling speed during spreading results in higher tension ratios emphasizes the need to carefully manage the rate at which the tow is pulled. This finding highlights the importance of controlling pulling speed to achieve desired tension levels and avoid excessive tension, which could compromise the integrity of the carbon fiber tow or the spreading mechanism.
4. Enhancing Quality Control with Resistivity Measurements: The successful inline measurement of resistivity properties provides a valuable tool for quality control during carbon fiber production. The ability to measure resistivity inline and detect anomalies, such as fiber cuts and waviness, aids in identifying areas of partial tension in the tow and improving defect detection. Further research and advancements in resistivity measurement techniques will enhance the reliability and repeatability of these measurements.
5. Advancing Optical Analysis for Fiber Orientation: The study reveals the challenges associated with optical analysis of fiber orientations within carbon tows, such as limited repeatability and verification. This highlights the need for continued advancements in technology and methods to improve the reliability and consistency of fiber orientation measurements. Combining optical analysis with other complementary techniques, such as resistivity measurements, will provide a more comprehensive understanding of the properties of carbon fiber tows.
6. Considering Multiple Tow Properties: The differences between optical analysis and resistivity measurements, such as out-of-plane effects and the measured properties, emphasize the importance of employing multiple techniques for a comprehensive characterization of carbon fiber tows. Taking into account various properties, including fiber orientation, resistivity, and tow width, will enable a more holistic understanding of the spreading process and contribute to process optimization.
7. Tension-Related Implications: The observed tow width increase reaching an asymptote, possibly influenced by tension properties in the system, may highlight the significance of tension distribution, particularly in the post-spreading stage. Further research into tension-related mechanisms will aid in optimizing tow width control and enhancing the efficiency of carbon fiber spreading processes.

In conclusion, this study provides valuable insights into the behavior and properties of carbon fiber tows during spreading processes. The implications derived from the findings have far-reaching implications for improving process control, optimizing spreading techniques, enhancing quality control measures, and advancing the understanding of tension-related mechanisms. Continued research and technological advancements will drive further progress in carbon fiber manufacturing, ultimately leading to improved product quality, performance, and applications across various industries.

## 4.3. Further Recommendations

The study findings suggest several recommendations to further improve the understanding and optimization of carbon fiber tow spreading processes. These recommendations encompass advancements in measurement techniques, process control, waste reduction, and exploring additional aspects of friction behavior and tow width.

Improved Measurement Techniques:

- Develop an improved electrical mechanical brake system for active torque control to enhance control over tension and reduce the ”springy carbon tow” effect. This will contribute to better understanding and control of friction behavior.
- Implement rotating resistivity bars or explore contactless measurement methods such as eddy current or high voltage to minimize damage to the carbon tow during resistivity measurements. This will enhance measurement accuracy and preserve the integrity of the tow.

Enhanced Optical Analysis:

- Incorporate a 3D camera system to eliminate the impact of waviness and improve the accuracy of fiber orientation measurements. This will provide more reliable and precise data for further analysis.
- Focus on improving the code robustness for optical analysis software to ensure consistent and reliable results in measuring fiber orientations.

Waste Reduction and Environmentally Friendly Practices:

- Consider the implementation of a tow collector or binder deposition station at the end of the line to prevent wastage of experimentally used carbon tow. This will help reduce material waste and optimize the utilization of resources.
- Alternatively, explore options for recycling the carbon tow, such as chopping and recycling it for forged carbon applications. This environmentally friendly approach will contribute to sustainable practices in carbon fiber manufacturing.

Further Investigation of Friction Behavior:

- Conduct a more extensive study on friction behavior by incorporating superimposed wrap angles to explore similarities or differences in the behavior. This analysis could lead to the development of an analytical solution for predicting friction behavior in carbon tow spreading.

Tow Width Analysis:

- Increase the number of data points and consider incorporating tension relaxation measurements to gain a more comprehensive understanding of tow width spread. This analysis will provide insights into the distribution and behavior of tow width during spreading.

Comprehensive Mapping and Analysis of Resistivity Results:

- Expand the resistivity measurement experiments by repeating tests and adding more damage cases to further map and validate the resistivity results. This will enhance the reliability and robustness of the resistivity measurement technique.

Analyze the Effects of Friction on Resistivity Measurements:

- Investigate the impact of friction on resistivity measurements and analyze any potential damage caused by the measurement process. Understanding the relationship between friction and resistivity will provide insights into the accuracy and reliability of resistivity measurements.

Implementing these recommendations will contribute to advancements in measurement techniques, process control, waste reduction, and a deeper understanding of the behavior and properties of carbon fiber tows during spreading processes. These improvements will facilitate the optimization of manufacturing processes, enhance quality control measures, and promote sustainability in carbon fiber production.

# References


[1] G. Gardiner and W. Happach, “The spread of spread tow,” 2018.

[2] R. Amacher, J. Cugnoni, J. Botsis, L. Sorensen, W. Smith, and C. Dransfeld, “Thin ply composites: Experimental characterization and modeling of size-effects,” *Composites Science and Technology.*, 2014.

[3] R. C. Murray, “An investigation into fibre spreading.,” Accessed 04-2022.

[4] J. Cugnoni, R. Amacher, S. Kohler, *et al.*, “Towards aerospace grade thin-ply composites: Effect of ply thickness, fibre, matrix and interlayer toughening on strength and damage tolerance.,” *Composites Science and Technology*, 2016.

[5] S. Choi and B. V. Sankar, “Gas permeability of various graphite/epoxy composite laminates for cryogenic storage systems,” 2008.

[6] A. Schlothauer, G. A. Pappas, and P. Ermanni, “Aterial response and failure of highly deformable carbon fiber composite shells,” *Composites Science and Technology.*, 2020.

[7] A. Schlothauer, N. Schwob, G. A. Pappas, and P. Ermanni, “Thin-ply thermoplastic composites for foldable structures,” 2020.

[8] P. M. Pawar and R. Ganguli, “On the effect of progressive damage on composite helicopter rotor system behavior,” *Composite Structures*, 2007.

[9] H. S. KatzJohn and V. Milewski, “Composite heat shield patent us3203849a,” 1961.

[10] Y. Huang and R. Young, “Effect of fibre microstructure upon the modulus of pan- and pitch-based carbon fiber,” 1995.

[11] D. Stefaniak and C. Dransfeld, “Industrial composite manufacturing lecture slides.,” 2021.

[12] M. Troughton, “Handbook of plastics joining,” 2009.

[13] S.-J. Park and M.-K. Seo, “Manufacture of carbon fiber composites,” 2018.

[14] M. A. Naeem, W. Yu, Y.-h. Zhenga, and Y. He, “Structure and spinning of composite yarn based on the multifilament spreading method using a modified ring frame.,” 2014.

[15] P. Singh, “Microstructure formation in tow spreading.,” *TUDelft*, 2021.

[16] A. Ahmad and B. Davijani, “Experiments and prediction of the spreading behavior of fibrous tows by means of the discrete element method.,” 2012.

[17] M. S. Irfan, V. R. Machavaram, R. C. Murray, *et al.*, “The design and optimisation of a rig to enable the lateral spreading of fibre bundles,” *Journal of Composite Materials*, pp. 1813–1831, 2014.

[18] M. S. Irfan, V. R. Machavaram, R. Mahendran, and G. F. Fernando, “Lateral spreading of a fiber bundle via mechanical means.,” 2012.

[19] B. Cornelissen, “The role of friction in tow mechanics.,” *The Title of the Journal*, 2012.

[20] H. M. El-Dessouky, “Spread tow technology for ultra lightweight cfrp composites: Potential and possibilities,” Accessed 06-2022.

[21] W. K. Happach, “Automatic tape width control for a carbon fiber bar spreading process.,” Accessed 06-2022.

[22] Q. Li, A. L.Woodhead, J. S. Church, and M. Naebe, “On the detection of carbon fbre storage contamination and its efect on the fbre–matrix interface.,” 2018.

[23] N. Wu, X. Xie, J. Yang, *et al.*, “Effect of normal load on the frictional and wear behaviour of carbon fiber in tow-on-tool contact during three-dimensional weaving process,” 2020.

[24] Y. Liu, Z. Xiang, X. Zhou, Z. Wu, and X. Hu, “An improved nonlinear model considering relative velocity for the friction behavior between untwisted glass-fiber tow and roller,” *The Title of the Journal*, 2021.

[25] S. Gomarasca, D. Peeters, B. Atli-Veltin, and C. Dransfeld, “Characterising microstructural organisation in unidirectional composites.,” *TUDelft*, 2021.

[26] I. E. Sawi, P. A. Olivier, P. Demont, and H. Bougherara, “Processing and electrical characterization of a unidirectional cfrp composite filled with double walled carbon nanotubes,” 2012.

[27] C. P. B. Jr., “The analysis of carbon fibre strength distributions exhibiting multiple modes of failure,” 1982.

[28] H. A. Mahmud, M. S. Radue, W. A. Pisani, and G. M. Odegard, “Computational modeling of hybrid carbon fiber/epoxy composites reinforced with functionalized and non-functionalized graphene nanoplatelets,” 2021.

[29] B. Caglar, G. Broggi, M. A. Ali, L. Orgéas, and V. Michaud, “Deep learning accelerated prediction of the permeability of fibrous microstructures,” 2022.

[30] P. Böhler, “Aachen reinforced symposium,” 2022.

# A

# Technical Specifications of the Carbon Fiber Tow Spreading Machine

## A.1. Frame Elements

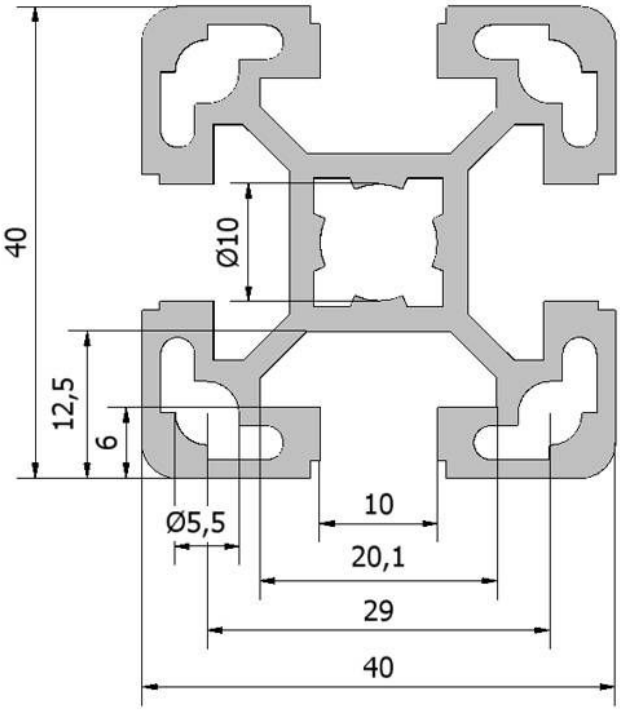


**Figure A.1:** Cross-section of 40x40mm frame elements.

## A.2. Mechanical Brake

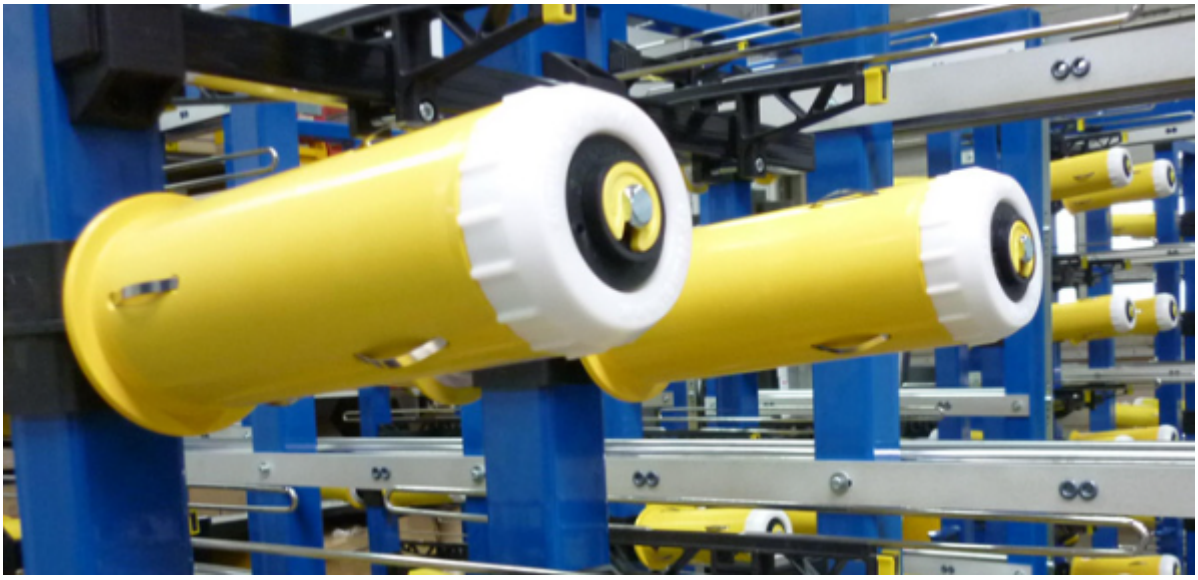

**Figure A.2:** Picture of spring-loaded Texmer creel in a factory setting. From Texmer GMBH.

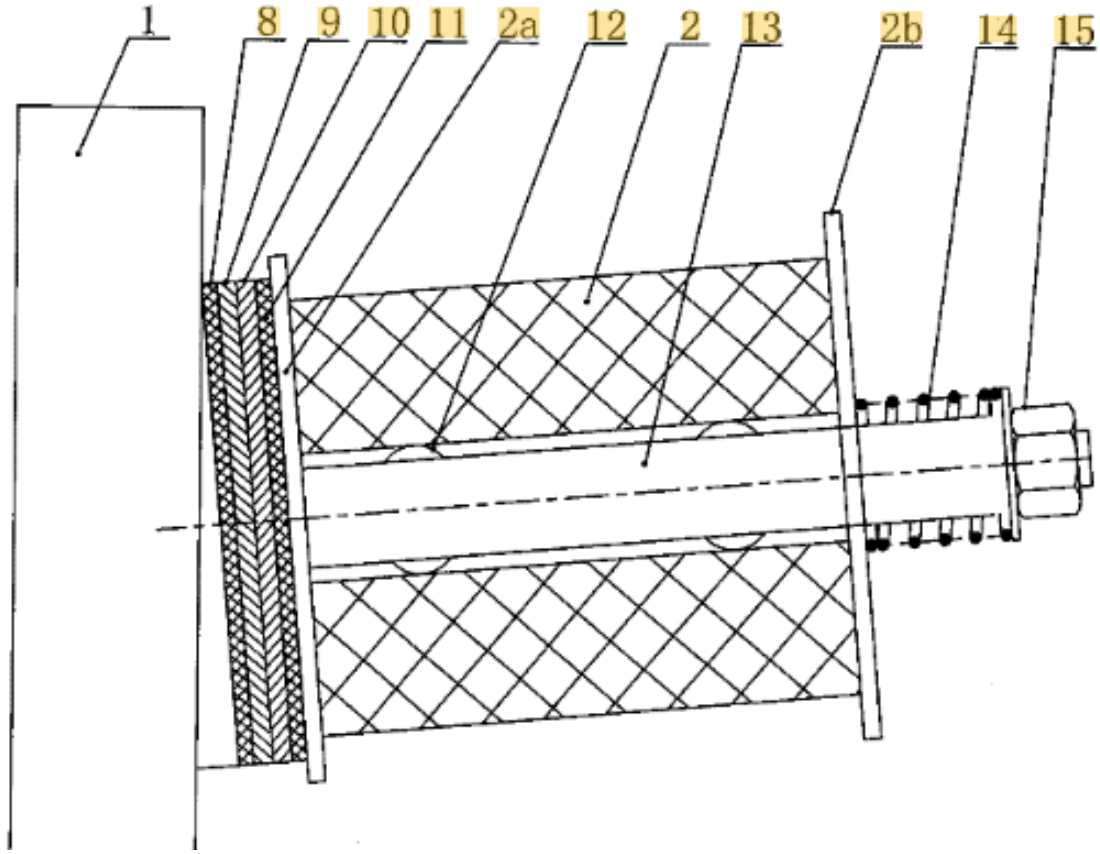


**Figure A.3:** Diagram of cross-section of spring-loaded creel. As the clamping force is increased via 15, The friction assembly of 8, 9, 10, and 11 is pressed harder against the mount 1. This results in a higher static friction. From Jiangsu Xinyang new material Limited by Share Ltd.

# A.3. Motor Specifications

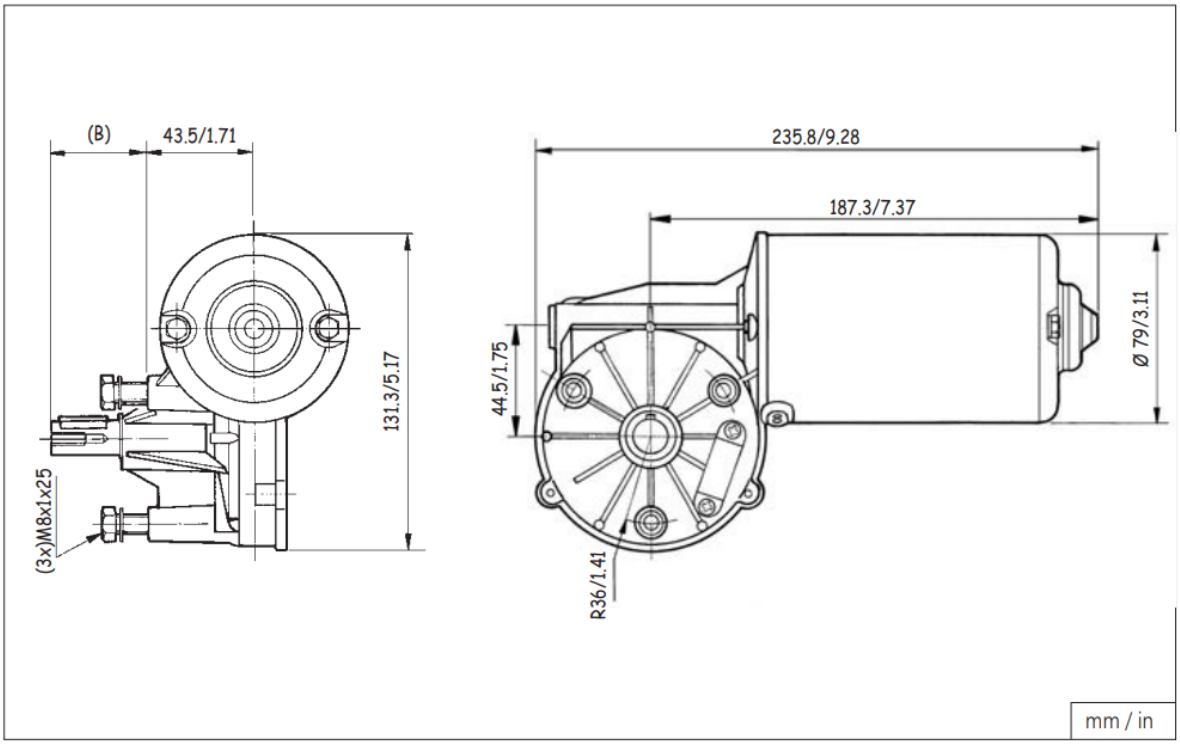


**Figure A.4:** Motor Dimensions

| Reference number<br>Referencia | Nominal voltage<br>Tensión nominal | Nominal torque<br>Par nominal | Nominal speed<br>Velocidad nominal | Nominal current<br>Corriente nominal | Starting torque<br>Par de arranque | Starting current<br>Corriente de Arranque | Shaft<br>Eje | Connections<br>Conexiones | Wiring diag.<br>Esq. eléct. | Transmission ratio<br>Relación de reducción | Approximate weight<br>Peso aproximado | Grado de estanqueidad<br>Watertightness | Wheel material<br>Material rueda | Curve<br>Curva |
|---|---|---|---|---|---|---|---|---|---|---|---|---|---|---|
| | **Un (V)** | **Mn (N.m./Lbf.in)** | **Nn (r.p.m.)** | **In (A)** | **Ma (N.m./Lbf.in)** | **Ia (A)** | | | | **i** | **P (kg / Lb.t)** | **IP** | | |
| 258.1710.20.00 | 12 | 15 / 133 | 25 | 10 | 80 / 708 | 42 | E36 | C34 | F2 | 52:1 | 3.00 / 8 | IP53 | PLA | 18 |
| 258.1710.30.00 | 24 | 15 / 133 | 25 | 5 | 80 / 708 | 21 | E36 | C34 | F2 | 52:1 | 3.00 / 8 | IP53 | PLA | 18 |
| 258.3710.20.00 | 12 | 15 / 133 | 25 | 10 | 80 / 708 | 42 | E36 | C34 | EE2 | 52:1 | 3.00 / 8 | IP53 | PLA | 18 |
| 258.3710.30.00 | 24 | 15 / 133 | 25 | 5 | 80 / 708 | 21 | E36 | C34 | EE2 | 52:1 | 3.00 / 8 | IP53 | PLA | 18 |
| 258.3712.20.00 | 12 | 12 / 106 | 40 | 12 | 80 / 708 | 55 | E36 | C34 | EE2 | 52:1 | 3.00 / 8 | IP53 | PLA | 19 |
| 258.3712.30.00 | 24 | 12 / 106 | 40 | 6 | 80 / 708 | 32 | E36 | C34 | EE2 | 52:1 | 3.00 / 8 | IP53 | PLA | 19 |
| 258.9026.20.00 | 12 | 12 / 106 | 40 | 12 | 80 / 708 | 55 | E36 | C34 | EE2 | 52:1 | 3.00 / 8 | IP53 | CEL | 19 |
| 258.9026.30.00 | 24 | 12 / 106 | 40 | 6 | 80 / 708 | 32 | E36 | C34 | EE2 | 52:1 | 3.00 / 8 | IP53 | CEL | 19 |

**Figure A.5:** Motor Specs 1


**Figure A.6:** Motor Specs 2

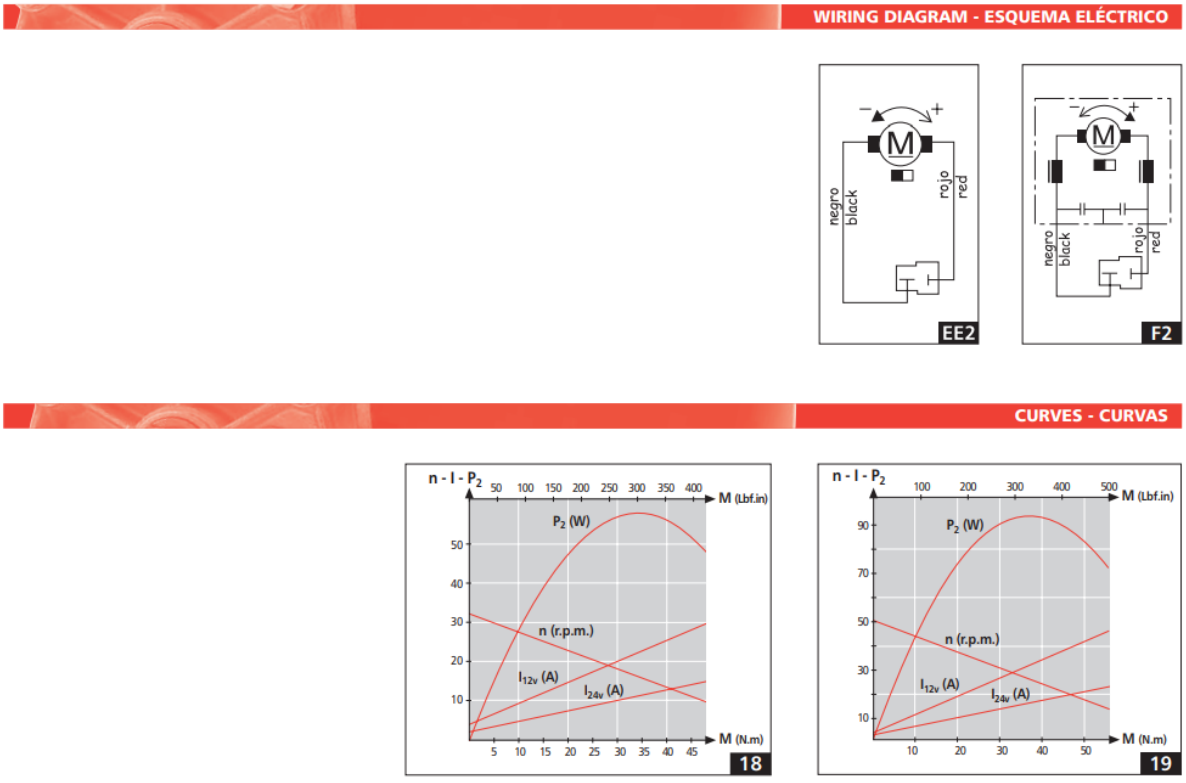


**Figure A.7:** Motor Specs 3

# A.4. Power Supplies

| Output Specification | |
|---|---|
| **Number of Outputs** | 1 |
| **DC Voltage** | 24V |
| **Ripple & Noise (max.)** | <150mVp-p |
| **Rated Current** | 10A |
| **Rated Power** | 240W |
| **Voltage Tolerance** | ±1.0% |
| **Line Regulation** | ±0.5% |
| **Load Regulation** | ±1.0% |

**Figure A.8:** Motor PSU Output Specifications.

SPECIFICATION

| MODEL | | LRS-100-3.3 | LRS-100-5 | LRS-100-12 | LRS-100-15 | LRS-100-24 | LRS-100-36 | LRS-100-48 |
|---|---|---|---|---|---|---|---|---|
| OUTPUT | DC VOLTAGE | 3.3V | 5V | 12V | 15V | 24V | 36V | 48V |
| | RATED CURRENT | 20A | 18A | 8.5A | 7A | 4.5A | 2.8A | 2.3A |
| | CURRENT RANGE | 0 ~ 20A | 0 ~ 18A | 0 ~ 8.5A | 0 ~ 7A | 0 ~ 4.5A | 0 ~ 2.8A | 0 ~ 2.3A |
| | RATED POWER | 66W | 90W | 102W | 105W | 108W | 100.8W | 110.4W |
| | RIPPLE & NOISE (max.) Note.2 | 100mVp-p | 100mVp-p | 120mVp-p | 120mVp-p | 150mVp-p | 200mVp-p | 200mVp-p |
| | VOLTAGE ADJ. RANGE | 2.97 ~ 3.6V | 4.5 ~ 5.5V | 10.2 ~ 13.8V | 13.5 ~ 18V | 21.6 ~ 28.8V | 32.4 ~ 39.6V | 43.2 ~ 52.8V |
| | VOLTAGE TOLERANCE Note.3 | ±3.0% | ±2.0% | ±1.0% | ±1.0% | ±1.0% | ±1.0% | ±1.0% |
| | LINE REGULATION Note.4 | ±0.5% | ±0.5% | ±0.5% | ±0.5% | ±0.5% | ±0.5% | ±0.5% |
| | LOAD REGULATION Note.5 | ±2.0% | ±1.0% | ±0.5% | ±0.5% | ±0.5% | ±0.5% | ±0.5% |
| | SETUP, RISE TIME | 500ms, 30ms/230VAC 500ms,30ms/115VAC at full load | | | | | | |
| | HOLD UP TIME (Typ.) | 55ms/230VAC 10ms/115VAC at full load | | | | | | |

**Figure A.9:** Sensor PSU Output Specifications. Note that the resistivity sensors are not powered by this PSU but by Constant Current Sources.

# A.5. Drive Train

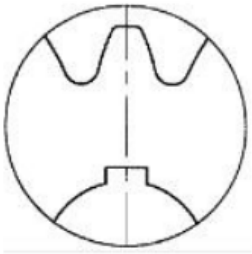

| D (H7) | b (H9) | T | | M |
|---|---|---|---|---|
| 10 | 3 | D + 1,4 | (+0,1/0) | M3 |
| 11 | 4 | D + 1,8 | (+0,1/0) | M3 |
| 12 | 4 | D + 1,8 | (+0,1/0) | M3 |
| 14 | 5 | D + 2,3 | (+0,1/0) | M4 |
| 15 | 5 | D + 2,3 | (+0,1/0) | M4 |
| 16 | 5 | D + 2,3 | (+0,1/0) | M4 |
| 18 | 6 | D + 2,8 | (+0,1/0) | M5 |
| 19 | 6 | D + 2,8 | (+0,1/0) | M5 |
| 20 | 6 | D + 2,8 | (+0,1/0) | M5 |
| 22 | 6 | D + 2,8 | (+0,1/0) | M5 |
| 24 | 8 | D + 3,3 | (+0,2/0) | M6 |
| 25 | 8 | D + 3,3 | (+0,2/0) | M6 |
| 28 | 8 | D + 3,3 | (+0,2/0) | M6 |
| 30 | 8 | D + 3,3 | (+0,2/0) | M6 |
| 32 | 10 | D + 3,3 | (+0,2/0) | M8 |
| 35 | 10 | D + 3,3 | (+0,2/0) | M8 |
| 38 | 10 | D + 3,3 | (+0,2/0) | M8 |
| 40 | 12 | D + 3,3 | (+0,2/0) | M10 |
| 42 | 12 | D + 3,3 | (+0,2/0) | M10 |
| 45 | 14 | D + 3,8 | (+0,2/0) | M12 |
| 48 | 14 | D + 3,8 | (+0,2/0) | M12 |
| 50 | 14 | D + 3,8 | (+0,2/0) | M12 |
| 60 | 18 | D + 4,4 | (+0,2/0) | M12 |
| 65 | 18 | D + 4,4 | (+0,2/0) | M12 |
| 70 | 20 | D + 4,9 | (+0,2/0) | M12 |

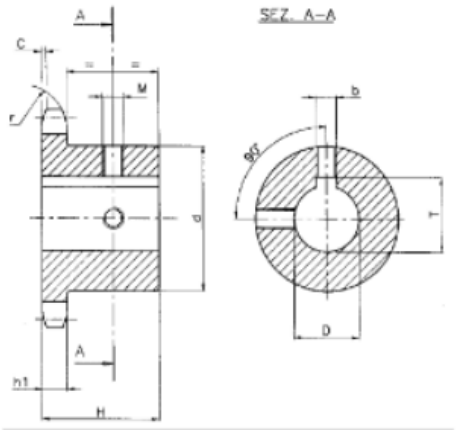


**Figure A.10:** Technical Drawings Drivetrain Gears.

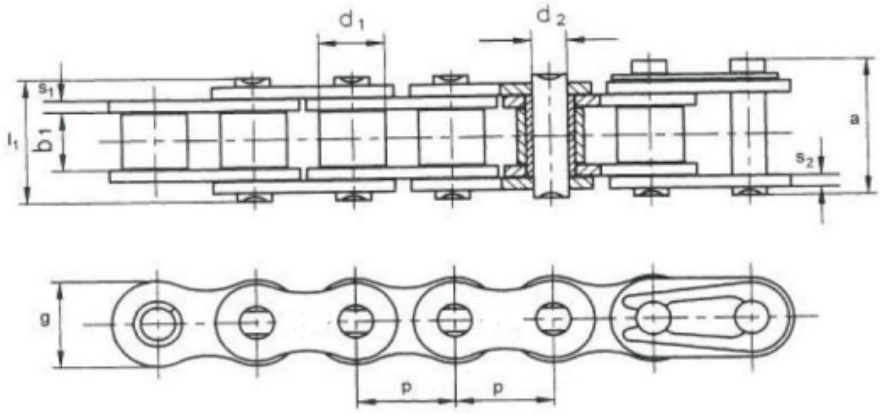


| Ketten-Nr. | Teilung p mm | lichte Weite Innenglied $b_1$ mm min. | Rollen-durchm. $d_1$ mm max. | Bolzen-durchm. $d_2$ mm max. | Laschen-höhe g mm max. | Laschen-dicke innen/außen $s_1/s_2$ mm max. | Bolzen-länge $l_1$ mm max. | a mm max. | Bruchkraft standard FB kN min. | Bruchkraft ∅ erreicht kN | Ge-wicht q kg/m ca. |
|---|---|---|---|---|---|---|---|---|---|---|---|
| K 03 | 5,000 | 2,50 | 3,20 | 1,49 | 4,1 | 0,6 | 7,4 | 9,9 | 2,20 | 2,40 | 0,08 |
| K 04-1 | 6,000 | 2,80 | 4,00 | 1,85 | 5,0 | 0,6 | 7,4 | 10,3 | 3,00 | 3,30 | 0,11 |
| K 05B-1 | 8,000 | 3,00 | 5,00 | 2,31 | 7,1 | 0,8 | 8,6 | 11,7 | 5,00 | 5,90 | 0,20 |
| K *06B-1 | 9,525 | 5,72 | 6,35 | 3,28 | 8,2 | 1,3/1,0 | 13,5 | 16,8 | 9,00 | 10,40 | 0,41 |
| K 081 | 12,700 | 3,30 | 7,75 | 3,66 | 9,9 | 1,2/1,0 | 10,2 | 11,7 | 8,20 | 9,00 | 0,28 |
| K 082 | 12,700 | 2,38 | 7,75 | 3,66 | 9,9 | 1,1 | 8,2 | - | 10,00 | 11,00 | 0,26 |
| K 083 | 12,700 | 4,88 | 7,75 | 4,09 | 10,3 | 1,5 | 12,9 | 14,4 | 12,00 | 13,20 | 0,42 |
| K 084 | 12,700 | 4,88 | 7,75 | 4,09 | 11,1 | 1,9/1,6 | 14,8 | 16,3 | 16,00 | 17,60 | 0,59 |
| K 085 | 12,700 | 6,38 | 7,77 | 3,58 | 9,9 | 1,3 | 14,0 | 16,0 | 6,80 | 7,50 | 0,38 |
| K 08B-1 | 12,700 | 7,75 | 8,51 | 4,45 | 11,8 | 1,6 | 17,0 | 20,9 | 18,00 | 19,40 | 0,70 |
| K 10B-1 | 15,875 | 9,65 | 10,16 | 5,08 | 14,7 | 1,7 | 19,6 | 23,7 | 22,40 | 27,50 | 0,93 |
| K 12B-1 | 19,050 | 11,68 | 12,07 | 5,72 | 16,1 | 1,8 | 22,7 | 27,3 | 29,00 | 32,20 | 1,15 |
| K 16B-1 | 25,400 | 17,02 | 15,88 | 8,28 | 21,0 | 4,1/3,1 | 36,1 | 41,5 | 60,00 | 72,80 | 2,71 |
| K 20B-1 | 31,750 | 19,56 | 19,05 | 10,19 | 26,4 | 4,5/3,5 | 43,2 | 49,3 | 95,00 | 106,70 | 3,70 |
| K 24B-1 | 38,100 | 25,40 | 25,40 | 14,63 | 33,2 | 6,0/4,8 | 53,4 | 60,0 | 160,00 | 178,00 | 7,10 |
| K 28B-1 | 44,450 | 30,99 | 27,94 | 15,90 | 36,7 | 7,5/6,0 | 65,1 | 72,5 | 200,00 | 222,00 | 8,50 |
| K 32B-1 | 50,800 | 30,99 | 29,21 | 17,81 | 42,0 | 7,0/6,0 | 67,4 | 75,3 | 250,00 | 277,50 | 10,25 |
| K 40B-1 | 63,500 | 38,10 | 39,37 | 22,89 | 52,9 | 8,5/8,0 | 82,6 | 92,6 | 355,00 | 394,00 | 16,35 |
| K 48B-1 | 76,200 | 45,72 | 48,26 | 29,24 | 63,8 | 12/10 | 99,1 | 109,1 | 560,00 | 621,60 | 25,00 |
| K 56B-1 | 88,900 | 53,34 | 53,96 | 34,32 | 77,8 | 13/12 | 114,0 | 125,0 | 850,00 | 935,00 | 35,00 |
| K 64B-1 | 101,600 | 60,96 | 63,50 | 39,40 | 90,1 | 14/13 | 130,0 | 143,0 | 1.100,00 | 1.210,00 | 60,00 |
| K 72B-1 | 114,300 | 68,58 | 72,39 | 44,50 | 103,6 | 17/15 | 147,0 | 161,0 | 1.400,00 | 1.540,00 | 80,00 |

*a) Bolzenlänge Verschlussglied, * in der Ausführung mit geraden Laschen*

**Figure A.11:** Technical Drawings Drivetrain Chain.

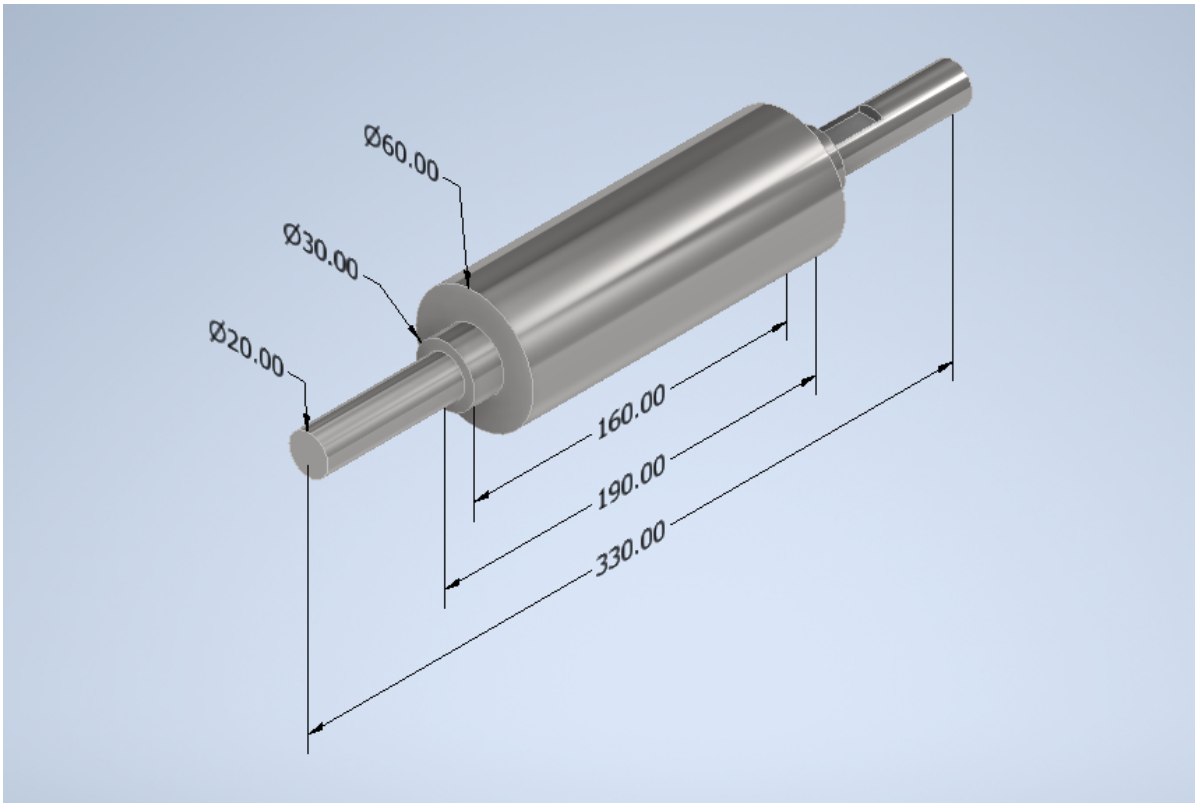


**Figure A.12:** CAD of Pulling Axle.

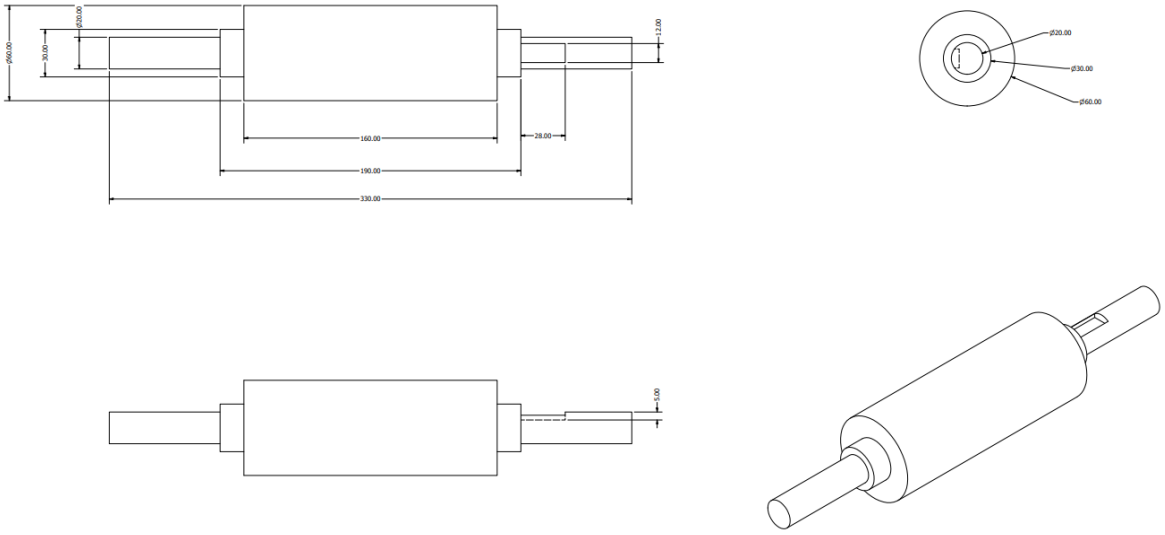


**Figure A.13:** Technical Drawings of the Pulling Axles.

## A.6. Initial CAD Concept Design

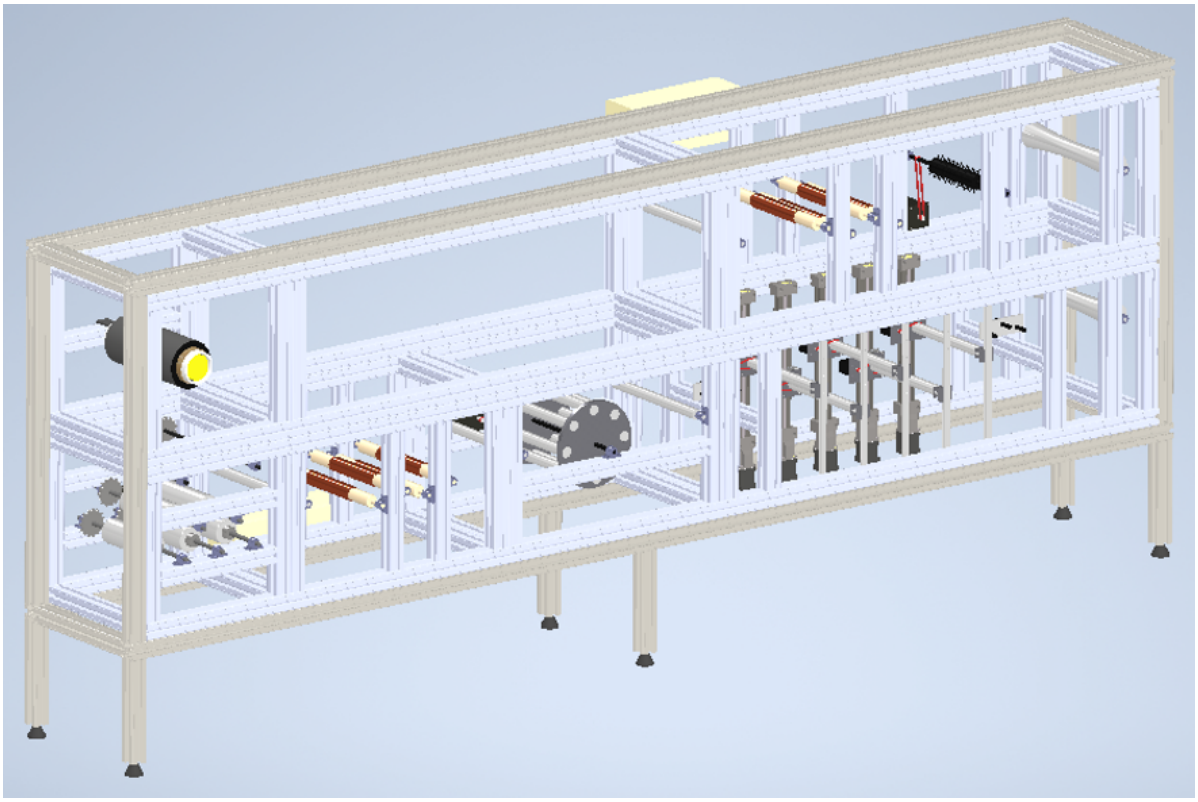

**Figure A.14:** Initial concept CAD of spreading line.

## A.7. Machine Functions Diagram

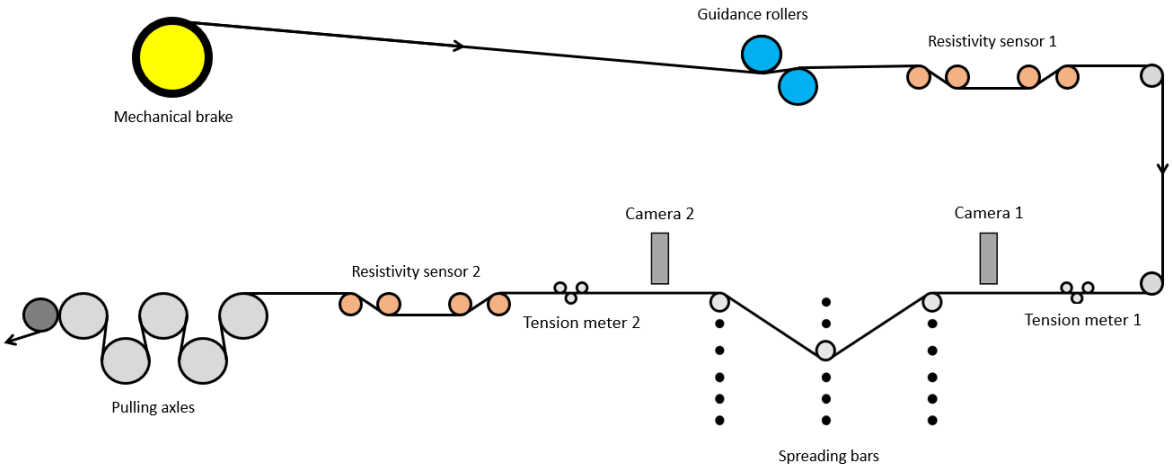


**Figure A.15:** Initial concept CAD of spreading line.

## A.8. Spreader Bar Concepts

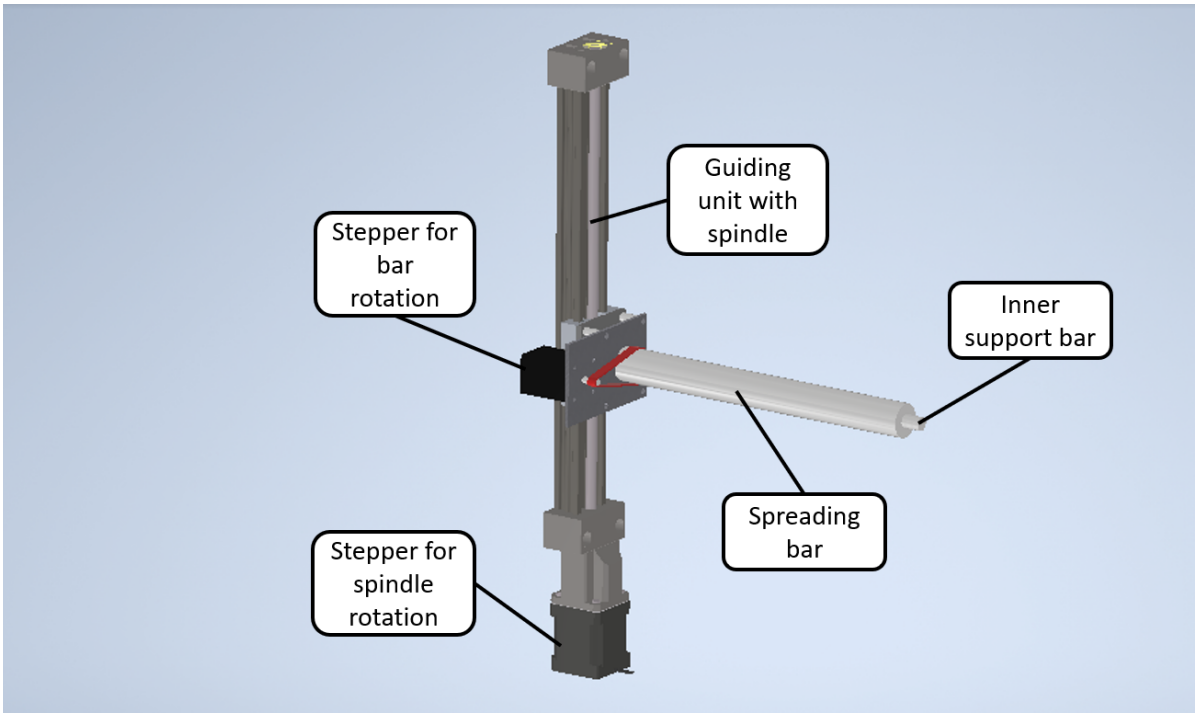


**Figure A.16:** CAD of Spreader Bar concept 1.

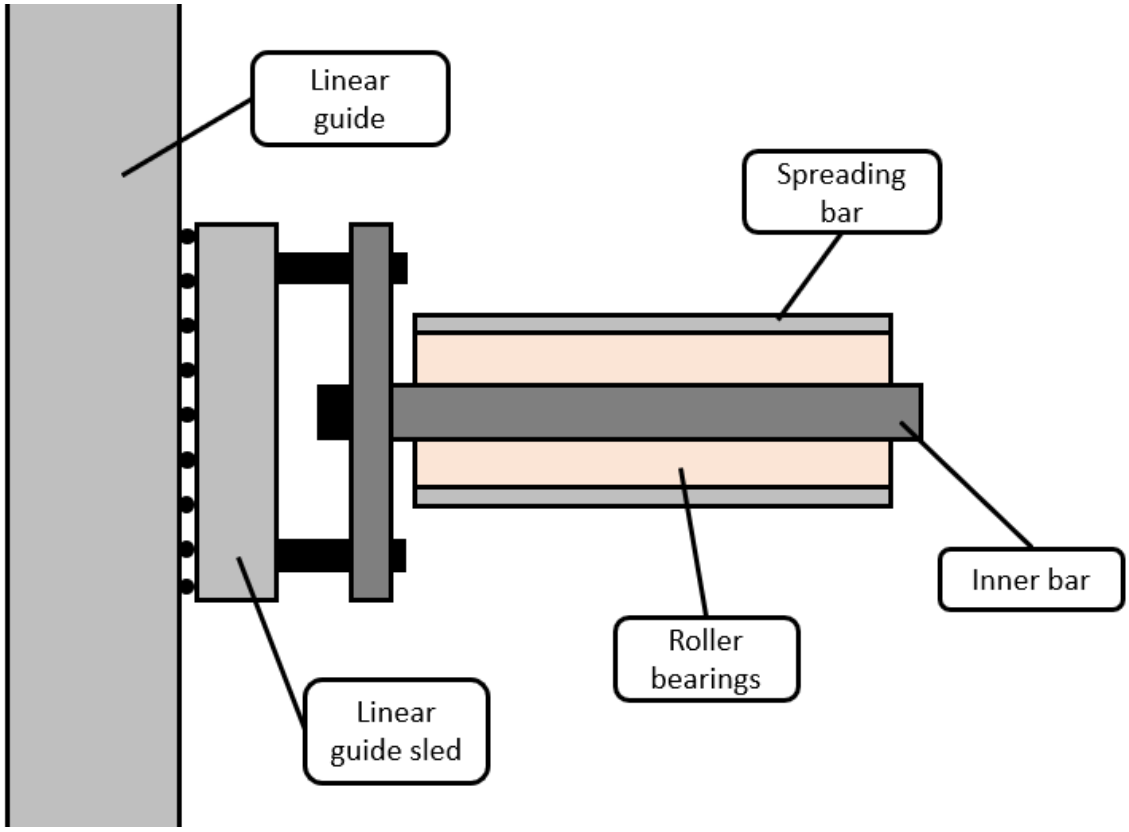


**Figure A.17:** Detail of rotating bar connection.

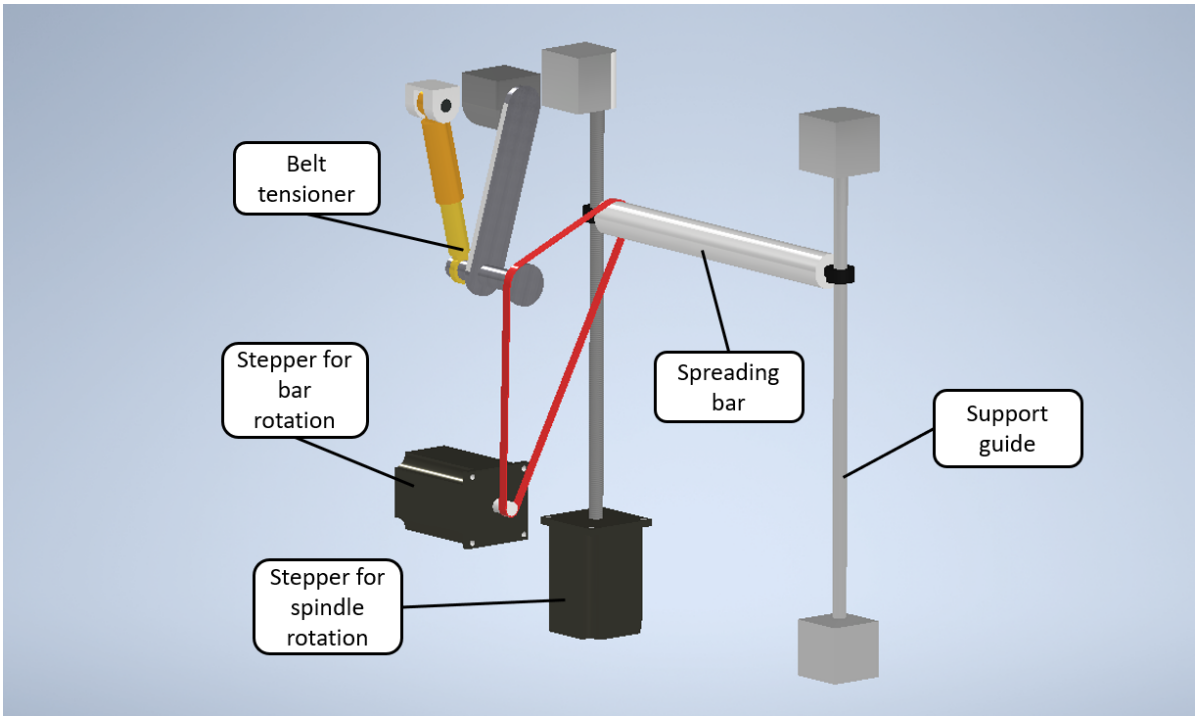


**Figure A.18:** CAD of Spreader Bar concept 2.

# A.9. Connectors

**Y-bearing plummer block units with a cast housing and grub screws, metric shafts**
d **12 – 60** mm

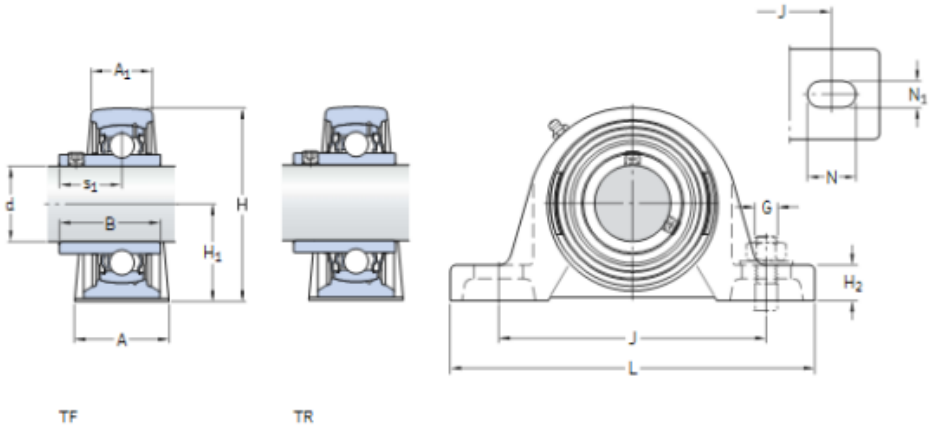


TF TR

| Dimensions | | | | | | | | | | | | | Basic load ratings | | Fatigue load limit | Limiting speed | Designation |
|---|---|---|---|---|---|---|---|---|---|---|---|---|---|---|---|---|---|
| | | | | | | | | | | | | | dynamic | static | | with shaft tolerance h6 | Bearing unit |
| d | A | $A_1$ | B | H | $H_1$ | $H_2$ | J | L | N | $N_1$ | G | $s_1$ | C | $C_0$ | $P_u$ | | |
| mm | | | | | | | | | | | | | kN | | kN | r/min | – |
| **12** | 32 | 18 | 27,4 | 57 | 30,2 | 14 | 97 | 127 | 20,5 | 11,5 | 10 | 15,9 | 9,56 | 4,75 | 0,2 | 9 500 | **SY 12 TF** |
| **15** | 32 | 18 | 27,4 | 57 | 30,2 | 14 | 97 | 127 | 20,5 | 11,5 | 10 | 15,9 | 9,56 | 4,75 | 0,2 | 9 500 | **SY 15 TF** |
| **17** | 32 | 18 | 27,4 | 57 | 30,2 | 14 | 97 | 127 | 20,5 | 11,5 | 10 | 15,9 | 9,56 | 4,75 | 0,2 | 9 500 | **SY 17 TF** |
| **20** | 32 | 21 | 31 | 65 | 33,3 | 14 | 97 | 127 | 20,5 | 11,5 | 10 | 18,3 | 12,7 | 6,55 | 0,28 | 8 500 | **SY 20 TF** |
| | 34 | 23 | 31 | 65 | 33,3 | 14 | 97 | 127 | 20,7 | 13 | 10 | 18,3 | 12,7 | 6,55 | 0,28 | 8 500 | **SYJ 20 TF** |
| | 32 | 21 | 31 | 65 | 33,3 | 14 | 97 | 127 | 20,5 | 11,5 | 10 | 18,3 | 12,7 | 6,55 | 0,28 | 5 000 | **SY 20 TR** |
| **25** | 36 | 22 | 34,1 | 70,5 | 36,5 | 16 | 102 | 130 | 19,5 | 11,5 | 10 | 19,8 | 14 | 7,8 | 0,335 | 7 000 | **SY 25 TF** |
| | 38 | 24 | 34,1 | 70,5 | 36,5 | 16 | 102,5 | 140 | 21,5 | 13 | 10 | 19,8 | 14 | 7,8 | 0,335 | 7 000 | **SYJ 25 TF** |
| | 36 | 22 | 34,1 | 70,5 | 36,5 | 16 | 102 | 130 | 19,5 | 11,5 | 10 | 19,8 | 14 | 7,8 | 0,335 | 4 300 | **SY 25 TR** |
| **30** | 40 | 25 | 38,1 | 82,5 | 42,9 | 17 | 117,5 | 152 | 23,5 | 14 | 12 | 22,2 | 19,5 | 11,2 | 0,475 | 6 300 | **SY 30 TF** |
| | 42 | 27 | 38,1 | 82,5 | 42,9 | 16 | 118 | 165 | 24 | 17 | 14 | 22,2 | 19,5 | 11,2 | 0,475 | 6 300 | **SYJ 30 TF** |
| | 40 | 25 | 38,1 | 82,5 | 42,9 | 17 | 117,5 | 152 | 23,5 | 14 | 12 | 22,2 | 19,5 | 11,2 | 0,475 | 3 800 | **SY 30 TR** |
| **35** | 45 | 27 | 42,9 | 93 | 47,6 | 19 | 126 | 160 | 21 | 14 | 12 | 25,4 | 25,5 | 15,3 | 0,655 | 5 300 | **SY 35 TF** |
| | 46 | 28 | 42,9 | 93 | 47,6 | 17 | 129 | 167 | 24 | 17 | 14 | 25,4 | 25,5 | 15,3 | 0,655 | 5 300 | **SYJ 35 TF** |
| | 45 | 27 | 42,9 | 93 | 47,6 | 19 | 126 | 160 | 21 | 14 | 12 | 25,4 | 25,5 | 15,3 | 0,655 | 3 200 | **SY 35 TR** |
| **40** | 48 | 30 | 49,2 | 99 | 49,2 | 19 | 135,5 | 175 | 24,5 | 14 | 12 | 30,2 | 30,7 | 19 | 0,8 | 4 800 | **SY 40 TF** |
| | 49 | 31 | 49,2 | 99 | 49,2 | 18 | 136,5 | 184 | 25,5 | 17 | 14 | 30,2 | 30,7 | 19 | 0,8 | 4 800 | **SYJ 40 TF** |
| | 48 | 30 | 49,2 | 99 | 49,2 | 19 | 135,5 | 175 | 24,5 | 14 | 12 | 30,2 | 30,7 | 19 | 0,8 | 2 800 | **SY 40 TR** |
| **45** | 48 | 32 | 49,2 | 107,5 | 54 | 21 | 143,5 | 187 | 22,5 | 14 | 12 | 30,2 | 33,2 | 21,6 | 0,915 | 4 300 | **SY 45 TF** |
| | 52 | 36 | 49,2 | 107,5 | 54 | 20 | 143,5 | 190 | 23,5 | 17 | 14 | 30,2 | 33,2 | 21,6 | 0,915 | 4 300 | **SYJ 45 TF** |
| | 48 | 32 | 49,2 | 107,5 | 54 | 21 | 143,5 | 187 | 22,5 | 14 | 12 | 30,2 | 33,2 | 21,6 | 0,915 | 2 400 | **SY 45 TR** |
| **50** | 54 | 34 | 51,6 | 114,5 | 57,2 | 22 | 157 | 203 | 26 | 18 | 16 | 32,6 | 35,1 | 23,2 | 0,98 | 4 000 | **SY 50 TF** |
| | 58 | 38 | 51,6 | 114,5 | 57,2 | 22 | 157,5 | 206 | 26,5 | 20 | 16 | 32,6 | 35,1 | 23,2 | 0,98 | 4 000 | **SYJ 50 TF** |
| | 54 | 34 | 51,6 | 114,5 | 57,2 | 22 | 157 | 203 | 26 | 18 | 16 | 32,6 | 35,1 | 23,2 | 0,98 | 2 200 | **SY 50 TR** |
| **55** | 60 | 40 | 55,6 | 126 | 63,5 | 24 | 171,5 | 219 | 27,5 | 18 | 16 | 33,4 | 43,6 | 29 | 1,25 | 3 600 | **SY 55 TF** |
| | 60 | 40 | 55,6 | 126 | 63,5 | 24 | 171,5 | 219 | 27,5 | 20 | 16 | 33,4 | 43,6 | 29 | 1,25 | 3 600 | **SYJ 55 TF** |
| | 60 | 40 | 55,6 | 126 | 63,5 | 24 | 171,5 | 219 | 27,5 | 18 | 16 | 33,4 | 43,6 | 29 | 1,25 | 1 900 | **SY 55 TR** |
| **60** | 60 | 42 | 65,1 | 138 | 69,8 | 26,5 | 190,5 | 240 | 29,5 | 18 | 16 | 39,7 | 52,7 | 36 | 1,53 | 3 400 | **SY 60 TF** |
| | 65 | 47 | 65,1 | 138 | 69,8 | 26,5 | 188,5 | 241 | 29,5 | 20 | 16 | 39,7 | 52,7 | 36 | 1,53 | 3 400 | **SYJ 60 TF** |
| | 60 | 42 | 65,1 | 138 | 69,8 | 26,5 | 190,5 | 240 | 29,5 | 18 | 16 | 39,7 | 52,7 | 36 | 1,53 | 1 800 | **SY 60 TR** |

**Figure A.19:** Specifications of bearing assemblies. 20mm I.D. used for pulling axles.

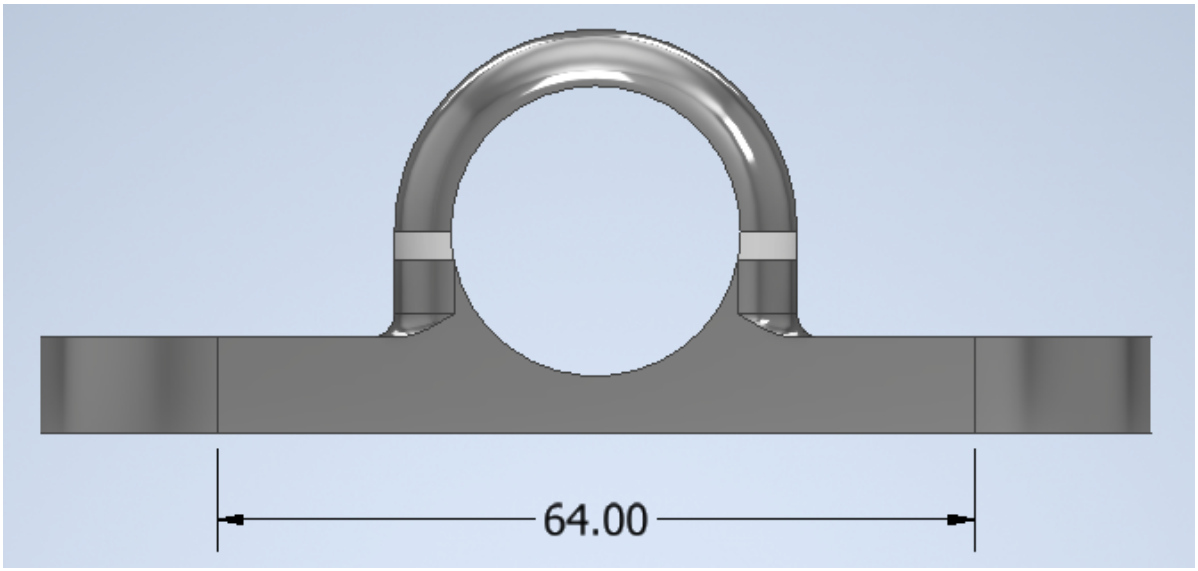


**Figure A.20:** CAD image of the 3D printed mounts for the resistivity sensors. Front view.

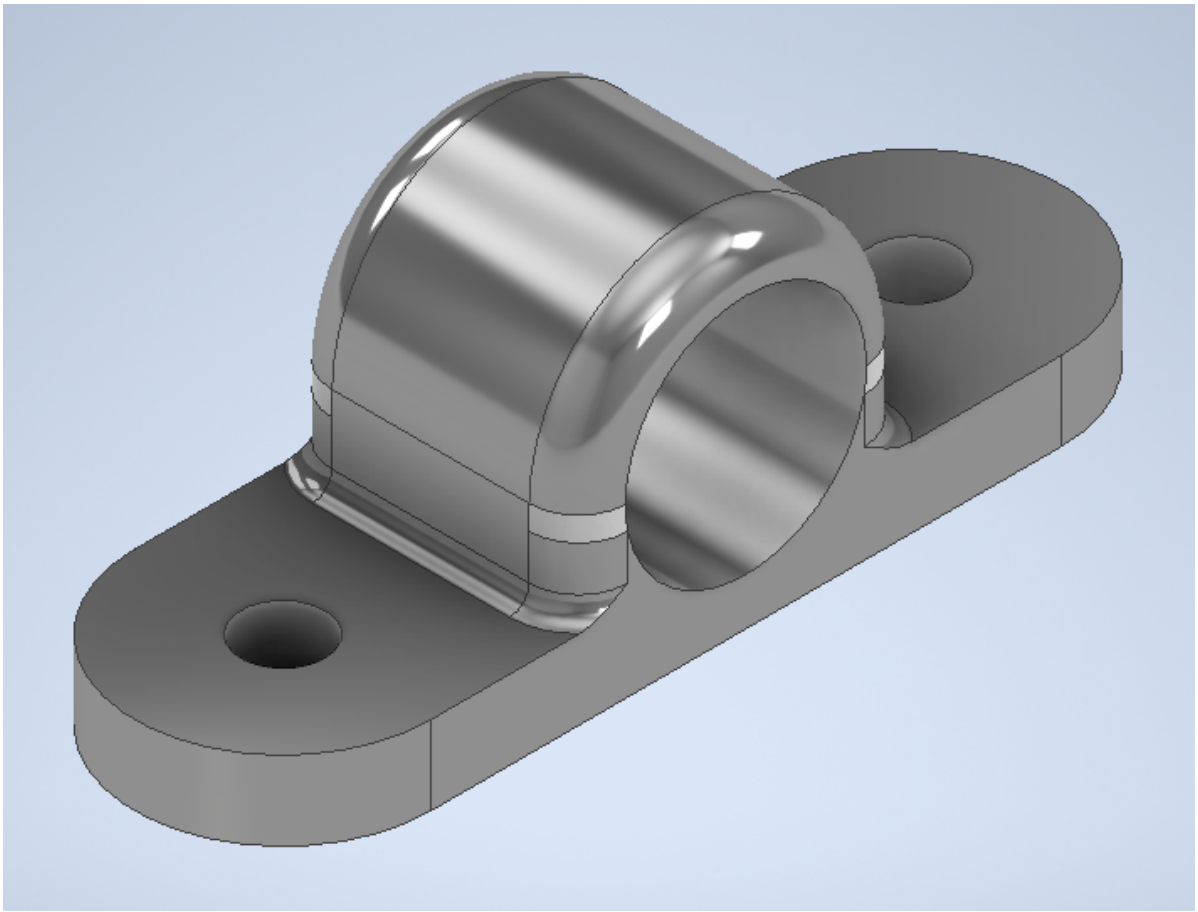

**Figure A.21:** CAD image of the 3D printed mounts for the resistivity sensors. Overview.

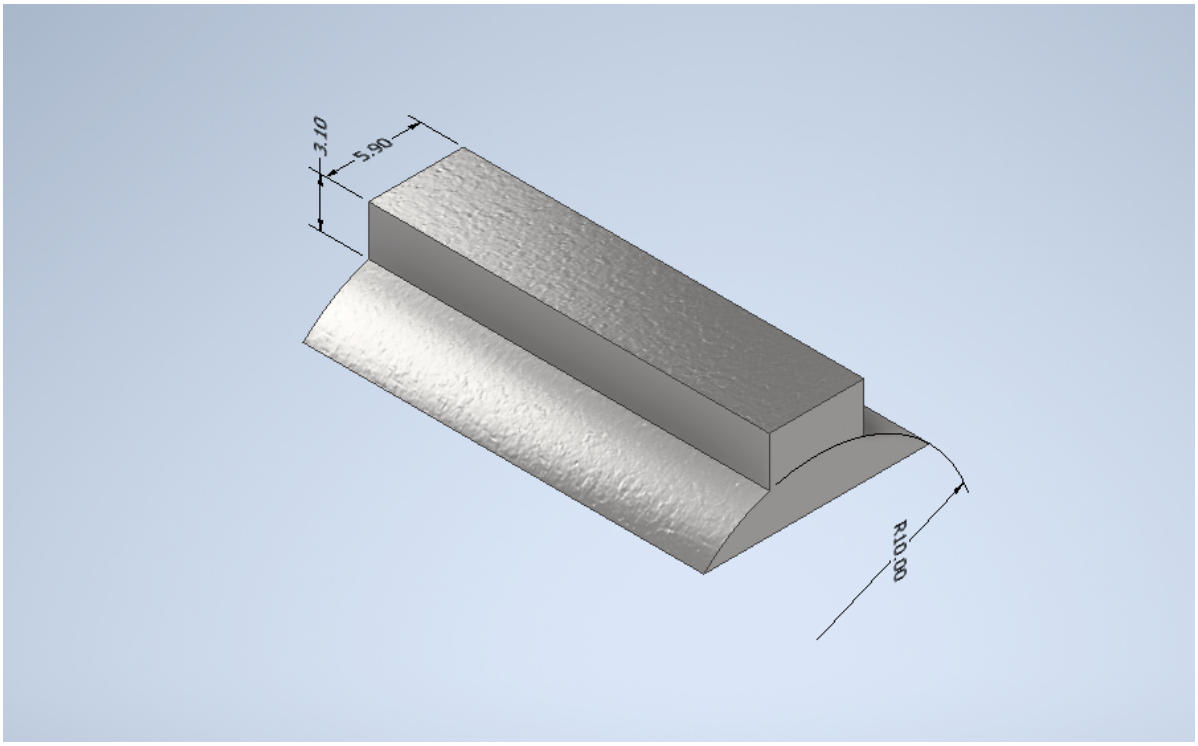


**Figure A.22:** CAD image of key used to mechanically lock axles and gears. Key is press-fit into position.

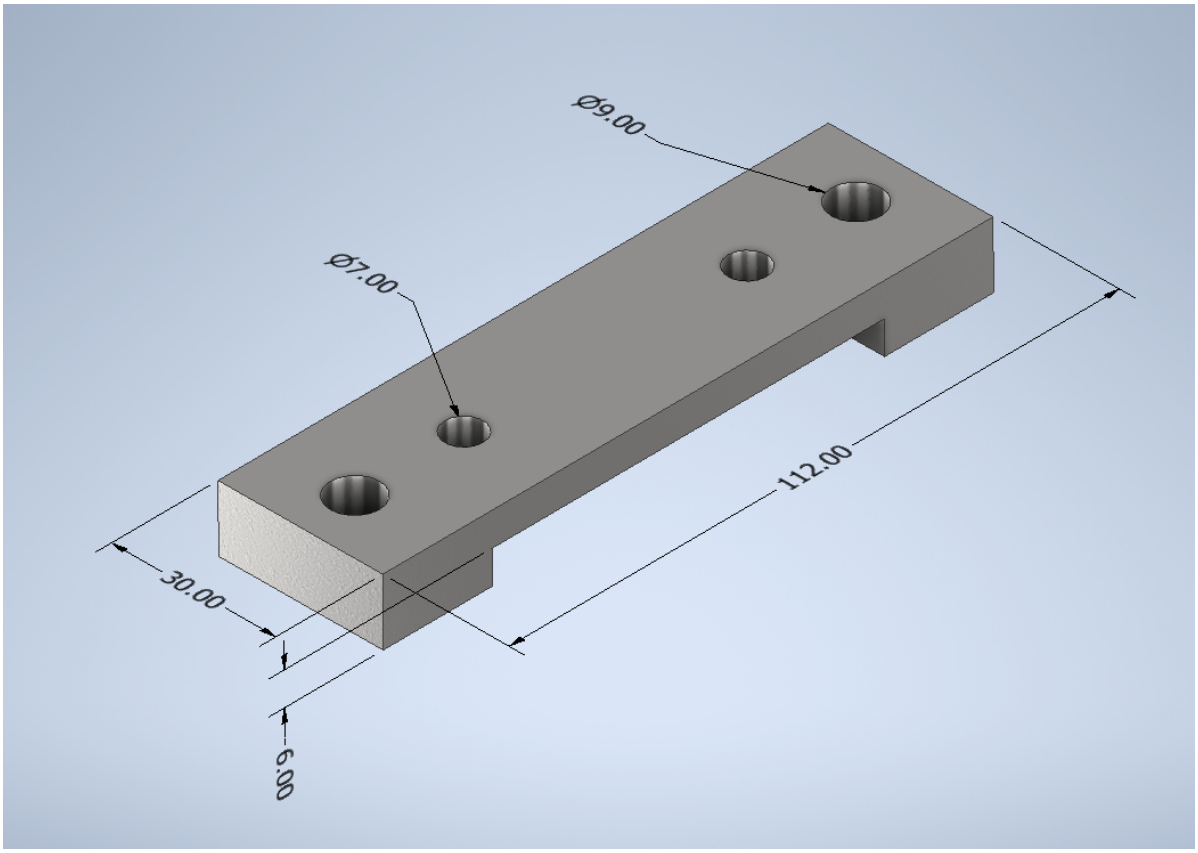


**Figure A.23:** CAD image of 3D printed adapter to convert M8 mounting points to M6 mounting points. Used for occasional integration of old components.

# B

# Code for Capturing and Analysis

## B.1. Motor Drive Script

```
'C++'

// Motor A connections
int enA = 9;
int in1 = 8;
int in2 = 7;


void setup() {
  // Set all the motor control pins to outputs
  pinMode(enA, OUTPUT);
  pinMode(in1, OUTPUT);
  pinMode(in2, OUTPUT);

  // Turn off motors - Initial state
  digitalWrite(in1, LOW);
  digitalWrite(in2, LOW);
}

void loop() {
  directionControl();

}


// Power and direction
void directionControl() {
  // For PWM maximum possible values are 0 to 255
  analogWrite(enA, 140);

  // Turn on motor A
  digitalWrite(in1, HIGH);
  digitalWrite(in2, LOW);

}
```

## B.2. Friction and Resistivity Measurements

```
'Python'

import nidaqmx
import matplotlib.pyplot as plt
import keyboard
import numpy as np
```

```
from datetime import datetime
import sys
import matplotlib
matplotlib.use('TkAgg')

i = 0
x = []
rholist1 = []
rholist2 = []
Flist1 = []
Flist2 = []

I = 0.500 #A
L = 0.125 #m
A = 12000 * 0.25 * np.pi * 0.000007**2
factor1 = 0.2 *10
factor2 = 0.5 *10

plt.ion()
fig, (ax1, ax2) = plt.subplots(2, 1, sharex=True)


# Create a new file for writing data
filename = datetime.now().strftime('%Y-%m-%d_%H-%M-%S')
with open(f'{filename}.txt', 'w') as f:
# with open('output.txt', 'w') as f:
    f.write('Index\tRho1\tRho2\tF1\tF2\n')  # write header row
    index = 0

    with nidaqmx.Task() as task1, nidaqmx.Task() as task2:
        task1.ai_channels.add_ai_voltage_chan("Dev1/ai0:1")
        task2.ai_channels.add_ai_voltage_chan("Dev1/ai2:3", max_val=10)

        while i < 500:
            data1 = task1.read(number_of_samples_per_channel=1)
            data2 = task2.read(number_of_samples_per_channel=1)

            x.append(datetime.now())  # Use current timestamp as x value

            floa1 = float(data1[1][0])
            R1 = floa1 * (1/I)
            rho1 = A*R1/L
            rholist1.append(rho1*1000000)

            floa2 = float(data1[0][0])
            R2 = floa2 * (1/I)
            rho2 = A*R2/L
            rholist2.append(rho2*1000000)

            floa3 = float(data2[1][0])
            F1 = floa3 * factor1
            Flist1.append(F1)

            floa4 = float(data2[0][0])
            F2 = floa4 * factor2
            Flist2.append(F2)

            ax1.plot(x, rholist1, c='b')
            ax1.plot(x, rholist2, c='r')
            ax1.set_ylabel('Effective resistivity [mOhm m]')
            ax1.legend(['One', 'Two'])

            ax2.plot(x, Flist1, c='y')
            ax2.plot(x, Flist2, c='k')
            ax2.set_ylabel('Tension [N]')
            ax2.set_xlabel('Timestamp')
            ax2.legend(['One', 'Two'])

            plt.gcf().autofmt_xdate()  # Format x-axis as dates
            plt.autoscale(enable=True, axis='y')

```

```

            # Write the data to the output file with the current timestamp as the index
            timestamp = datetime.now().strftime('%Y-%m-%d %H:%M:%S.%f')
            f.write(f'{timestamp}\t{rho1:.2f}\t{rho2:.2f}\t{F1:.2f}\t{F2:.2f}\n')


            i += 1
            plt.show()
            plt.pause(0.25)

            # Check for ESC key press and break out of loop
            if keyboard.is_pressed('esc'):
                print('krakaka')
                sys.exit()
                # plt.close(fig)
                # break
```

## B.3. Width Detection

```

'Python'

import cv2
import numpy as np
from datetime import datetime

# initialize video capture from USB cameras
cap1 = cv2.VideoCapture(0)
cap2 = cv2.VideoCapture(1)

# initialize the previous height values for both cameras
prev_h1 = 0
prev_h2 = 0

filename = datetime.now().strftime('%Y-%m-%d_%H-%M-%S')

with open(f'{filename}.txt', 'w') as f1:
# with open('output.txt', 'w') as f:
    f1.write('Index\tTowWidth1\tTowWdith2\n')  # write header row for camera 1

    index = 0

    while True:
        # read frames from the video streams
        ret1, frame1 = cap1.read()
        ret2, frame2 = cap2.read()

        # convert to grayscale
        gray1 = cv2.cvtColor(frame1, cv2.COLOR_BGR2GRAY)
        gray2 = cv2.cvtColor(frame2, cv2.COLOR_BGR2GRAY)

        # apply thresholding to create binary images
        thresh1 = cv2.threshold(gray1, 0, 255, cv2.THRESH_BINARY_INV + cv2.THRESH_OTSU)[1]
        thresh2 = cv2.threshold(gray2, 0, 255, cv2.THRESH_BINARY_INV + cv2.THRESH_OTSU)[1]

        # apply morphological operations to remove noise and smooth the images
        kernel = np.ones((8,8), np.uint8)
        opening1 = cv2.morphologyEx(thresh1, cv2.MORPH_OPEN, kernel, iterations=2)
        closing1 = cv2.morphologyEx(opening1, cv2.MORPH_CLOSE, kernel, iterations=2)

        opening2 = cv2.morphologyEx(thresh2, cv2.MORPH_OPEN, kernel, iterations=2)
        closing2 = cv2.morphologyEx(opening2, cv2.MORPH_CLOSE, kernel, iterations=2)

        # find contours in the images
        contours1, hierarchy1 = cv2.findContours(closing1, cv2.RETR_TREE, cv2.
            CHAIN_APPROX_SIMPLE)
        contours2, hierarchy2 = cv2.findContours(closing2, cv2.RETR_TREE, cv2.
            CHAIN_APPROX_SIMPLE)

```

```
        # find the contour with the largest area for both cameras
        max_area1 = 0
        max_contour1 = None
        for contour in contours1:
            area = cv2.contourArea(contour)
            if area > max_area1:
                max_area1 = area
                max_contour1 = contour

        max_area2 = 0
        max_contour2 = None
        for contour in contours2:
            area = cv2.contourArea(contour)
            if area > max_area2:
                max_area2 = area
                max_contour2 = contour

        # draw the largest contour on the original images for visualization
        cv2.drawContours(frame1, [max_contour1], 0, (0, 255, 0), 2)
        cv2.drawContours(frame2, [max_contour2], 0, (0, 255, 0), 2)


        # find the bounding rectangle of the largest contour
        x1,y1,w1,h1 = cv2.boundingRect(max_contour1)
        x2,y2,w2,h2 = cv2.boundingRect(max_contour2)

        # print the height of the object for camera 2
        print(f"The height of the object for camera 1 is {h1} pixels.")
        print(f"The height of the object for camera 2 is {h2} pixels.")

        # check for gap in measured height sections
        # if abs(h2 - prev_h2) > 5: # adjust the threshold as needed
        #     print("Gap detected for camera 2!")
        #     cv2.putText(frame2, "Gap detected", (200, 30), cv2.FONT_HERSHEY_SIMPLEX, 0.8,
            (0, 0, 255), 2)

        # update the previous height value
        prev_h1 = h1
        prev_h2 = h2

        # Convert the frame to grayscale
        gray1 = cv2.cvtColor(frame1, cv2.COLOR_BGR2GRAY)
        gray2 = cv2.cvtColor(frame2, cv2.COLOR_BGR2GRAY)

        # Convert the image to binary using a threshold
        _, thresh1 = cv2.threshold(gray1, 230, 255, cv2.THRESH_BINARY)
        _, thresh2 = cv2.threshold(gray2, 230, 255, cv2.THRESH_BINARY)

        # Get the horizontal projection of the image
        hist1 = cv2.reduce(thresh1, 1, cv2.REDUCE_AVG)
        hist2 = cv2.reduce(thresh2, 1, cv2.REDUCE_AVG)


        # Smooth the histogram to remove noise
        hist1 = cv2.GaussianBlur(hist1, (5,5), 0)
        hist2 = cv2.GaussianBlur(hist2, (5,5), 0)

        # Find the gaps in the histogram by looking for values below a threshold
        gap_threshold1 = 50
        gaps1 = np.where(hist1 > gap_threshold1)[0]
        gap_threshold2 = 50
        gaps2 = np.where(hist2 > gap_threshold2)[0]

        # Draw the gaps on a separate image with transparency
        gap_image1 = np.zeros_like(frame1)
        for gap1 in gaps1:
            cv2.line(gap_image1, (0, gap1), (frame1.shape[1], gap1), (0, 255, 0), 2)
        gap_image2 = np.zeros_like(frame2)
        for gap2 in gaps2:
            cv2.line(gap_image2, (0, gap2), (frame2.shape[1], gap2), (0, 255, 0), 2)

```

```
        # Add the gap image onto the original frame with alpha blending
        alpha2 = 0.3  # adjust as needed
        alpha1 = 0.3
        cv2.addWeighted(gap_image1, alpha1, frame1, 1 - alpha1, 0, frame1)
        cv2.addWeighted(gap_image2, alpha2, frame2, 1 - alpha2, 0, frame2)

        # display the output image with the height value and gaps marked

        cv2.putText(frame1, f"Height: {h1}", (10, 30), cv2.FONT_HERSHEY_SIMPLEX, 0.8, (255,0,
            0), 2)
        cv2.putText(frame2, f"Height: {h2}", (10, 30), cv2.FONT_HERSHEY_SIMPLEX, 0.8, (255,0,
            0), 2)

        cv2.imshow('Output', np.hstack((frame1, frame2)))


        # Write the data to the output file with the current timestamp as the index
        timestamp = datetime.now().strftime('%Y-%m-%d %H:%M:%S.%f')
        f1.write(f'{timestamp}\t{h1:.2f}\t{h2:.2f}\n')


        # exit on ESC key press
        if cv2.waitKey(1) == 27:
            break

cap1.release()
cap2.release()
cv2.destroyAllWindows()
```

## B.4. Directional Detection

```

'Python'

# -*- coding: utf-8 -*-

import cv2
import numpy as np
from datetime import datetime

# Initialize the webcams
cap1 = cv2.VideoCapture(0)
cap2 = cv2.VideoCapture(1)

# Loop over frames from the webcams

filename = datetime.now().strftime('%Y-%m-%d_%H-%M-%S')
with open(f'{filename}.txt', 'w') as f:
    f.write('Index\tAvg. Angle1\tStd. Dev1.\tAvg. Angle2\tStd. Dev2.\n')  # write header row
    index = 0

    while True:
        # Capture frames from the webcams
        ret1, frame1 = cap1.read()
        ret2, frame2 = cap2.read()

        # Convert the frames to grayscale
        gray1 = cv2.cvtColor(frame1, cv2.COLOR_BGR2GRAY)
        gray2 = cv2.cvtColor(frame2, cv2.COLOR_BGR2GRAY)

        # Apply Gaussian blur to remove noise
        gray1 = cv2.GaussianBlur(gray1, (3, 3), 0)
        gray2 = cv2.GaussianBlur(gray2, (3, 3), 0)

        # Set the sensitivity of the line detection
        sensitivity = 20000

        # Apply Canny edge detection to detect edges
        edges1 = cv2.Canny(gray1, sensitivity, sensitivity * 3, apertureSize=7)
```

```
        edges2 = cv2.Canny(gray2, sensitivity, sensitivity * 3, apertureSize=7)

        # Dilate the edges to thicken the lines
        kernel = np.ones((3, 3), np.uint8)
        edges1 = cv2.dilate(edges1, kernel, iterations=1)
        edges2 = cv2.dilate(edges2, kernel, iterations=1)

        # Find contours in the binary images
        contours1, hierarchy1 = cv2.findContours(edges1, cv2.RETR_TREE, cv2.
            CHAIN_APPROX_SIMPLE)
        contours2, hierarchy2 = cv2.findContours(edges2, cv2.RETR_TREE, cv2.
            CHAIN_APPROX_SIMPLE)

        # Initialize variables for computing the average angle
        angles1 = []
        angles2 = []

        # Loop through each contour and fit a line to it
        for contour in contours1:
            # Fit a line to the contour using the least squares method
            [vx, vy, x, y] = cv2.fitLine(contour, cv2.DIST_L2, 0, 0.01, 0.01)

            # Compute the angle of the line with respect to the horizontal axis
            angle = np.arctan2(vy, vx) * 180 / np.pi

            # Adjust the angle if it is outside the range [0, 180]
            if angle > 180:
                angle -= 180

            # Add the angle to the list
            angles1.append(angle)

            # Draw the line on the image with the corresponding color
            thickness = 1
            pt1 = (int(x - 100 * vx), int(y - 100 * vy))
            pt2 = (int(x + 100 * vx), int(y + 100 * vy))
            cv2.line(frame1, pt1, pt2, (255, 0, 255), thickness)




        for contour in contours2:
            # Fit a line to the contour using the least squares method
            [vx, vy, x, y] = cv2.fitLine(contour, cv2.DIST_L2, 0, 0.01, 0.01)

            # Compute the angle of the line with respect to the horizontal axis
            angle = np.arctan2(vy, vx) * 180 / np.pi

            # Adjust the angle if it is outside the range [0, 180]
            if angle > 180:
                angle -= 180

            # Add the angle to the list and sum it
            angles2.append(angle)

            # Draw the line on the image with the corresponding color
            thickness = 1
            pt1 = (int(x - 100 * vx), int(y - 100 * vy))
            pt2 = (int(x + 100 * vx), int(y + 100 * vy))
            cv2.line(frame2, pt1, pt2, (255, 0, 255), thickness)

        # Compute the average angle and std
        if len(angles1) > 0:
            avg_angle1 = np.mean(angles1)
            std_angle1 = np.std(angles1)

            # Display the average angle as text on the image
            cv2.putText(frame1, f"Avg. Angle: {avg_angle1:.2f}", (50, 50), cv2.
                FONT_HERSHEY_SIMPLEX, 1, (255, 0, 255), 2)
            cv2.putText(frame1, f"Std. Dev.: {std_angle1:.2f}", (50, 100), cv2.
```

```
                FONT_HERSHEY_SIMPLEX, 1, (255, 0, 255), 2)


        if len(angles2) > 0:
            avg_angle2 = np.mean(angles2)
            std_angle2 = np.std(angles2)

            # Display the average angle as text on the image
            cv2.putText(frame2, f"Avg. Angle: {avg_angle2:.2f}", (50, 50), cv2.
                FONT_HERSHEY_SIMPLEX, 1, (255, 0, 255), 2)
            cv2.putText(frame2, f"Std. Dev.: {std_angle2:.2f}", (50, 100), cv2.
                FONT_HERSHEY_SIMPLEX, 1, (255, 0, 255), 2)

            # Write the data to the output file with the current timestamp as the index
            timestamp = datetime.now().strftime('%Y-%m-%d %H:%M:%S.%f')
            f.write(f'{timestamp}\t{avg_angle1:.2f}\t{std_angle1:.2f}\t{avg_angle2:.2f}\t{
                std_angle2:.2f}\n')

        # Show the output in real-time for both cameras
        cv2.imshow('Output', np.hstack((frame1, frame2)))

        # Wait for a key press to exit
        if cv2.waitKey(1) == ord('q'):
            break

    # Release the webcams and close all windows
    cap1.release()
    cap2.release()
    cv2.destroyAllWindows()
```

## B.5. Data Processing

```


# -*- coding: utf-8 -*-

'Python'
'General file used for reading the output .txt files'

import pandas as pd
import matplotlib.pyplot as plt

# Load the data into a pandas DataFrame
df = pd.read_csv('2023-04-11_19-25-48.txt', delimiter='\t', header=0, names=['index', 'avg1',
     'std1', 'avg2', 'std2'])

# Plot the first column (value) against the index column
plt.plot(df['index'], df['std1'])
plt.xlabel('Index')
plt.ylabel('Value')
plt.show()
```

```

'Python'
'Code to quickly process values for multiple .txt files at once'

import csv
import glob
import os

directories = ['140speed60wrap1pretension']

for directory in directories:
    for filename in glob.glob(directory + '/**/*.txt', recursive=True):
        with open(filename, 'r') as file:
            reader = csv.reader(file, delimiter='\t')
            data = [[] for _ in range(5)]
            for row in reader:
                for i in range(5):
```

```
                    try:
                        data[i].append(float(row[i]))
                    except ValueError:
                        # Ignore non-numeric values
                        pass
            averages = [sum(column) / len(column) if column else 0 for column in data]
            output_filename = os.path.splitext(filename)[0] + '_averages.csv'
            with open(output_filename, 'w', newline='') as output_file:
                writer = csv.writer(output_file)
                writer.writerow(['Column', 'Average'])
                for i, average in enumerate(averages):
                    writer.writerow([i+1, average])
```

# C

# Experimental Output

## C.1. Friction Behaviour

```
Dataset W40_T1_V140: y = 0.0139x^2 + -0.1136x + 1.5517
Dataset W40_T1_V200: y = 0.0169x^2 + -0.1323x + 1.5808
Dataset W40_T1_V255: y = 0.0134x^2 + -0.1129x + 1.5431
Dataset W40_T2_V140: y = 0.0196x^2 + -0.1491x + 1.5943
Dataset W40_T2_V200: y = 0.0085x^2 + -0.0838x + 1.4932
Dataset W40_T2_V255: y = 0.0132x^2 + -0.1168x + 1.5591
Dataset W40_T3_V140: y = 0.0068x^2 + -0.0730x + 1.4656
Dataset W40_T3_V200: y = 0.0081x^2 + -0.0761x + 1.4584
Dataset W40_T3_V255: y = 0.0040x^2 + -0.0468x + 1.4053
Dataset W40_T4_V140: y = 0.0060x^2 + -0.0678x + 1.4487
Dataset W40_T4_V200: y = 0.0083x^2 + -0.0814x + 1.4661
Dataset W40_T4_V255: y = 0.0067x^2 + -0.0722x + 1.4659
Dataset W40_T5_V140: y = 0.0097x^2 + -0.0918x + 1.4790
Dataset W40_T5_V200: y = 0.0091x^2 + -0.0846x + 1.4676
Dataset W40_T5_V255: y = 0.0132x^2 + -0.1185x + 1.5335
Dataset W80_T1_V140: y = 0.0433x^2 + -0.3302x + 2.2910
Dataset W80_T1_V200: y = 0.0360x^2 + -0.2844x + 2.1799
Dataset W80_T1_V255: y = 0.0479x^2 + -0.3473x + 2.2645
Dataset W80_T2_V140: y = 0.0493x^2 + -0.3590x + 2.2528
Dataset W80_T2_V200: y = 0.0218x^2 + -0.1960x + 2.0185
Dataset W80_T2_V255: y = 0.0332x^2 + -0.2783x + 2.1856
Dataset W80_T3_V140: y = 0.0310x^2 + -0.2558x + 2.1203
Dataset W80_T3_V200: y = 0.0158x^2 + -0.1630x + 2.0333
Dataset W80_T3_V255: y = 0.0259x^2 + -0.2370x + 2.1409
Dataset W80_T4_V140: y = 0.0229x^2 + -0.2124x + 2.0794
Dataset W80_T4_V200: y = 0.0287x^2 + -0.2449x + 2.1187
Dataset W80_T4_V255: y = 0.0245x^2 + -0.2311x + 2.1533
Dataset W80_T5_V140: y = 0.0233x^2 + -0.2072x + 2.0420
Dataset W80_T5_V200: y = 0.0261x^2 + -0.2403x + 2.1372
Dataset W80_T5_V255: y = 0.0168x^2 + -0.1660x + 1.9867
Dataset W115_T1_V140: y = 0.0753x^2 + -0.5347x + 2.8570
Dataset W115_T1_V200: y = 0.0537x^2 + -0.4313x + 2.8302
Dataset W115_T1_V255: y = 0.0335x^2 + -0.3090x + 2.5885
Dataset W115_T2_V140: y = 0.0455x^2 + -0.3658x + 2.6060
Dataset W115_T2_V200: y = 0.0422x^2 + -0.3585x + 2.6364
Dataset W115_T2_V255: y = 0.0568x^2 + -0.4441x + 2.7946
Dataset W115_T3_V140: y = 0.0420x^2 + -0.3543x + 2.7065
Dataset W115_T3_V200: y = 0.0247x^2 + -0.2589x + 2.5152
Dataset W115_T3_V255: y = 0.0740x^2 + -0.5671x + 2.9974
Dataset W115_T4_V140: y = 0.0784x^2 + -0.5838x + 3.0653
Dataset W115_T4_V200: y = 0.0452x^2 + -0.4154x + 3.1069
Dataset W115_T4_V255: y = 0.0335x^2 + -0.3144x + 2.7081
Dataset W115_T5_V140: y = 0.0361x^2 + -0.3308x + 2.6909
Dataset W115_T5_V200: y = 0.0269x^2 + -0.2699x + 2.6410
Dataset W115_T5_V255: y = 0.0375x^2 + -0.3643x + 2.9221
Dataset W150_T1_V140: y = 0.0864x^2 + -0.6140x + 3.2620
Dataset W150_T1_V200: y = 0.0638x^2 + -0.5224x + 3.2400
Dataset W150_T1_V255: y = 0.0725x^2 + -0.5726x + 3.3539
Dataset W150_T2_V140: y = 0.1561x^2 + -0.9883x + 3.7789
Dataset W150_T2_V200: y = 0.0507x^2 + -0.4658x + 3.3714
Dataset W150_T2_V255: y = 0.0554x^2 + -0.4891x + 3.3163
Dataset W150_T3_V140: y = 0.0574x^2 + -0.4709x + 3.1350
Dataset W150_T3_V200: y = 0.0401x^2 + -0.3778x + 3.0199
Dataset W150_T3_V255: y = 0.0466x^2 + -0.4231x + 3.1558
Dataset W150_T4_V140: y = 0.1066x^2 + -0.8159x + 4.0289
Dataset W150_T4_V200: y = 0.0545x^2 + -0.5158x + 3.6837
Dataset W150_T4_V255: y = 0.0369x^2 + -0.4193x + 3.5532
Dataset W150_T5_V140: y = 0.0737x^2 + -0.6088x + 3.5415
Dataset W150_T5_V200: y = 0.0467x^2 + -0.4703x + 3.6326
Dataset W150_T5_V255: y = 0.0709x^2 + -0.6281x + 3.8410
Dataset W170_T1_V140: y = 0.1035x^2 + -0.7782x + 4.2233
Dataset W170_T1_V200: y = 0.1080x^2 + -0.8268x + 4.4307
Dataset W170_T1_V255: y = 0.0842x^2 + -0.6949x + 4.1334
Dataset W170_T2_V140: y = 0.0809x^2 + -0.6661x + 4.0803
Dataset W170_T2_V200: y = 0.0985x^2 + -0.7576x + 4.1754
Dataset W170_T2_V255: y = 0.0454x^2 + -0.4564x + 3.6989
Dataset W170_T3_V140: y = 0.0686x^2 + -0.5990x + 3.8813
Dataset W170_T3_V200: y = 0.0566x^2 + -0.5295x + 3.8007
Dataset W170_T3_V255: y = 0.0398x^2 + -0.4174x + 3.6359
Dataset W170_T4_V140: y = 0.0865x^2 + -0.6913x + 3.9246
Dataset W170_T4_V200: y = 0.0415x^2 + -0.4166x + 3.5982
Dataset W170_T4_V255: y = 0.0612x^2 + -0.5524x + 3.8589
Dataset W170_T5_V140: y = 0.0406x^2 + -0.4066x + 3.5272
Dataset W170_T5_V200: y = 0.0497x^2 + -0.4754x + 3.6607
Dataset W170_T5_V255: y = 0.0327x^2 + -0.3544x + 3.5241
```

**(a)** Without resistivity sensors installed.

```
Dataset W40_T1_P140: y = 0.0117x^2 + -0.0882x + 1.4479
Dataset W40_T1_P200: y = 0.0146x^2 + -0.1073x + 1.4849
Dataset W40_T1_P255: y = 0.0081x^2 + -0.0757x + 1.4734
Dataset W40_T2_P140: y = 0.0230x^2 + -0.1618x + 1.5842
Dataset W40_T2_P200: y = 0.0007x^2 + -0.0284x + 1.3684
Dataset W40_T2_P255: y = 0.0057x^2 + -0.0608x + 1.4456
Dataset W40_T3_P140: y = 0.0178x^2 + -0.1329x + 1.5508
Dataset W40_T3_P200: y = 0.0069x^2 + -0.0684x + 1.4517
Dataset W40_T3_P255: y = 0.0076x^2 + -0.0704x + 1.4674
Dataset W40_T4_P140: y = 0.0030x^2 + -0.0380x + 1.3761
Dataset W40_T4_P200: y = 0.0025x^2 + -0.0338x + 1.3928
Dataset W40_T4_P255: y = 0.0073x^2 + -0.0709x + 1.4635
Dataset W40_T5_P140: y = 0.0135x^2 + -0.1148x + 1.5191
Dataset W40_T5_P200: y = -0.0016x^2 + -0.0031x + 1.3255
Dataset W40_T5_P255: y = 0.0013x^2 + -0.0228x + 1.3644
Dataset W80_T1_P140: y = 0.0544x^2 + -0.4022x + 2.4888
Dataset W80_T1_P200: y = 0.0393x^2 + -0.3016x + 2.2501
Dataset W80_T1_P255: y = 0.0173x^2 + -0.1927x + 2.1498
Dataset W80_T2_P140: y = 0.0172x^2 + -0.1754x + 2.0428
Dataset W80_T2_P200: y = 0.0263x^2 + -0.2268x + 2.0957
Dataset W80_T2_P255: y = 0.0266x^2 + -0.2300x + 2.0947
Dataset W80_T3_P140: y = 0.0232x^2 + -0.2023x + 2.0120
Dataset W80_T3_P200: y = 0.0188x^2 + -0.1839x + 2.0108
Dataset W80_T3_P255: y = 0.0223x^2 + -0.2275x + 2.2278
Dataset W80_T4_P140: y = 0.0060x^2 + -0.1042x + 1.9940
Dataset W80_T4_P200: y = 0.0103x^2 + -0.1225x + 1.9467
Dataset W80_T4_P255: y = 0.0202x^2 + -0.1982x + 2.0624
Dataset W80_T5_P140: y = 0.0144x^2 + -0.1512x + 1.9367
Dataset W80_T5_P200: y = 0.0147x^2 + -0.1508x + 1.9323
Dataset W80_T5_P255: y = 0.0130x^2 + -0.1437x + 1.9432
Dataset W115_T1_P140: y = 0.0645x^2 + -0.4813x + 2.8984
Dataset W115_T1_P200: y = 0.0456x^2 + -0.3928x + 2.8738
Dataset W115_T1_P255: y = 0.0602x^2 + -0.4684x + 2.9325
Dataset W115_T2_P140: y = 0.0728x^2 + -0.5483x + 3.1423
Dataset W115_T2_P200: y = 0.0450x^2 + -0.4119x + 3.0206
Dataset W115_T2_P255: y = 0.0567x^2 + -0.4529x + 2.9722
Dataset W115_T3_P140: y = 0.0639x^2 + -0.4971x + 2.8947
Dataset W115_T3_P200: y = 0.0466x^2 + -0.3862x + 2.7819
Dataset W115_T3_P255: y = 0.0269x^2 + -0.2676x + 2.5368
Dataset W115_T4_P140: y = 0.0259x^2 + -0.2509x + 2.4636
Dataset W115_T4_P200: y = 0.0287x^2 + -0.2796x + 2.5501
Dataset W115_T4_P255: y = 0.0109x^2 + -0.1694x + 2.4432
Dataset W115_T5_P140: y = 0.0449x^2 + -0.4046x + 2.9233
Dataset W115_T5_P200: y = 0.0170x^2 + -0.2061x + 2.5642
Dataset W115_T5_P255: y = 0.0226x^2 + -0.2448x + 2.6732
Dataset W150_T1_P140: y = 0.0812x^2 + -0.6216x + 3.5565
Dataset W150_T1_P200: y = 0.0849x^2 + -0.6382x + 3.6249
Dataset W150_T1_P255: y = 0.0721x^2 + -0.5800x + 3.5295
Dataset W150_T2_P140: y = 0.0869x^2 + -0.6383x + 3.5315
Dataset W150_T2_P200: y = 0.0529x^2 + -0.4742x + 3.3489
Dataset W150_T2_P255: y = 0.0413x^2 + -0.4049x + 3.2818
Dataset W150_T3_P140: y = 0.0522x^2 + -0.4684x + 3.2855
Dataset W150_T3_P200: y = 0.0426x^2 + -0.3970x + 3.1825
Dataset W150_T3_P255: y = 0.0519x^2 + -0.4657x + 3.3491
Dataset W150_T4_P140: y = 0.0697x^2 + -0.5695x + 3.3952
Dataset W150_T4_P200: y = 0.0357x^2 + -0.3491x + 3.0973
Dataset W150_T4_P255: y = 0.0528x^2 + -0.4741x + 3.3207
Dataset W150_T5_P140: y = 0.0412x^2 + -0.3816x + 3.0723
Dataset W150_T5_P200: y = 0.0308x^2 + -0.3285x + 3.0905
Dataset W150_T5_P255: y = 0.0428x^2 + -0.4107x + 3.2213
Dataset W170_T1_P140: y = 0.0869x^2 + -0.6645x + 3.8228
Dataset W170_T1_P200: y = 0.1341x^2 + -0.9220x + 4.2738
Dataset W170_T1_P255: y = 0.0774x^2 + -0.6327x + 3.9305
Dataset W170_T2_P140: y = 0.0981x^2 + -0.7421x + 4.0430
Dataset W170_T2_P200: y = 0.0673x^2 + -0.5655x + 3.6937
Dataset W170_T2_P255: y = 0.0522x^2 + -0.5032x + 3.8865
Dataset W170_T3_P140: y = 0.0765x^2 + -0.6362x + 3.8834
Dataset W170_T3_P200: y = 0.0709x^2 + -0.6041x + 3.7818
Dataset W170_T3_P255: y = 0.0657x^2 + -0.5688x + 3.7376
Dataset W170_T4_P140: y = 0.0667x^2 + -0.5768x + 3.6829
Dataset W170_T4_P200: y = 0.0470x^2 + -0.4509x + 3.5604
Dataset W170_T4_P255: y = 0.0506x^2 + -0.4854x + 3.8121
Dataset W170_T5_P140: y = 0.0529x^2 + -0.4957x + 3.6616
Dataset W170_T5_P200: y = 0.0290x^2 + -0.3291x + 3.3624
Dataset W170_T5_P255: y = 0.0230x^2 + -0.2804x + 3.2745
```

**(b)** With resistivity sensors installed.

**Figure C.1:** Fitting parameters for friction behaviour

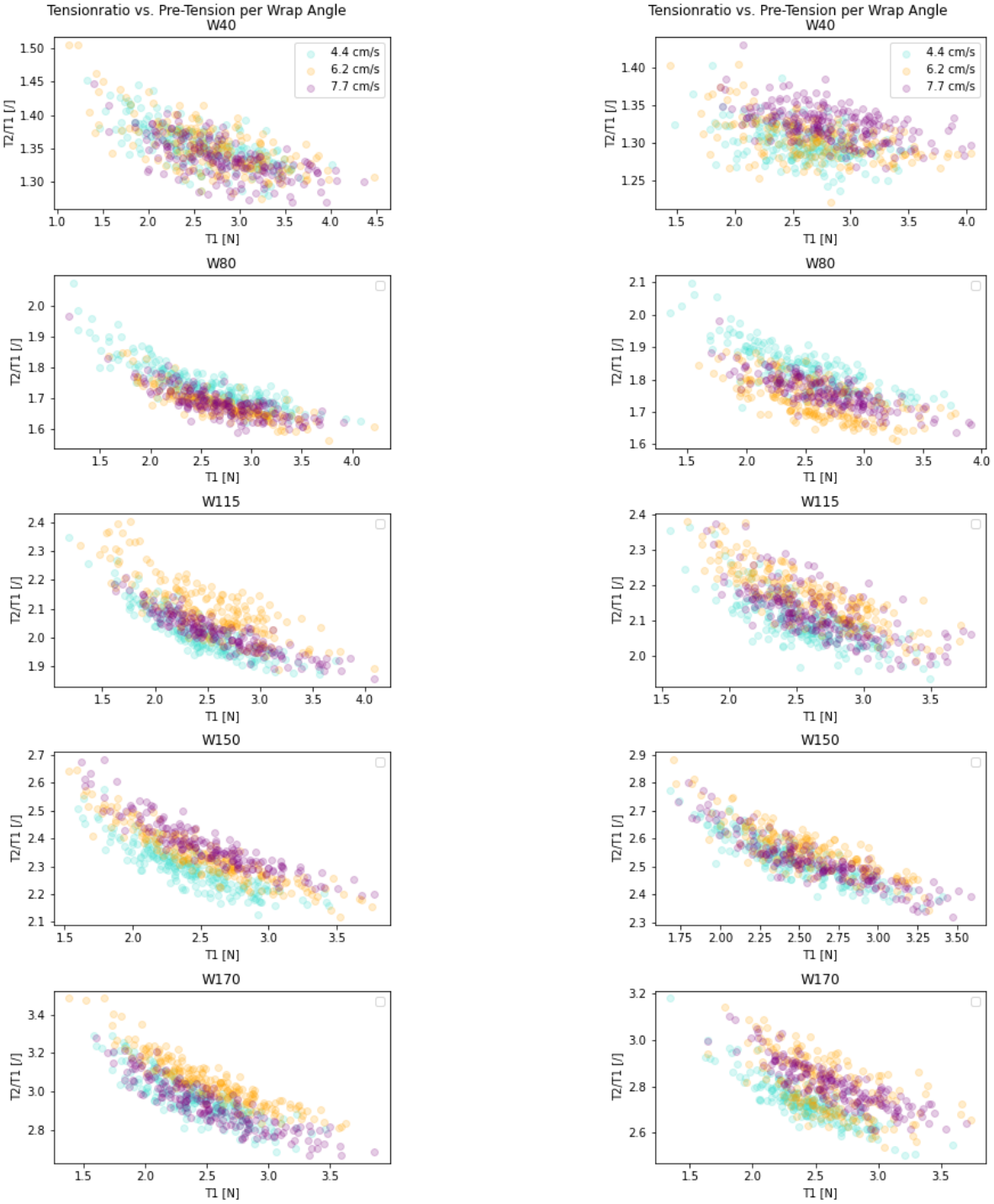


**(a)** Without resistivity sensors installed.

**(b)** With resistivity sensors installed.

**Figure C.2:** Influence of relative velocity on spreading friction behaviour. Pre-tension setting = 1/5.

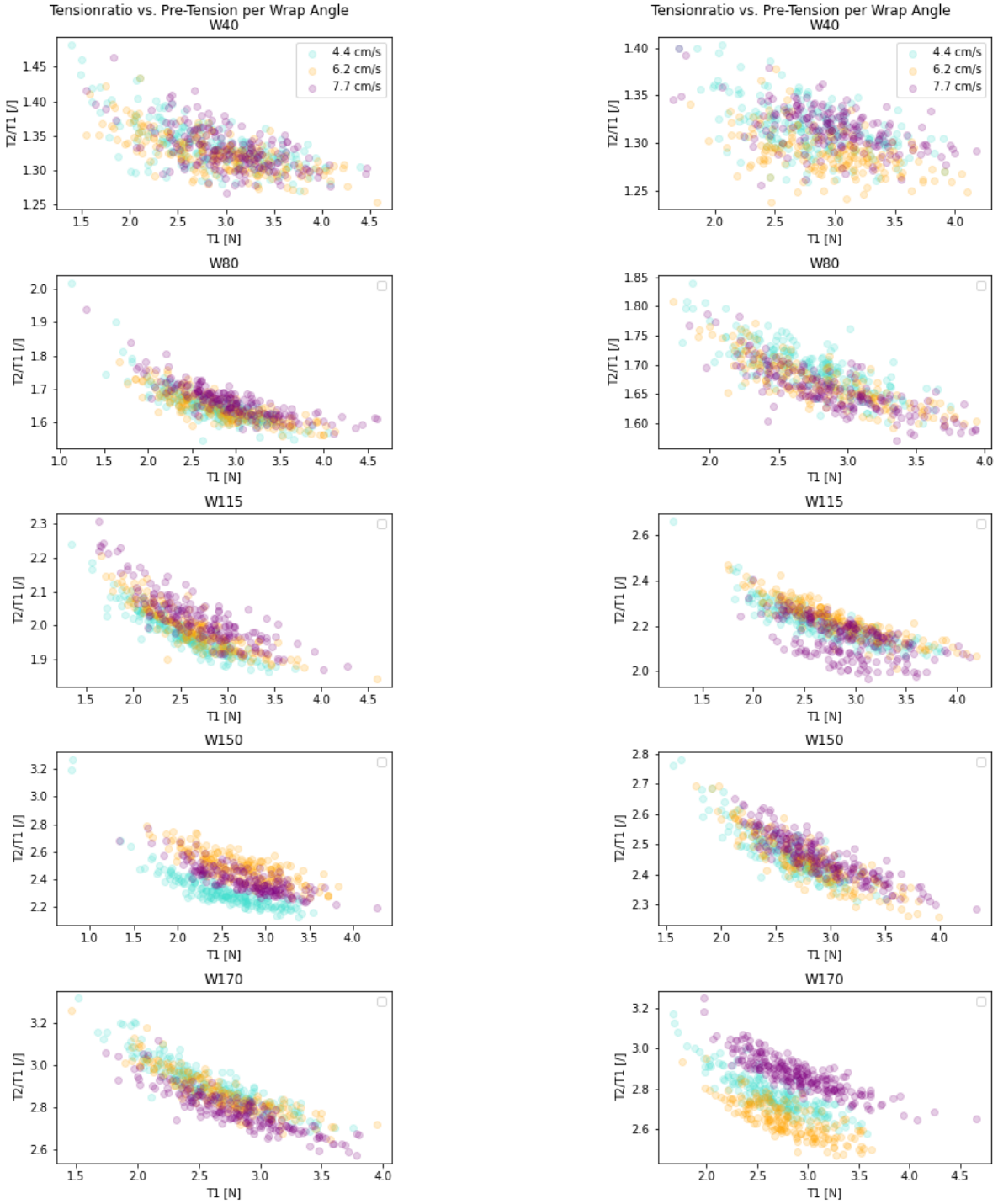


**(a)** Without resistivity sensors installed.

**(b)** With resistivity sensors installed.

**Figure C.3:** Influence of relative velocity on spreading friction behaviour. Pre-tension setting = 2/5.

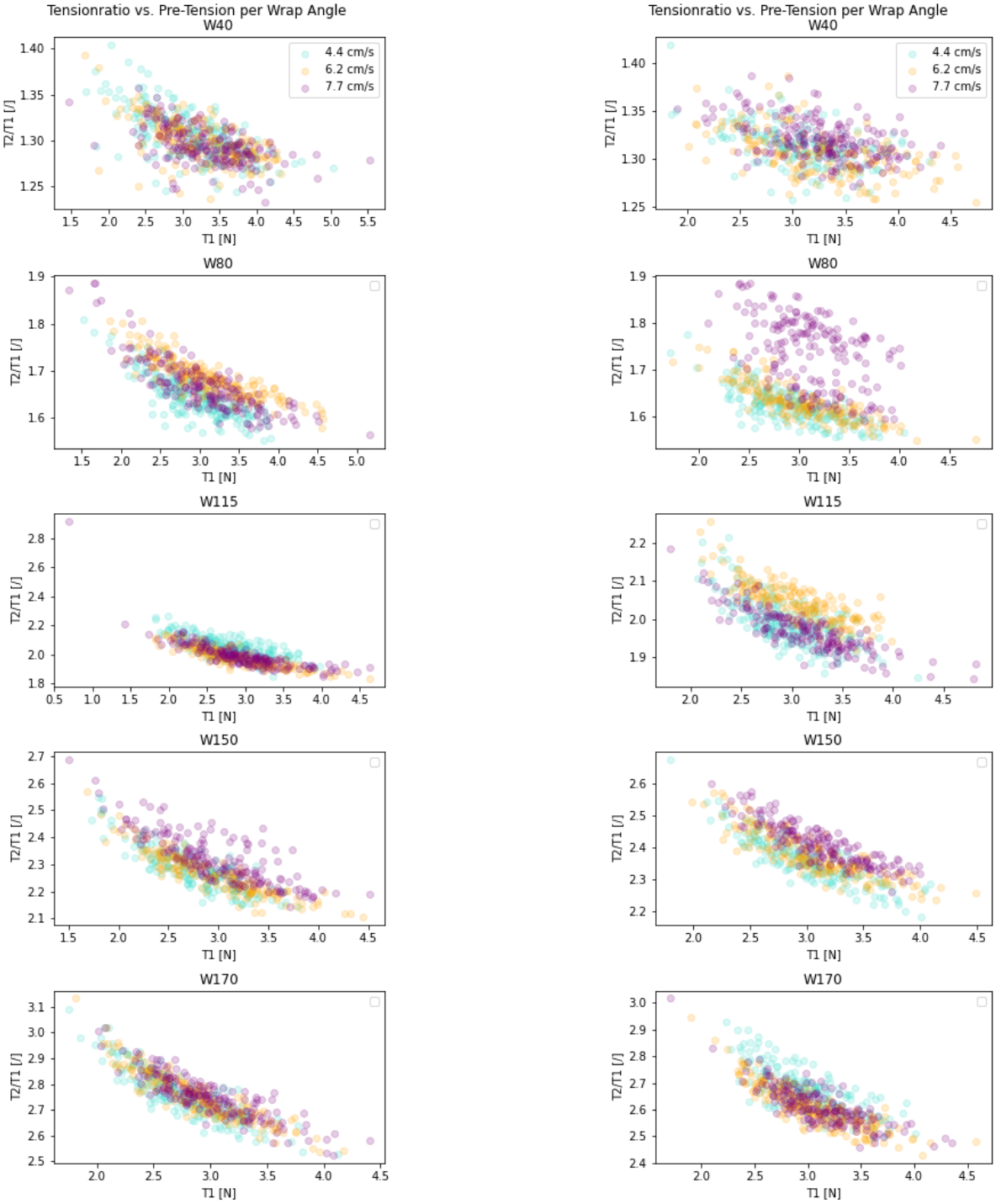


**(a)** Without resistivity sensors installed.

**(b)** With resistivity sensors installed.

**Figure C.4:** Influence of relative velocity on spreading friction behaviour. Pre-tension setting = 3/5.

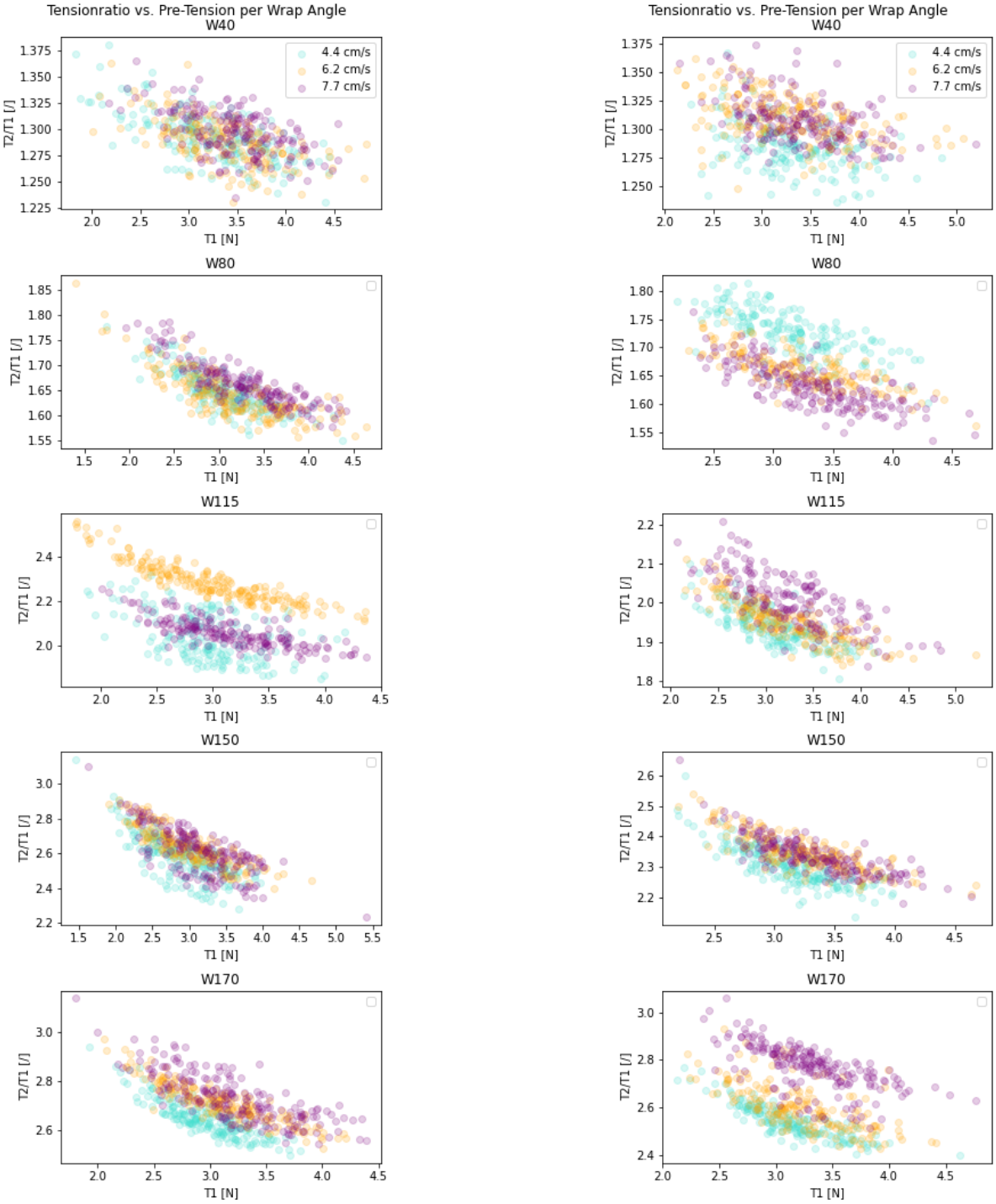


**(a)** Without resistivity sensors installed.

**(b)** With resistivity sensors installed.

**Figure C.5:** Influence of relative velocity on spreading friction behaviour. Pre-tension setting = 4/5.

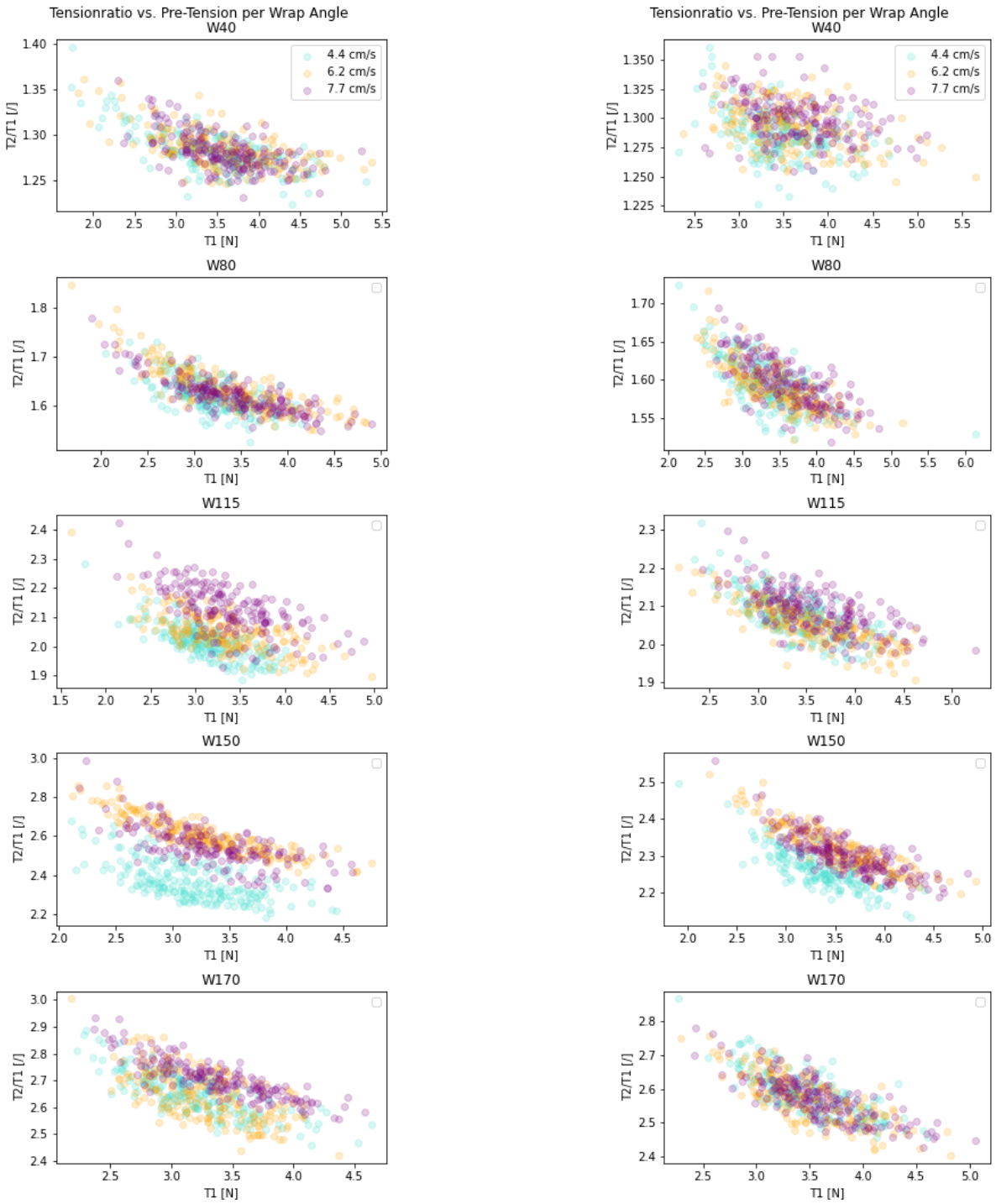


**(a)** Without resistivity sensors installed.

**(b)** With resistivity sensors installed.

**Figure C.6:** Influence of relative velocity on spreading friction behaviour. Pre-tension setting = 5/5.

## C.2. Resistivity Measurements

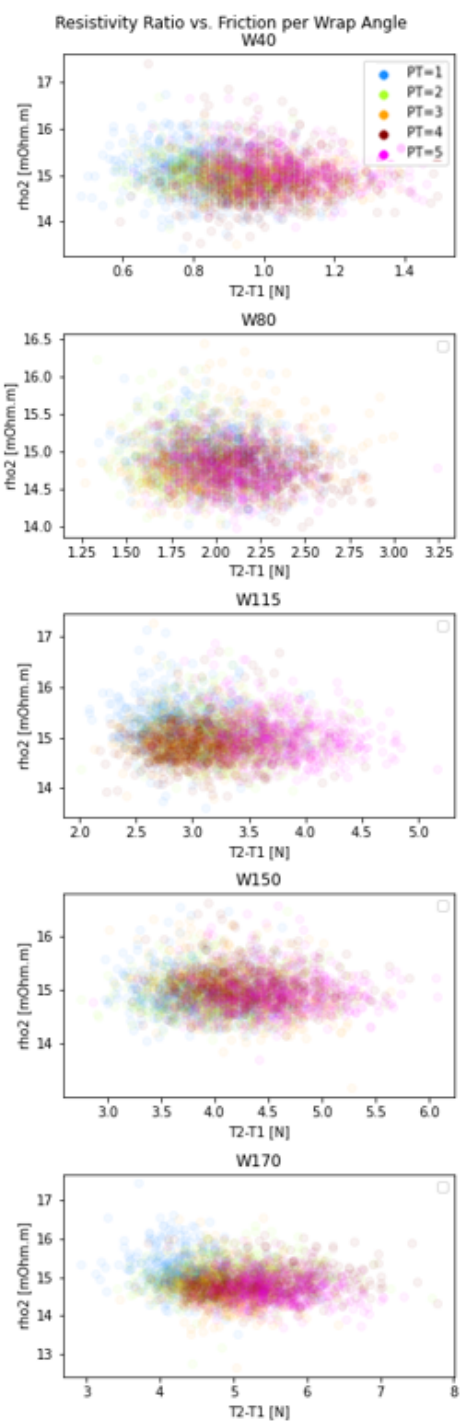


**(a)** Resistivity measurements for sensor 1.

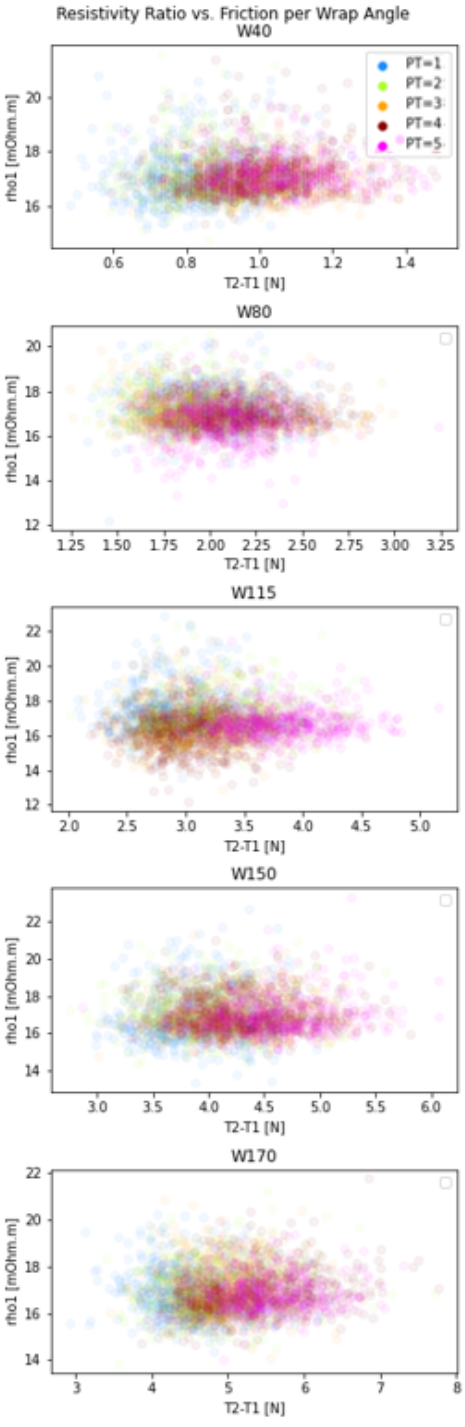


**(b)** Resistivity measurements for sensor 2.

**Figure C.7:** Overview of resistivity measurement results sorted by their related pre-tension brake value, per wrap angle per sensor.

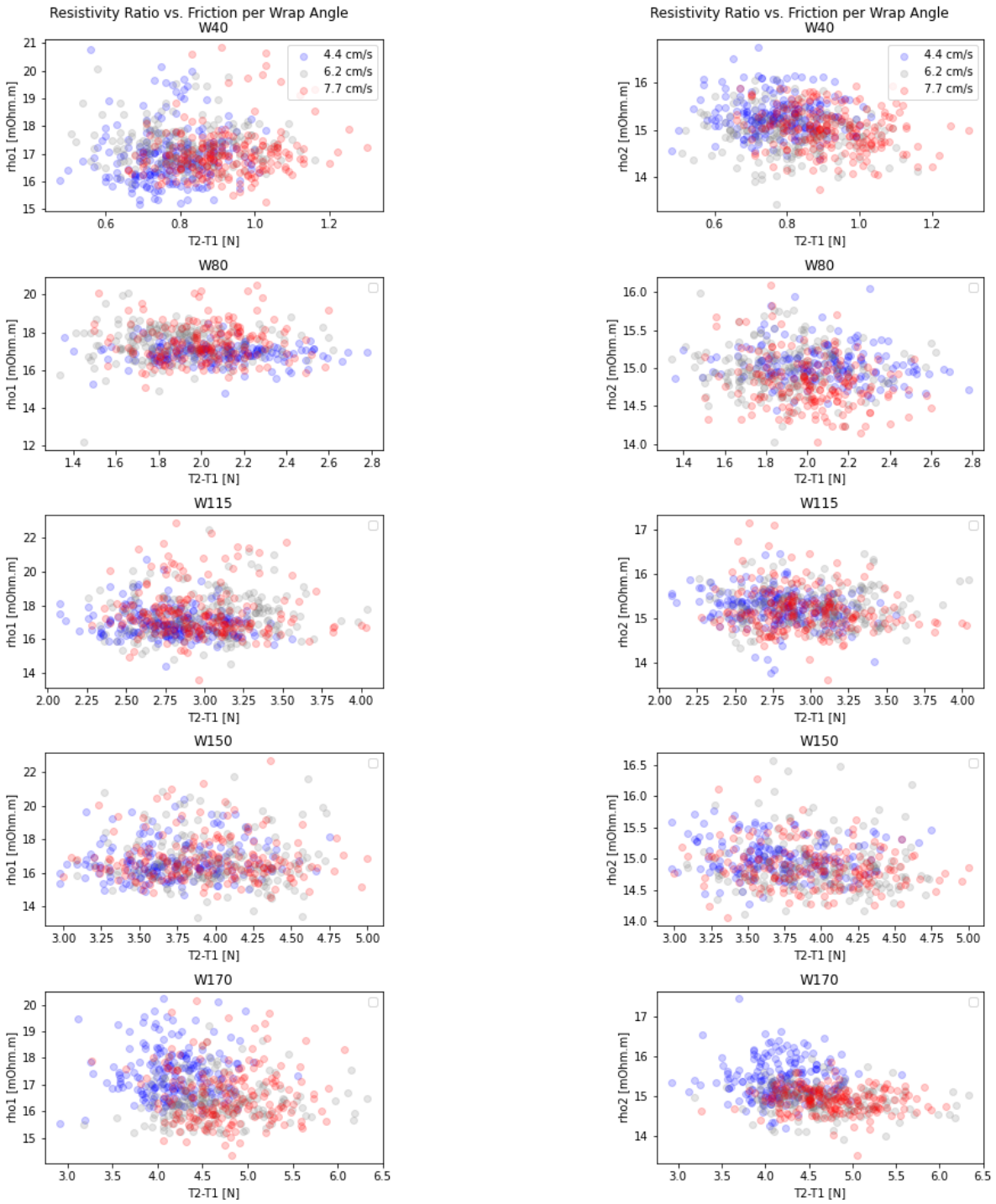


**(a)** Resistivity measurements for sensor 1.

**(b)** Resistivity measurements for sensor 2.

**Figure C.8:** Overview of resistivity measurement results sorted by their related pulling speed, per wrap angle per sensor. Mechanical brake pre-tension at setting 1/5.

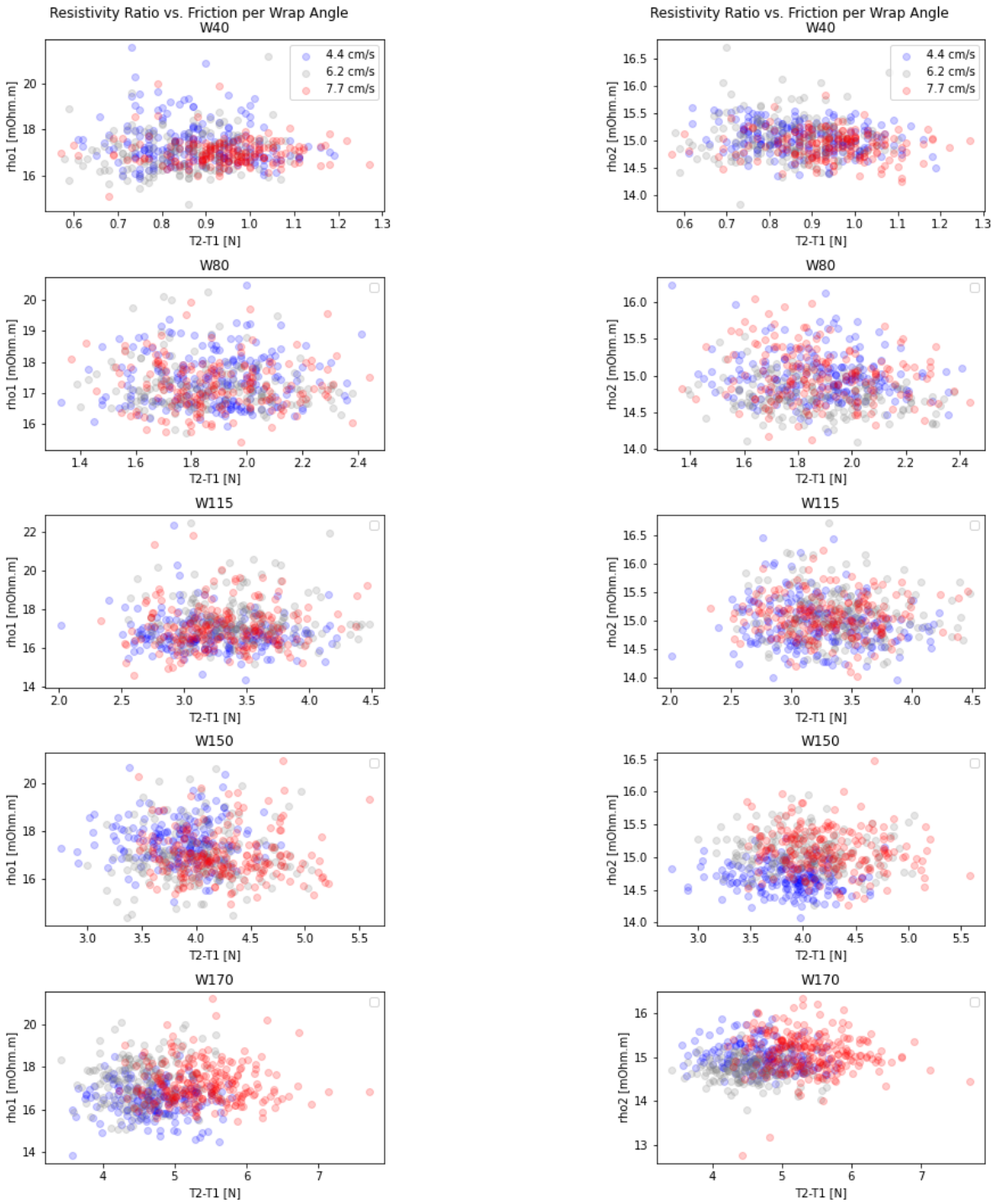


**(a)** Resistivity measurements for sensor 1.

**(b)** Resistivity measurements for sensor 2.

**Figure C.9:** Overview of resistivity measurement results sorted by their related pulling speed, per wrap angle per sensor. Mechanical brake pre-tension at setting 2/5.

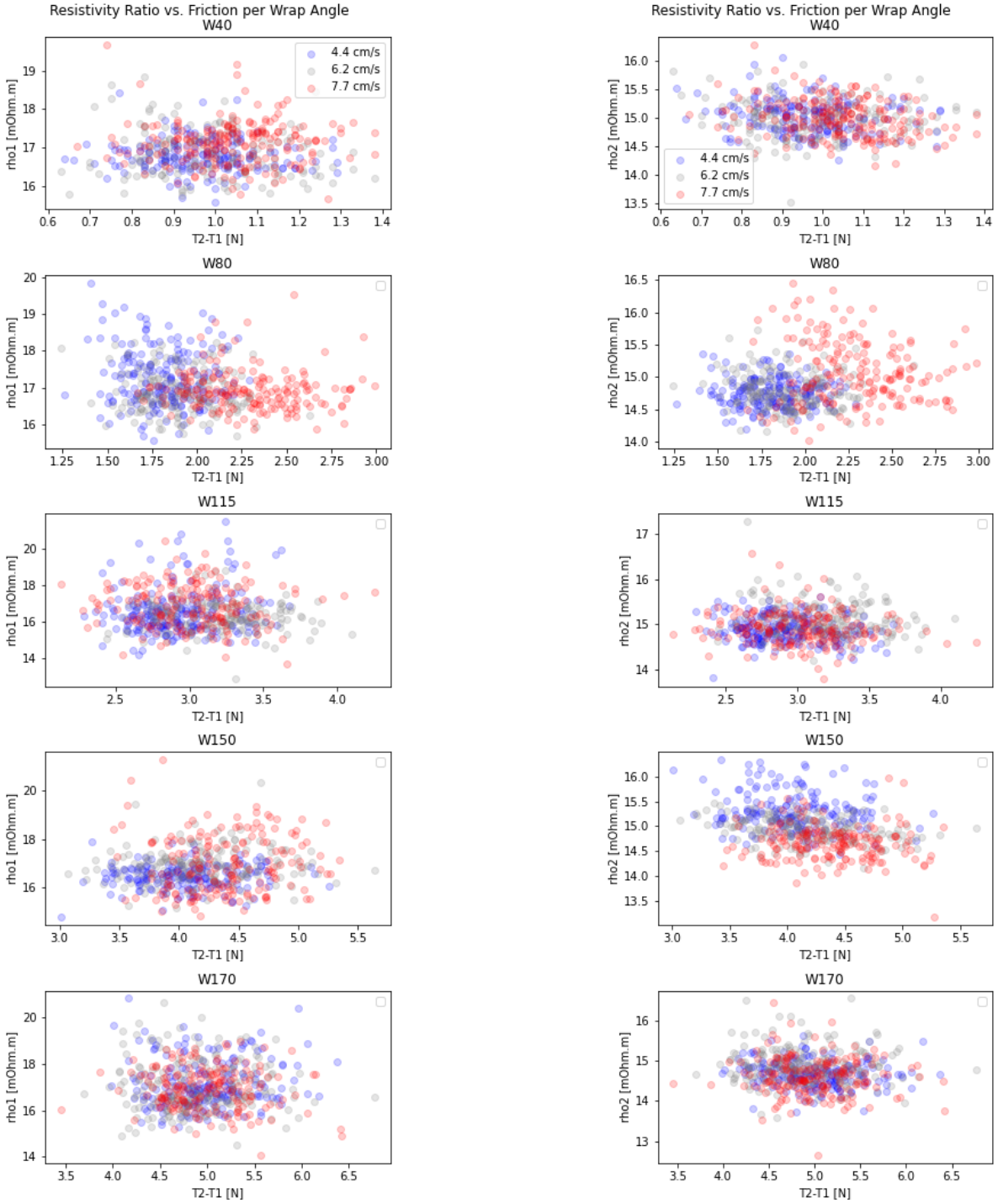


**(a)** Resistivity measurements for sensor 1.

**(b)** Resistivity measurements for sensor 2.

**Figure C.10:** Overview of resistivity measurement results sorted by their related pulling speed, per wrap angle per sensor. Mechanical brake pre-tension at setting 3/5.

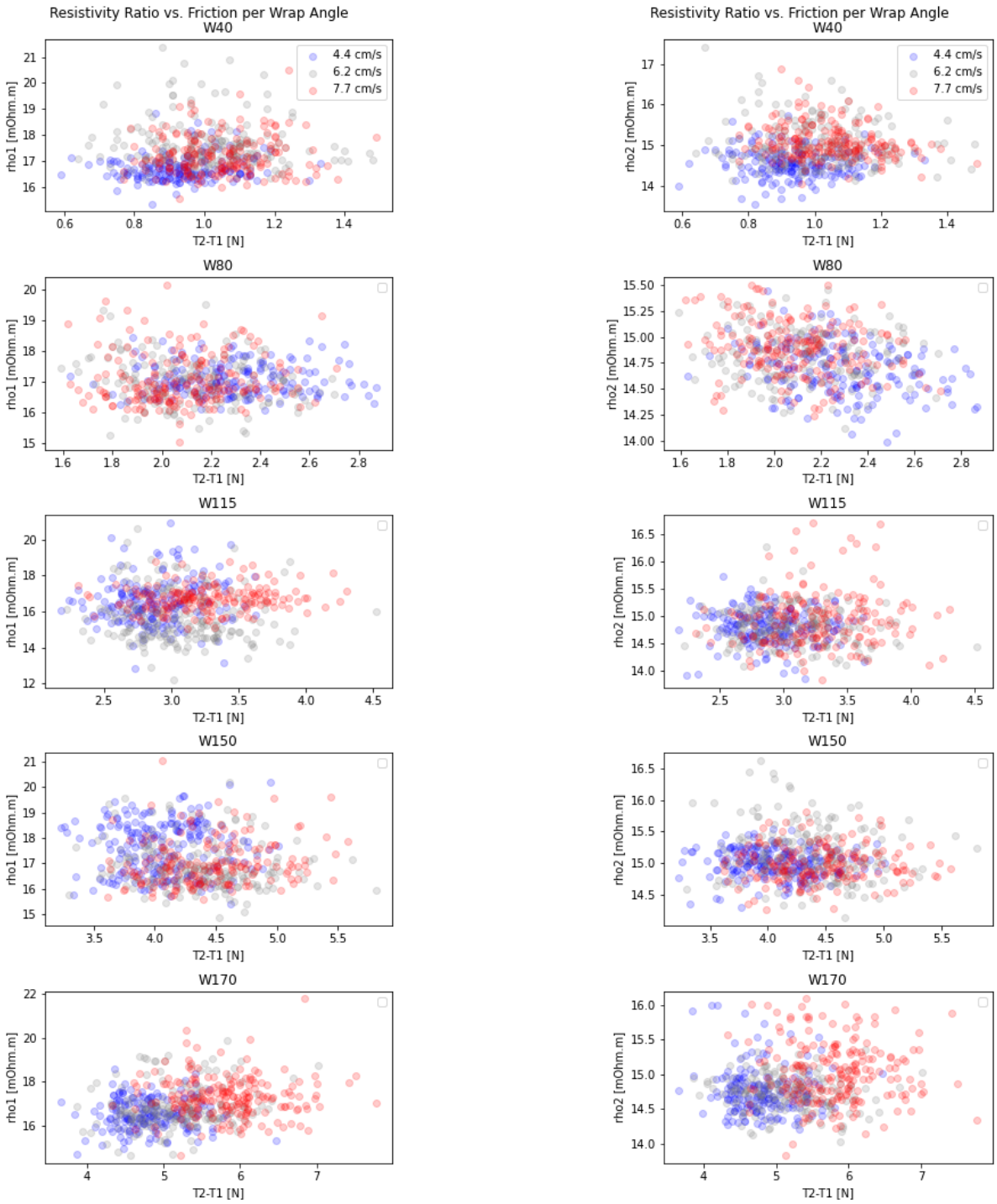


**(a)** Resistivity measurements for sensor 1.

**(b)** Resistivity measurements for sensor 2.

**Figure C.11:** Overview of resistivity measurement results sorted by their related pulling speed, per wrap angle per sensor. Mechanical brake pre-tension at setting 4/5.

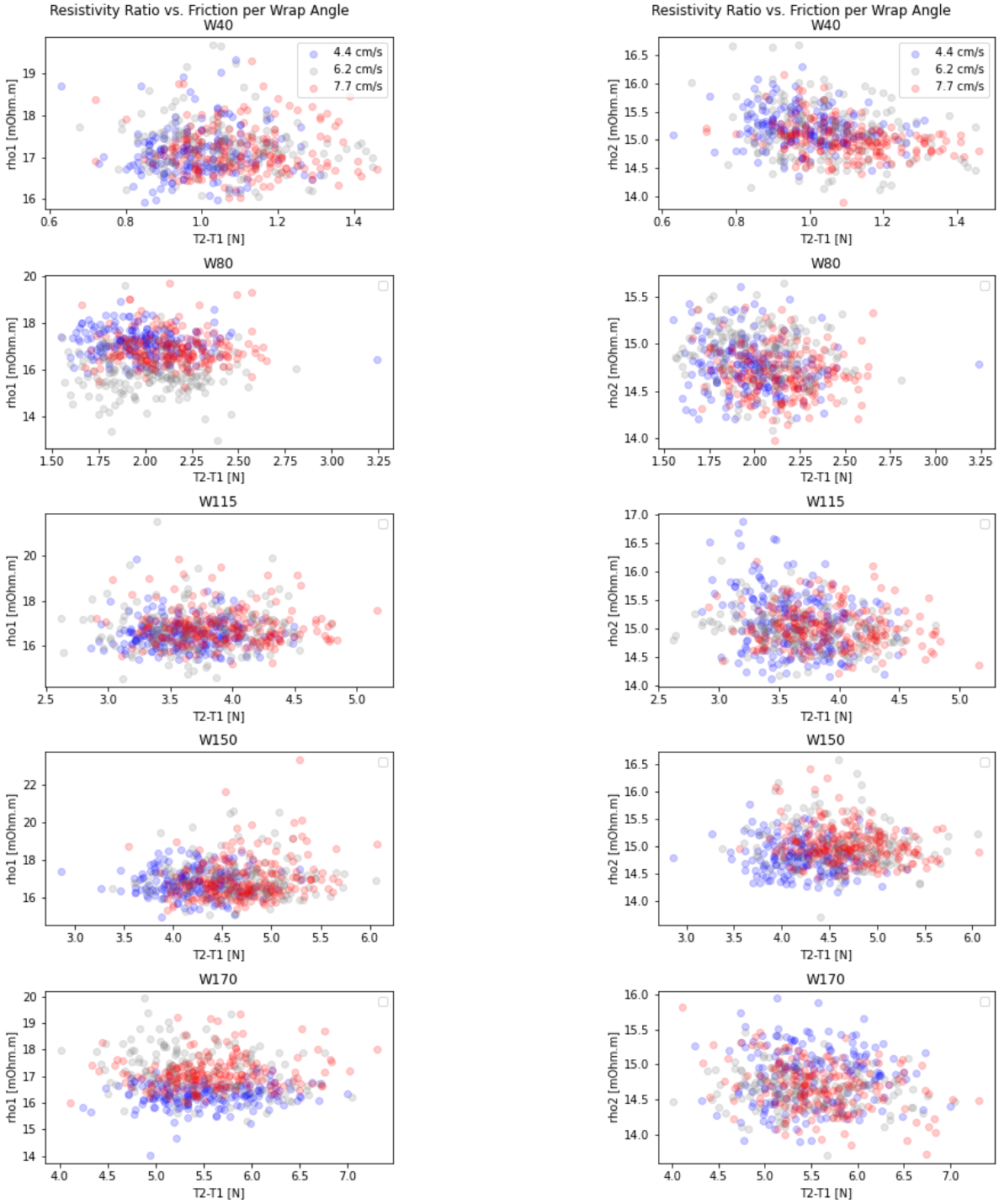


**(a)** Resistivity measurements for sensor 1.

**(b)** Resistivity measurements for sensor 2.

**Figure C.12:** Overview of resistivity measurement results sorted by their related pulling speed, per wrap angle per sensor. Mechanical brake pre-tension at setting 5/5.

# C.3. Orientation Analysis

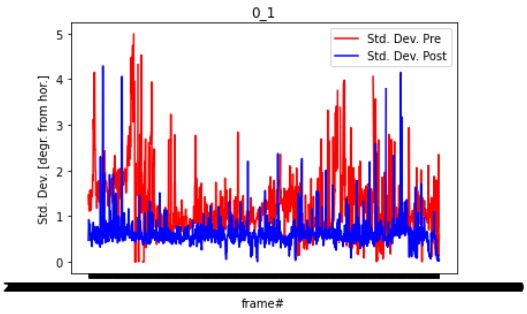


**(a)** Individual responses of cameras 1 and 2.

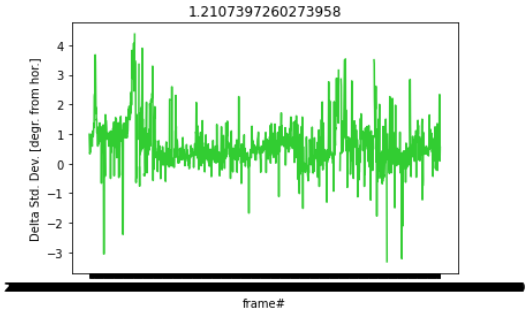


**(b)** Absolute difference between responses 1 and 2.

**Figure C.13:** Standard deviation recordings of camera 1 (pre-) and camera 2 (post-spread), and their absolute difference. From 0degree WA setup.

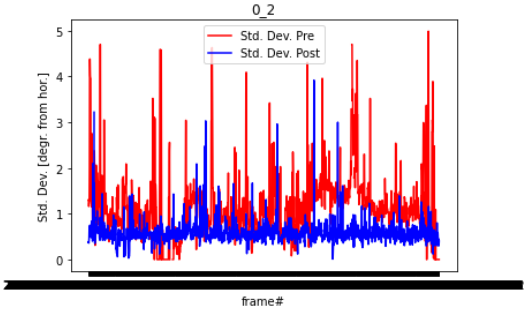


**(a)** Individual responses of cameras 1 and 2.

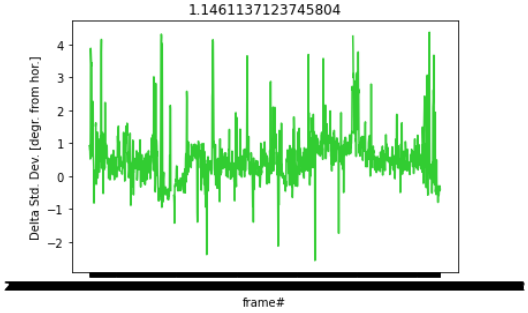


**(b)** Absolute difference between responses 1 and 2.

**Figure C.14:** Standard deviation recordings of camera 1 (pre-) and camera 2 (post-spread), and their absolute difference. From 0degree WA setup.

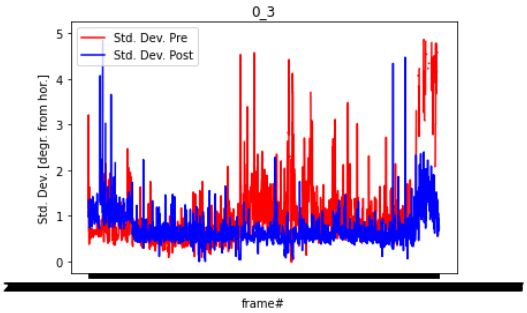


**(a)** Individual responses of cameras 1 and 2.

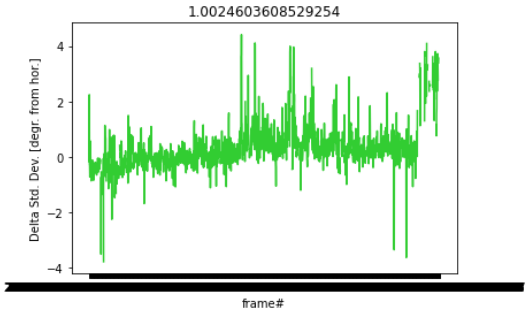


**(b)** Absolute difference between responses 1 and 2.

**Figure C.15:** Standard deviation recordings of camera 1 (pre-) and camera 2 (post-spread), and their absolute difference. From 0degree WA setup.

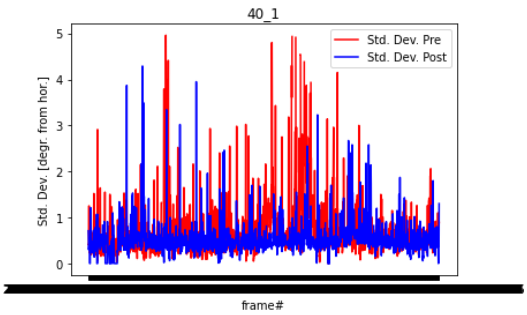


**(a)** Individual responses of cameras 1 and 2.

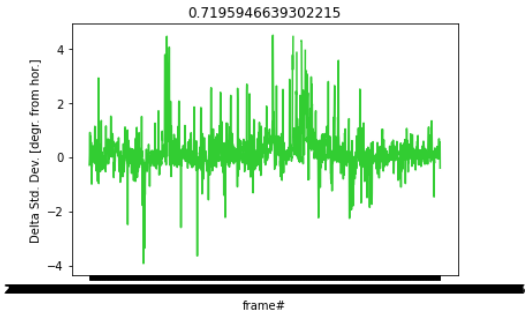


**(b)** Absolute difference between responses 1 and 2.

**Figure C.16:** Standard deviation recordings of camera 1 (pre-) and camera 2 (post-spread), and their absolute difference. From 40degree WA setup.

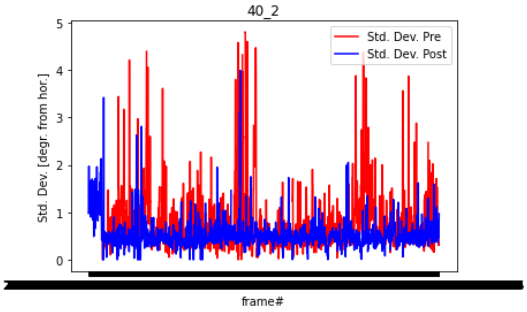


**(a)** Individual responses of cameras 1 and 2.

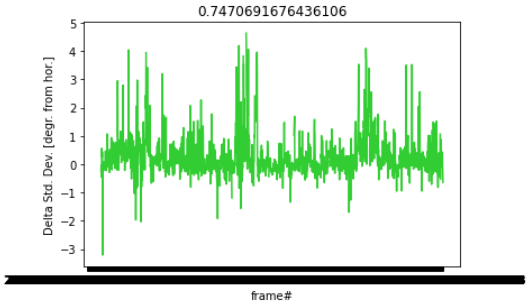


**(b)** Absolute difference between responses 1 and 2.

**Figure C.17:** Standard deviation recordings of camera 1 (pre-) and camera 2 (post-spread), and their absolute difference. From 40degree WA setup.

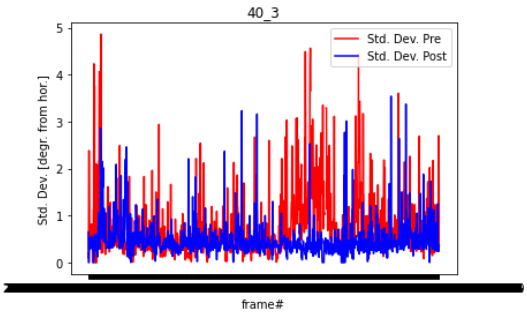


**(a)** Individual responses of cameras 1 and 2.

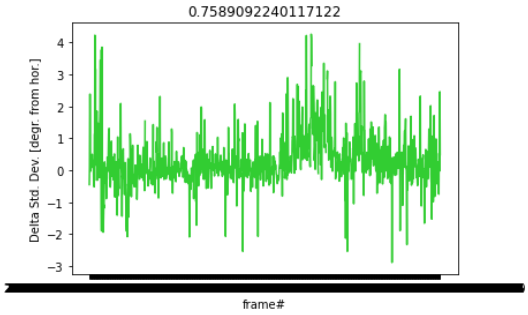


**(b)** Absolute difference between responses 1 and 2.

**Figure C.18:** Standard deviation recordings of camera 1 (pre-) and camera 2 (post-spread), and their absolute difference. From 40degree WA setup.

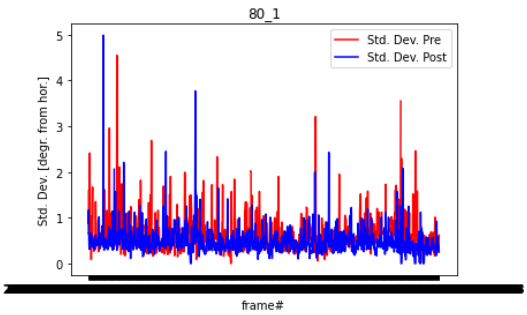


**(a)** Individual responses of cameras 1 and 2.

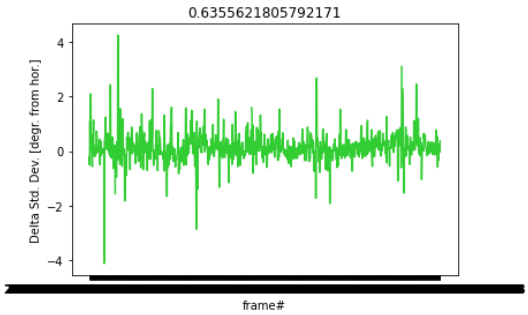


**(b)** Absolute difference between responses 1 and 2.

**Figure C.19:** Standard deviation recordings of camera 1 (pre-) and camera 2 (post-spread), and their absolute difference. From 80degree WA setup.

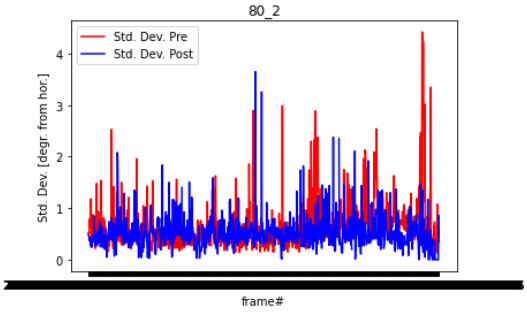


**(a)** Individual responses of cameras 1 and 2.

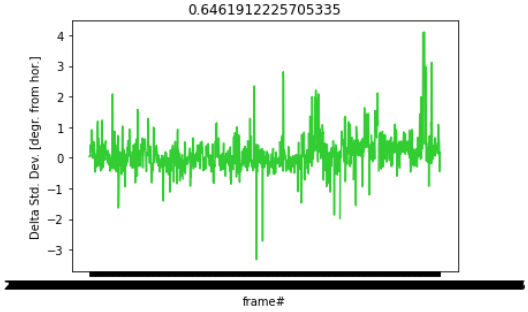


**(b)** Absolute difference between responses 1 and 2.

**Figure C.20:** Standard deviation recordings of camera 1 (pre-) and camera 2 (post-spread), and their absolute difference. From 80degree WA setup.

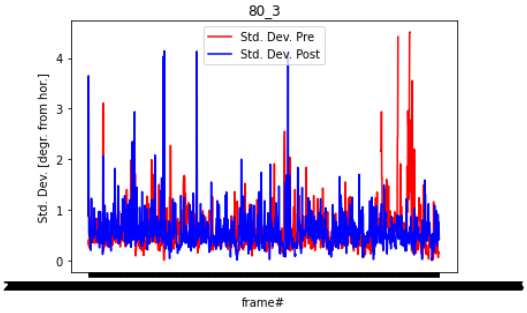


**(a)** Individual responses of cameras 1 and 2.

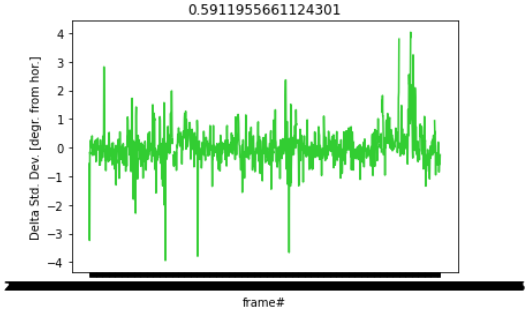


**(b)** Absolute difference between responses 1 and 2.

**Figure C.21:** Standard deviation recordings of camera 1 (pre-) and camera 2 (post-spread), and their absolute difference. From 80degree WA setup.

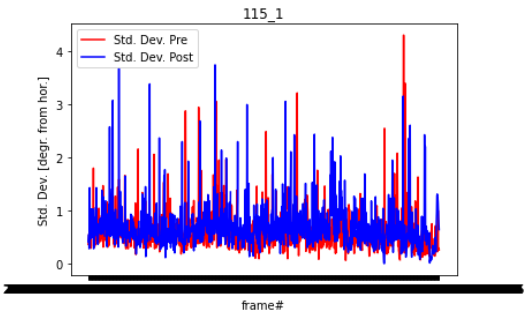


**(a)** Individual responses of cameras 1 and 2.

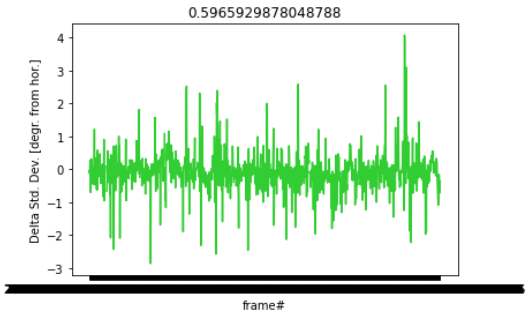


**(b)** Absolute difference between responses 1 and 2.

**Figure C.22:** Standard deviation recordings of camera 1 (pre-) and camera 2 (post-spread), and their absolute difference. From 115degree WA setup.

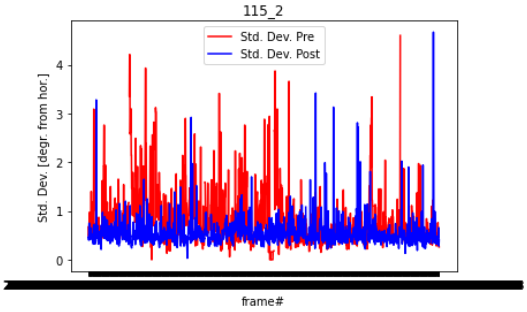


**(a)** Individual responses of cameras 1 and 2.

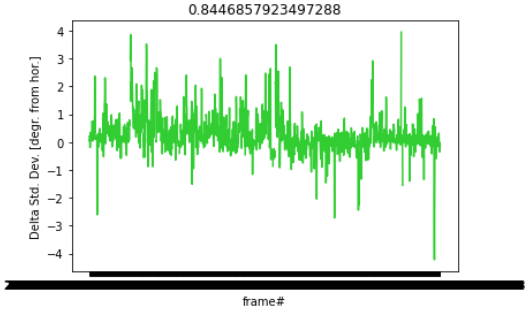


**(b)** Absolute difference between responses 1 and 2.

**Figure C.23:** Standard deviation recordings of camera 1 (pre-) and camera 2 (post-spread), and their absolute difference. From 115degree WA setup.

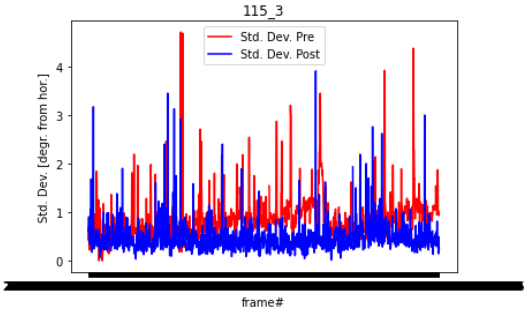


**(a)** Individual responses of cameras 1 and 2.

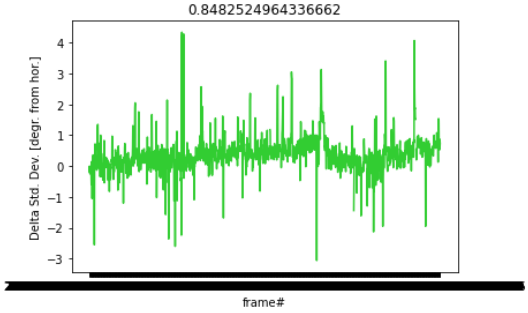


**(b)** Absolute difference between responses 1 and 2.

**Figure C.24:** Standard deviation recordings of camera 1 (pre-) and camera 2 (post-spread), and their absolute difference. From 115degree WA setup.

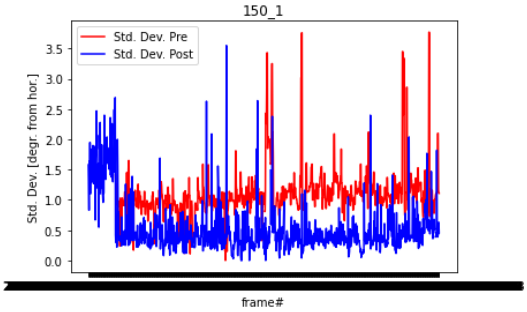


**(a)** Individual responses of cameras 1 and 2.

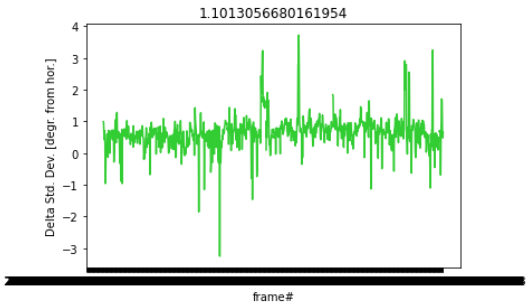


**(b)** Absolute difference between responses 1 and 2.

**Figure C.25:** Standard deviation recordings of camera 1 (pre-) and camera 2 (post-spread), and their absolute difference. From 150degree WA setup.

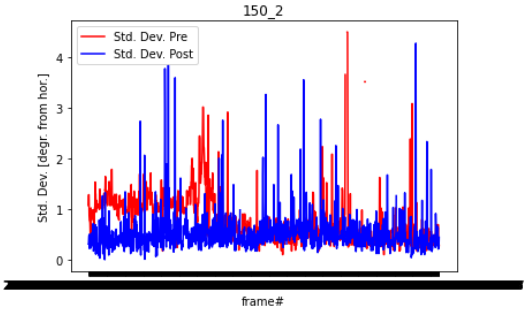


**(a)** Individual responses of cameras 1 and 2.

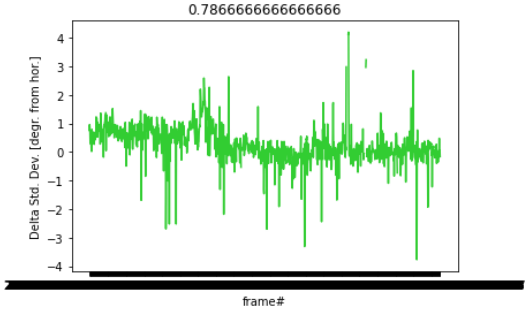


**(b)** Absolute difference between responses 1 and 2.

**Figure C.26:** Standard deviation recordings of camera 1 (pre-) and camera 2 (post-spread), and their absolute difference. From 150degree WA setup.

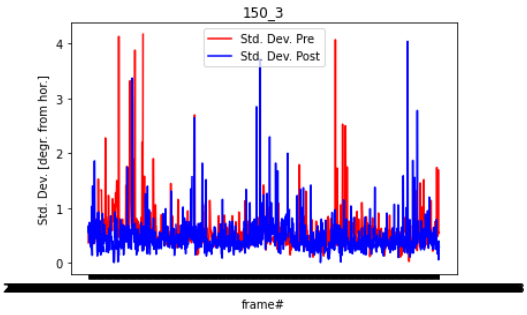


**(a)** Individual responses of cameras 1 and 2.

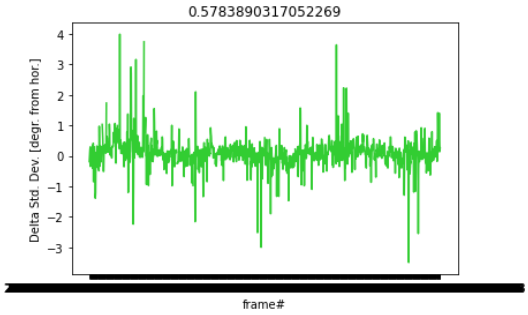


**(b)** Absolute difference between responses 1 and 2.

**Figure C.27:** Standard deviation recordings of camera 1 (pre-) and camera 2 (post-spread), and their absolute difference. From 150degree WA setup.

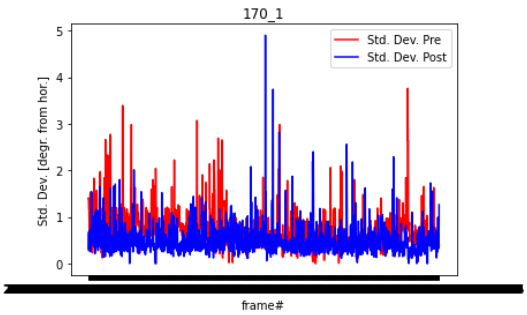


**(a)** Individual responses of cameras 1 and 2.

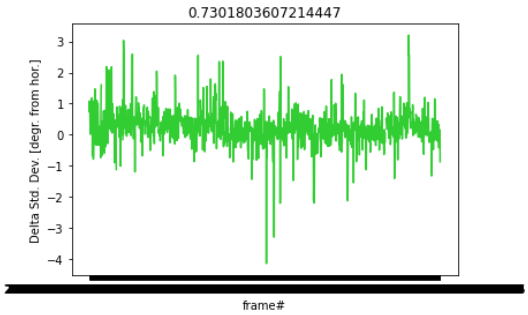


**(b)** Absolute difference between responses 1 and 2.

**Figure C.28:** Standard deviation recordings of camera 1 (pre-) and camera 2 (post-spread), and their absolute difference. From 170degree WA setup.

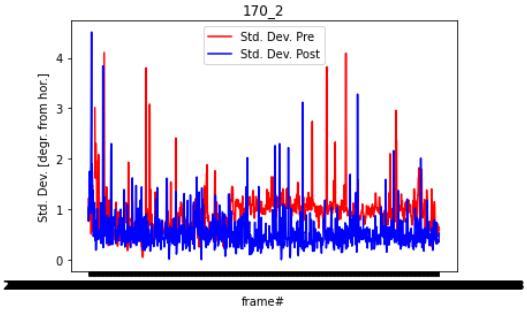


**(a)** Individual responses of cameras 1 and 2.

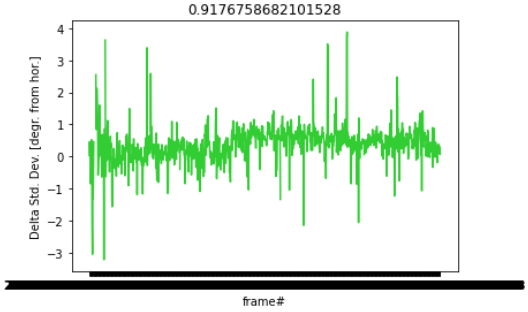


**(b)** Absolute difference between responses 1 and 2.

**Figure C.29:** Standard deviation recordings of camera 1 (pre-) and camera 2 (post-spread), and their absolute difference. From 170degree WA setup.

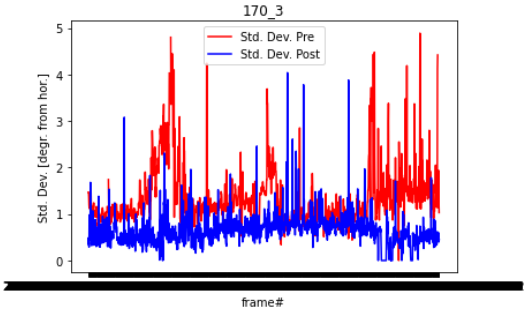


**(a)** Individual responses of cameras 1 and 2.

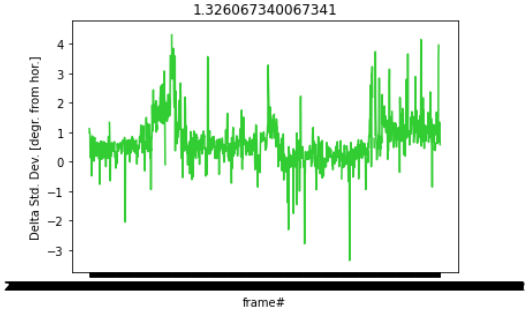


**(b)** Absolute difference between responses 1 and 2.

**Figure C.30:** Standard deviation recordings of camera 1 (pre-) and camera 2 (post-spread), and their absolute difference. From 170degree WA setup.